UNIVERSITY OF BELGRADE
FACULTY OF MEDICINE

Milutin Mićić

INFLUENCE OF THE CHOICE OF PROTOCOLS ON THE ACCURACY OF THREE-DIMENSIONAL MEDICAL MODELS, SURGICAL GUIDES AND BONE REPLACEMENT

Doctoral Dissertation

Belgrade, 2023.

UNIVERSITY OF BELGRADE
FACULTY OF MEDICINE

Milutin Mićić

INFLUENCE OF THE CHOICE OF PROTOCOLS ON THE ACCURACY OF THREE-DIMENSIONAL MEDICAL MODELS, SURGICAL GUIDES AND BONE REPLACEMENT

Doctoral Dissertation

Belgrade, 2023.

УНИВЕРЗИТЕТ У БЕОГРАДУ
МЕДИЦИНСКИ ФАКУЛТЕТ

Милутин Мићић

УТИЦАЈ ИЗБОРА ПРОТОКОЛА НА ТАЧНОСТ ТРОДИМЕНЗИОНАЛНИХ МЕДИЦИНСКИХ МОДЕЛА, ХИРУРШКИХ ВОДИЧА И КОШТАНИХ ЗАМЕНИКА

Докторска дисертација

Београд, 2023.

PhD Advisors:

1) Professor Marija Đurić, MD, PhD, Faculty of Medicine, University of Belgrade, and
2) Senior research associate Đorđe Antonijević, DMD, PhD, Faculty of Dentistry, University of Belgrade

Members of the Evaluation Committee:

- Professor Aleksandar Lešić, MD, PhD, Faculty of Medicine, University of Belgrade
- Associate Professor Petar Milovanović, MD, PhD, Faculty of Medicine, University of Belgrade
- Assistant Professor Drago Jelovac, MD, DMD,PhD, Faculty of Dentistry, University of Belgrade
- Assistant Professor Dejan Ćetković, DMD, PhD, Faculty of Dentistry, University of Belgrade
- Senior research associate Arso Vukićević, PhD, Faculty of Engineering, University of Kragujevac

Date of defense: _____

Ментори:

1) проф. др Марија Ђурић, Медицински факултет, Универзитета у Београду
2) виши научни сарадник Ђорђе Антонијевић, Стоматолошки факултет, Универзитета у Београду

Чланови комисије за оцену и одбрану докторске дисертације:

- проф. др Александар Лешић, Медицински факултет, Универзитета у Београду,
- проф. др Петар Миловановић, Медицински факултет, Универзитета у Београду,
- доц. др Драго Јеловац, Стоматолошки факултет, Универзитета у Београду,
- доц. др Дејан Ћетковић, Стоматолошки факултет, Универзитета у Београду,
- виши научни сарадник Арсо Вукићевић, Факултет инжењерских наука, Универзитета у Крагујевцу

Датум одбране докторске дисертације: _____

Acknowledgements

I express my deepest gratitude to the people who gave me their help and support during my work on this PhD thesis.

To my PhD advisor, Professor Marija Đurić, for continual support and guidance through all scientific work, for patience and understanding of multiple distractions I had in my work, as well as for coordinating a creative team and excellent working atmosphere in Center of Bone Biology.

To my PhD advisor, senior research associate Đorđe Antonijević, for great inspiration, support and guidance during most of the research phase, for introducing me to the research methods, as well as to relations in scientific community.

To my dear colleague, Jelena Jadžić, for introducing me to the art of publishing scientific papers and for her tremendous patience and resilience.

To Assistant Professor Petar Milovanović, for numerous useful methodological and practical advice during my scientific work, as well as continual readiness to help and deal with issues to the details.

To the late Professor Zoran Rakočević, for his great guidance and for sharing all the revealing insights in the field of radiology and life in general.

To Professor Vukoman Jokanović, for sharing his overwhelming knowledge in the field of biomaterial engineering, for synthetizing bone replacement material and for being a most inspirational figure of dedication and innovation.

To Assistant Professor Drago Jelovac and his team, for sharing great knowledge and experience in the fields of maxillofacial surgery and surgical guides, for willingness and courage to be innovative, and for performing surgical procedures in third phase of our research.

To Dr Petar Milenković and Assistant professor Svetlana Antić for their professional support during first phase of the research.

To my dear colleague Dr Teodora Rodić, for her professional guidance and inspiration.

To my dear colleagues from the Center of Bone Biology: Professor Danijela Đonić, dr Ksenija Đukić, dr Ksenija Zelić and Tamara Šarkić, for useful research ideas, valuable advice and inspirational atmosphere.

To my dear colleges from Faculty of Dental Medicine: Professor Sanja Milutinović-Smiljanić, Dr Dijana Trisić, Professor Slavoljub Živković, Professor Jelena Milašin and Professor Vesna Danilović for their great help and support during histological characterization of bone scaffold, without which this research would not be possible.

To my dear colleagues from Institute for Nuclear Sciences Vinča: Dr Zlatko Rakočević, Igor Peterka and Dr Božana Čolović, for their great work in material characterization, without which this research would not be possible.

To my dear colleague Dr Dejana Kosanović from Institute for Virology, Vaccine and Sera “Torlak”, for her professional help in histological analyses.

To dr Miloš Bokorov, University Center for Electronic Microscopy of Novi Sad, for conducting electron microscopy in second phase of our research.

To my dear colleagues from Faculty of Veterinary Medicine: Dr Bogomir Prokić and professor Jugoslav Vasić, for conducting surgery during second phase of our research.

To prof. Bjoern Busse, from Institute for Osteology and Biomechanics, University Medical Center Hamburg-Eppendorf, Germany for enabling the mechanical testing necessary in this research.

The last, but most important, to my family, most of all my mother Radovinka and father Despot, for their unconditional love and support.

Contents

1. Introduction 1
2. Research Aims and Objectives 6
3. Materials and Methods 7
3.1. Material and patients included in the study 7
3.2. Methods 8
3.2.1. Radiological protocols 8
3.2.2. 3D model creation 9
3.2.3. 3D printing procedure 9
3.2.4. Linear and volumetric measurements on physical objects (mandible and 3D printed MM) 10
3.2.5. Linear and volumetric measurements on MDCT and CBCT scans 11
3.2.6. Correction of 3D model axis and volume 12
3.2.7. Bone replacement material synthesis and characterization 13
3.2.8. 3D modeling and printing of the construct 18
3.2.9. *In vivo* implantation of the personalized construct in rabbit's ulna 22
3.2.10. Radiography and micro-CT evaluation 23
3.2.11. Histological and histomorphometric analysis 24
3.2.12. Immunochemical staining for confocal microscopy 24
3.2.13. Clinical implementation of virtual surgical planning, medical models and surgical guides 25
3.2.14. Evaluation of clinical implementation of virtual surgical planning, medical models and surgical guides 31
3.2.15. Statistical analyses 33
4. Results 35
4.1 3D model creation procedure 35
4.2 The measurements on dry mandible and 3D-printed medical models 35
4.3 Intra- and inter-observer tests 43
4.4 Microstructural assessment and wettability determination of 3D-printed bone construct 43
4.6 Radiography of the implanted bone construct and micro-CT analysis of the explanted tissue 46
4.7 Histological and histomorphometric analysis 49
4.8 Immunostaining analysis 52
4.9 Evaluation of clinical implementation of virtual surgical planning, medical models and surgical guides 55
5. Discussion 57
6. Conclusion 66
7. References 67

INFLUENCE OF THE CHOICE OF PROTOCOLS ON THE ACCURACY OF THREE-DIMENSIONAL MEDICAL MODELS, SURGICAL GUIDES AND BONE REPLACEMENT

Abstract:

Background:

Bone defect reconstruction in contemporary medicine increasingly relies on 3D printing. This fast-evolving technology involves areas such as software engineering, 3D modeling, 3D printer, and bio-printer engineering and has a significant impact on biomedicine. There are two main research directions in biomedical 3D printing: 1) 3D reconstruction of radiological images for guided surgery, creation of medical models (MM) and surgical guides (SG), and 2) tissue engineering for a bone replacement material, tissue scaffolds, cells, and implants. To achieve both tasks, appropriate surgery navigation systems and software are needed. However, these software are lacking for complex operations on digital radiological images for various types of surgery, resulting in the slow clinical application of this advanced method. Still, numerous studies point out that computer-aided design and manufacturing are beneficial for surgery, resulting in more predictable surgery outcomes, less operation time, shorter ischemia periods, reduced complication risks, and lower healthcare costs.

Aims:

In this thesis, we aimed to include both main research directions in biomedical 3D printing. Specifically, our first objective was to test whether different radiological scanning protocols, various kernel and window settings, and different equipment influence linear and volumetric measures of both radiological images and 3D printed MM of the human mandible.

The second study phase involved the use of 3D printed bone scaffolds for over-critical size long bone reconstruction on an animal model to achieve regeneration using novel bone mimicking resorptive substitutes based on nanohydroxyapatite and polylactide-co-glycolide, without using stem cells, growth factors, and external fixation.

In the final phase of research, we implemented the methods of MM and SG fabrication, determined in the first phase of the research, in clinical practice, for the reconstructive surgery of the mandible, aiming to improve standard surgical procedures at the Clinic of Maxillofacial Surgery, Faculty of Dentistry, University of Belgrade: by achieving shortened operation and postoperative time as well as improving the functional and aesthetic result of the procedure. In this phase, we also aimed to highlight the benefits of utilizing of “in-house 3D printing” concept.

Material and methods:

In the first phase of research, one dry human mandible from Center of Bone Biology osteological collection, was scanned with six multi-slice computed tomography (MSCT) and two cone beam computed tomography (CBCT) scanning protocols. Eight MM was 3D-printed based

on those scans and compared with human mandible used as a reference. The mandible was chosen because, by its shape, it enables testing of linear and volume contraction of 3D model in all 3 axes. Linear and volumetric measures were compared on medical scans, 3D printed MM, and dry mandible (500 linear and 63 volumetric measures, 563 measures in total). Although there are commercially available surgery navigation systems and software, they are expensive and limited at one specific area of surgery (almost exclusively dental implant guide systems). Moreover, the source code of such software is not available to researchers, making it impossible to experiment by measuring the effects that software architecture modifications imply on 3D models and MM as an end product. That is the reason we focused in this study on open-source software (3DSlicer), as it has high compatibility and surface resolution for medical 3D printing and a wide range of tools for complex operations on digital radiological images.

In the second research phase, a New Zealand white adult rabbit (five months of age, weight 2.5 kg) was used to reconstruct overcritical size bone defect. We firstly done preoperative radiography and optimal MM and SG fabrication procedure obtained in the first phase of the research. Innovative biodegradable materials, nanohydroxyapatite (nHAP) and polylactide –co-glicolyde (PLGA) were used for scaffold fabrication, and a 3D-printed bone scaffold was tested for micro porosity, wettability, and cytocompatibility. Control radiographs were done postoperatively, nine months after the operation and again, after sacrificing of the animal. Explanted material was subject to micro-CT analysis, histological and histomorphometric tests, as well as immunohistochemical staining for confocal microscopy in order to evaluate the osteointegration and restoration of bone continuum.

In the third research phase, seven adult patients of both sexes, with large bone defects of the mandible, from the Clinic for Maxillofacial Surgery on the Faculty of Dentistry, University of Belgrade, were selected for application of the most adequate technical procedure for MM and SG fabrication using 3D printing. The control group, operated without virtual planning, MM, and SG, consisted of five patients.

Results:

Linear measurement comparison on 3D printed MM and dry mandible has shown that the most adequate radiological protocol for precise MM fabrication was CBCT 0.25, while next on the precision scale were CBCT 0.35 and Dental 2.0 H60s, which generated almost the same precision. Volumetric comparison has shown that volumetrically most precise MM were derived from Dental 2.0 H60s and InnerEarUHR1 0.6 U30u radiological protocols. An attempt of volume measure correction through compensation of detected linear deviations improved results of anisotropic volume reconstructions in 4 out of 6 cases, while it has shown negative results on isotropic volume reconstructions.

In the second phase of research, an overcritical size full-diameter long bone (ulna) defect (more than ¼ of total bone length) was reconstructed, for the first time, by a 3D-printed bone scaffold made of innovative biodegradable materials (nHAP and PLGA). All preoperative analyses of bone substitutes, postoperative radiographs, and analyses of explanted material after animal sacrifice have shown desirable osteoconductive, osteoinductive, and osteointegrative characteristics.

During the clinical implementation of virtual planning of lower jaw reconstruction surgery with MM, SG fabrication through an “In-house” 3D printing concept, seven patients were

successfully and on time treated at the Clinic for maxillofacial surgery, Faculty of Dentistry, University of Belgrade. Compared to the control group, an experimental group of patients had significantly decreased postoperative recovery time, better functional and aesthetic operation results, and increased patient satisfaction. A significant positive correlation between the number of guided surgery 3D printed elements (MM, mandibular resection and reconstruction SG, fibular resection SG) and the functional and aesthetic result of the surgery was also determined.

Conclusion:

In total, the results of this dissertation have shown that precise virtual planning, with the use of adequate radiological protocols, as well as corrective and fabrication procedures for 3D models, can successfully produce MM, SG, and even bone replacement scaffolds designed to achieve primary stability without external fixation. Because of the demanding procedure of bone replacement scaffold fabrication and their use in human medicine, this part of the study was limited to proof of concept on an animal model, where for the first time, we used innovative materials for overcritical size (¼ of total length) long bone defect reconstruction, without the use of SC, GF, or external fixation.

The specificity of MM and SG fabrication using different radiological protocols is especially important for mandibular reconstruction surgery, where the donor and recipient regions of patient anatomy are frequently scanned with different radiological protocols or even by different technologies. Therefore, it was essential to simplify the preoperative scanning procedure and enable quick response-guided surgery, which is the core "in-house 3D printing" concept.

Clinical use of virtually planned surgery with the "in-house 3D printing" concept of MM and SG in this dissertation has shown that operation planning time, as well as a time of postoperative patient recovery, was significantly decreased, while functional and aesthetic results of the operation along with patient satisfaction were increased.

Key words: guided surgery, surgical guides, medical models, 3D printing, radiological protocols, bone grafts, overcritical size bone defect
Scientific field: Medicine

Scientific subfield: Skeletal biology

UDK number:_____

УТИЦАЈ ИЗБОРА ПРОТОКОЛА НА ТАЧНОСТ ТРОДИМЕНЗИОНАЛНИХ МЕДИЦИНСКИХ МОДЕЛА, ХИРУРШКИХ ВОДИЧА И КОШТАНИХ ЗАМЕНИКА

Сажетак

Увод:

Реконструкција коштаних дефеката у савременој медицини све више се ослања на 3Д штампу. Ова брзо напредујућа технологија укључује области као што су софтверски инжењеринг, 3Д моделовање, инжењерство 3Д штампача и био-штампача, и има значајан утицај на био медицину. Постоје два главна правца истраживања у биомедицинској 3Д штампи: 1) 3Д реконструкција радиолошких слика за вођену хирургију, медицинске моделе (ММ) и хируршке водиче (ХВ), и 2) ткивно инжењерство за коштане заменике, ткивне скафолде, ћелије и импланте. Да би се извршила оба ова задатка, потребни су одговарајући систем навођења хирургије и софтвер, међутим, за комплексне операције на дигиталним радиолошким сликама за разне типове хирургија, ови софтвери недостају, резултујући у спорој клиничкој апликацији ових напредних метода. Ипак бројне студије истичу да компјутерски потпомогнут дизајн и производња унапређују резултате хирургије, смањују време операције, скраћују време крварења, смањују ризик од компликација и смањују здравствене трошкове.

Циљеви:

Током истраживања, користили смо оба главна правца истраживања у биомедицинској 3Д штампи. Тачније, наш први циљ је био да покажемо да ли различити радиолошки протоколи за скенирање, подешавања кернела и прозора, као и различита опрема, утичу на линеарна и волуметријска мерења радиолошких слика и 3Д штампаних ММ.

Друга фаза истраживања је укључивала употребу 3Д штампаних коштаних надокнада за надокнаду над-критичног дефекта дуге кости на животињском моделу, да би се постигла регенерација употребом иновативног ресорптивног коштаног заменика који својим особинама подражава коштано ткиво, на бази нанохидроксиапатита и полилактид-ко-гликолида, без употребе матичних ћелија, фактора раста и спољашње фиксације.

У финалној фази истраживања, употребили смо методе производње ММ и ХВ, одређене првој фази истраживања, у клиничкој пракси, за реконструктивну хирургију мандибуле, са циљем да унапредимо стандардну хируршку процедуру на Клиници за максилофаццијалну хирургију, Стоматолошког факултета, Универзитета у Београду; постизањем скраћеног оперативног времена и времена опоравка, као и побољшањем естетског и функционалног резултата процедуре. У овој фази, такође смо се трудили да истакнемо предности "*in house 3D printing*" концепта.

Материјал и методе:

У првој фази истраживања, једна људска мандибула из остеолошке збирке Центра за биологију кости и биоантропологију, шест MSCT скенова, два CBCT скена и осам 3Д штампаних медицинских модела били су анализирани. Мандибула је одабрана јер својим обликом омогућава тестирање линеарне и запреминске контракције 3Д модела у све три осе.

Линеарне и волуметријске мере сз узете у поређене на радиолошким скеновима, 3Д штампаним ММ и сувој мандибули (500 линеарних и 63 волуметријске, укупно 563 мере). Иако постоје комерцијално доступни навигациони системи и софтвери, они су скупи и ограничени на једну специфичну област хирургије (готово искључиво на системе за водиче денталних имплантата). Штавише, софтверски код оваквих софтвера није доступан истраживачима, што чини немогућим експерименте са мерењем ефеката модификације архитектуре софтвера на 3Д моделе и ММ као завршне производе. То је разлог из ког смо се концентрисали на софтвер отвореног кода (3DSlicer), као и због високе компатибилности и површинске резолуције за медицинску 3Д штампу и широк спектар алата за комплексне операције на радиолошким сликама.

У другој фази истраживања, одрасли новозеландски бели зец (старости 5 месеци, тежине 2,5 кг) коришћен је за реконструкцију надкритичног коштаног дефекта. Прво је изведена преоперативна радиографија и оптимална ММ и ХВ фабрикациона процедура, утврђена током прве фазе истраживања. Иновативни биодеградибилни материјал, нанохидроксиапатит (nHAP) и полилактид – ко – гликолид (PLGA) су коришћени за фабрикацију скафолда а 3Д штампани коштани скафолд је тестиран на микро порозност, квашљивост и цитокомпатибилност. Контролна радиографија је урађена постоперативно, девет месеци после операције и поново, после жртвовања животиње. Експлатирани материјал је подвргнут микро-ЦТ анализи, хистолошким и хистоморфометријским тестовима, као и имунохистохемијском бојењу за конфокалну микроскопију у циљу процене остеоинтеграције и рестаурације континуума кости.

У трећој фази истраживања, седам одраслих пацијената оба пола, са великим коштаним дефектима мандибуле, са Клинике за максилофацијалну хирургију Стоматолошког факултета, Универзитета у Београду, изабрани су за примену најадекватније техничке процедуре за фабрикацију ММ и ХВ, уз помоћ 3Д штампе. Контролна група, која је оперисана без виртуелног планирања, ММ и ХВ, састојала се од пет пацијената.

Резултати:

Поређење линеарних мера на 3Д штампаним ММ и сувој мандибули је показало да је најадекватнији радиолошки протокол за фабриковање прецизних ММ CBCT 0.25, док су први следећи по прецизности CBCT 0.35 и Dental 2.0 H60s, који су се показали готово исту прецизност. Волуметријско поређење показало је да волуметријски најпрецизније ММ дају радиолошки протоколи Dental 2.0 H60s и InnerEarUHR1 0.6 U30u. Покушај корекције волуменских мера преко корекције линеарних детектованих линеарних девијација, побољшао је резултате анизотропских волуменских реконструкција у 4 од 6 случајева, док је показао негативне резултате код изотропских волуменских реконструкција.

У другој фази истраживања, по први пут је успешно реконструисан над-критични дефект (више од ¼ укупне дужине) пуног дијаметра дуге кости (улне) на животињском моделу, уз помоћ заменика добијеног 3Д штампом од иновативних биоразградивих материјала; нанохидроксиапатита (nHAP) и полилактид-ко-гликолида (PLGA). Све преоперативне анализе коштаног заменика, постоперативне радиографије као и анализе експлантираног материјала после жртвовања животиње, показале су пожељне остеокондуктивне, остеоиндуктивне и остеоинтегративне особине.

Приликом клиничке примене виртуалног планирања реконструктивних хирургија доње вилице са израдом ММ, ХВ и „In house“ 3Д принтинга, успешно је и на време збринуто

седам пацијената на Клиници за максилофацијалну хирургију Стоматолошког Факултета Универзитета у Београду. У односу на контролну групу пацијената, експериментална група пацијената имала је статистички значајно: смањено време постоперативног опоравка, боље функционалне и естетске резултате операције и повећано задовољство пацијента целокупним третманом. Осим тога, утврђена је значајна позитивна корелација између броја употребљених 3Д штампаних елемената вођене хирургије (ММ, мандибуларни ресекциони и реконструктивни ХВ, фибуларни ресекциони ХВ) и фунционалног и естетског резултата.

Закључак:

Укупно, резултати ове студије су показали да прецизно виртуелно планирање, са употребом одговарајућих радиолошких протокола, као и корективним и фабрикационим процедурама за 3Д моделе, може успешно да произведе ММ, ХВ, па чак и скафолде за реконструкцију кости, дизајниране да постигну примарну стабилност без спољашње фиксације. Услед захтевне процедуре за фабрикацију коштаног скафолда и његову употребу у људској медицини, овај део истраживања је био ограничен на „proof of concept“ на животињском моделу, где је по први пут, коришћен иновативни материјал за реконструкцију надкритичног (1/4 дужине кости) дефекта дуге кости, без коришћења матичних ћелија, фактора раста или спољашње фиксације.

Специфичност фабрикације ММ и ХВ коришћењем различитих радиолошких протокола је посебно важна за реконструктивну хирургију мандибуле, где се донорска и реципијентна регија анатомије пацијента често скенирају различитим радиолошким протоколима или чак различитим технологијама. Према томе, било је суштински важно да се поједностави преоперативна дијагностичка процедура и омогући брзи одговор на захтев вођене хирургије, који је суштина “*in house 3D printing*” концепта.

Клиничка употреба виртуелног планирања хирургије са “i*n house 3D printing*” концептом ММ и ХВ, у овој дисертацији, је показала да је време планирања операције, као и време постоперативног опоравка пацијента на овај начин значајно скраћено, док су функционални и естетски резултати заједно са задовољством пацијента читавом процедуром значајно повећани.

Кључне речи: вођена хирургија, хируршки водичи, медицински модели, 3Д штампа, радиолошки протоколи, коштани заменици, над-критични коштани дефект

Научна област: Медицина

Ужа научна област: Биологија скелета

УДК број:_____

1. **Introduction**

Current strategies for reconstructing bone defects are increasingly utilizing three-dimensional (3D) printing technology, which allows the fabrication of physical 3D objects based on virtual models (Berman 2012). This technology is rapidly advancing in areas such as 3D modeling, software engineering, and 3D printer engineering, and is having a significant impact on biomedicine (Ballard et al. 2018). A search of the PubMed database for the term "3D printing" over the past 30 years (1991-2021) shows a steady increase in its appearance frequency, from a few instances per year in the first half of this period to over 4,500 instances in 2021.

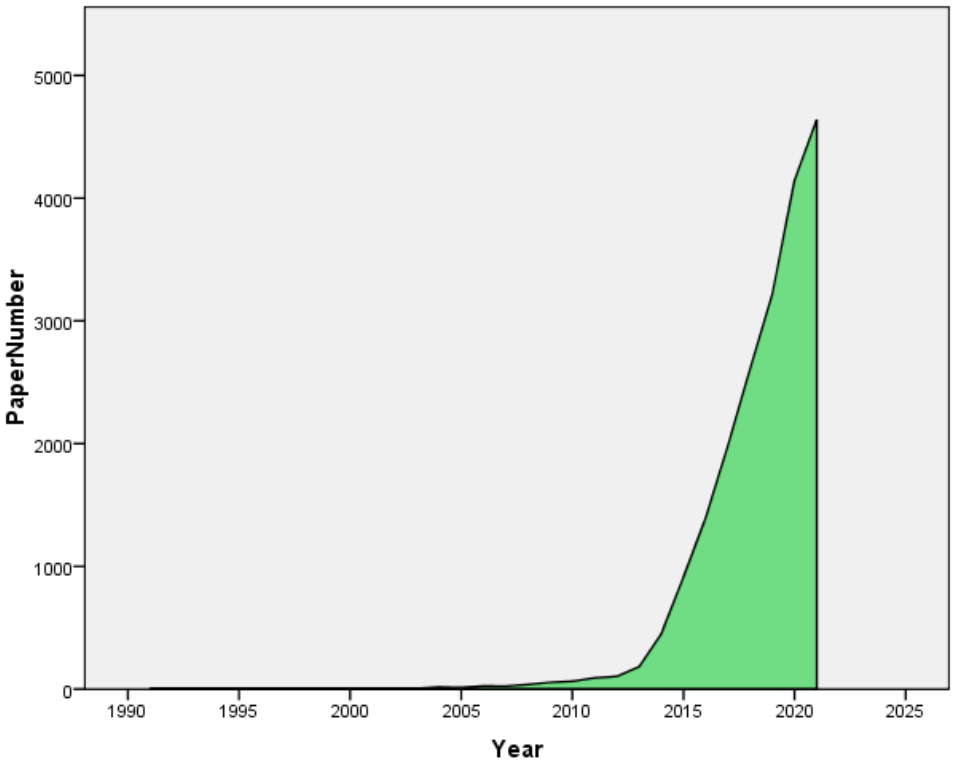

Figure 1: Graph of PubMed database 30-year timeline (1991 – 2021) search for frequency of the term 3D printing in scientific papers.

The most dominant fields of 3D printing implementation in medicine, reported in scientific papers, are knee surgery and maxillofacial surgery, comprising more than 55% of total reported usage (Figure 2, Tack et al. 2016). Research of Tack and associates (Tack et al. 2016) classifies different ways of 3D printing usage, where absolute majority of reported studies use 3D printing in medicine for surgical guides (SG) and medical models (MM) for surgical planning (Figure 2).

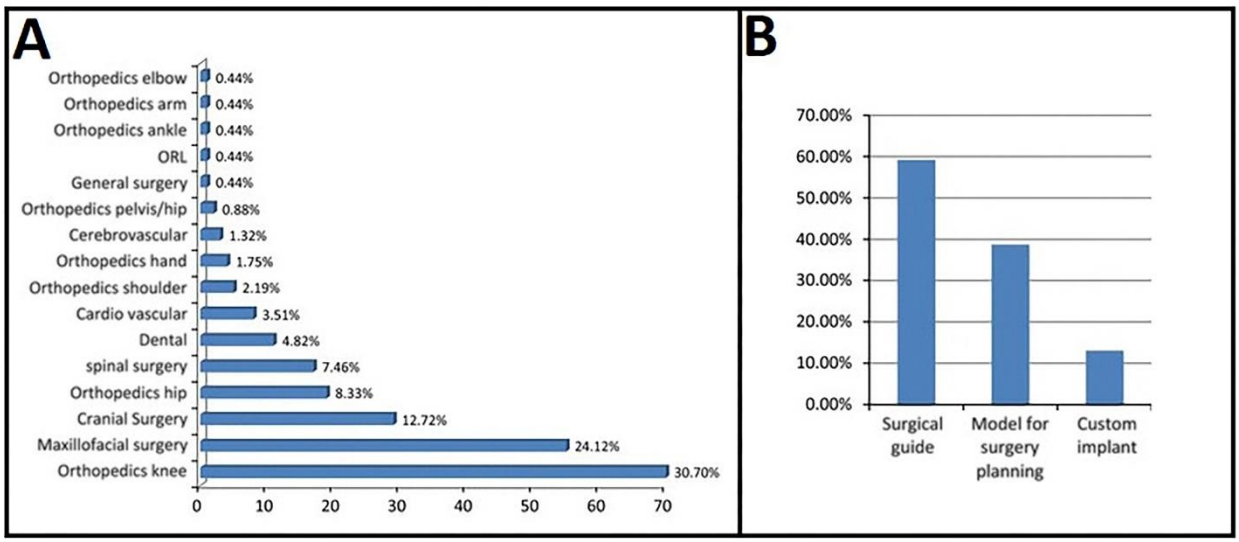

Figure 2: A: Overviev of 3D printig utilization in medicine, B: 3D pringing use by field of surgery (modified from Tack et al. 2016).

Same study showed that SG and MM comprise more than 80% of medical 3D printing and they represent the first of two major directions of research concerning 3D printing in biomedicine. SG and MM are derived from 3D reconstructions of radiological images in the process of virtual surgery planning in the form of 3D models, which then are 3D printed as physical objects that can be used during guided surgery procedures. The second research direction involving 3D printing is tissue engineering and, in the bone surgery field it includes production of bone replacement materials, acellular and cellular tissue scaffolds, or implants to be used during surgical procedure (Sohn and Oh 2019). Both the surgical navigation and the bone scaffold fabrication research directions are complementary in the process of surgical reconstruction of bone defects.

Numerous scientific publications have shown that computer-aided design and manufacturing, particularly in the form of MM and SG, can improve surgical outcomes, reduce operation time, shorten ischemia periods, lower risks, and decrease healthcare costs (Yuan et al. 2016; Serrano et al. 2019; Seruya et al. 2013; Hong et al. 2021; Eltes et al. 2020; Tel et al. 2018). The term "medical models" (Hong et al. 2021) is often used interchangeably with "3D-printed bone" (Eltes et al. 2020) and "human anatomy models" (Vani and Prasad 2017). Moreover, the vast majority of surgeons who have undergone training on the use of computer-aided design and manufacturing are willing to incorporate these methods into their daily practice (Ganry et al. 2018). There are also reports that suggest that virtual surgery planning takes too much time and has questionable cost to benefit ratio, but researchers suggest that these results came from lack of standardized procedures and cooperation between virtual planning and modeling experts and operation surgeon (Martelli et al. 2016).

New technologies in medicine such as 3D-printed MM and SG have also brought new dilemmas and unresolved questions (Tel et al. 2018; Mitsouras et al. 2015; Della Bona et al. 2021). Some of them are related to quality of medical images. Namely, SG, 3D-printed human anatomy MM for surgery planning and aid, along with educational models are all derived from Computed Tomography (CT), Cone Beam Computed Tomography (CBCT) and Nuclear Magnetic Resonance Imaging (NMRI), which produce Digital Imaging and Communication in Medicine (DICOM) files that are essential for 3D printing in medicine. However, radiologists are yet far away from adopting medical 3D printing as a crucial tool for producing precise 3D-printed MM and SG for all types of innovative surgeries (Della Bona et al. 2021). In clinical practice, radiologist often rely on their experience during CT reading, which may not be

scientifically verified (Auriemma, Voorhout and Barthez 2007). This can result in differences in image quality and influence on linear and volume measures, especially in lung and bone analyses (Mah, Reeves and McDavid 2010). Acquisition settings can also affect these variables (Troy and Edwards 2018). Additionally, bone kernel settings sharpen the radiological image and may lead to voxel order of magnitude alteration in bone dimensions' measurement on a radiological image (Dalrymple et al. 2007). All these variables in interpretation of radiological image and its segmentation for 3D model creation, can lead to discrepancies in dimensions used for MM and SG fabrication. The discrepancies of even one mm order of magnitude can result in misfit when bone surgical guides or scaffolds are placed, ultimately leading to a poor or unsuccessful surgical outcome. For example, while CBCT is a preferable method for scanning the mandibular region, creating a set of SG for mandibular reconstruction often involves CT of the donor region, which should enable the same precision as CBCT for autograft SG and MM, reported usually as "accuracy of the harvested transplant" and "final aesthetic result" throughout the different studies (Serrano et al. 2019).

Altogether, while there is a significant amount of evidence on the preciseness of 3D-printed models using different 3D-printing technologies, there is a lack of investigation into the influence of various scanning protocols and different radiological scanner technologies on the geometrical accuracy of 3D-printed models compared to the physical object of medical scanning (Ballard et al. 2018; Eltes et al. 2020; Whyms et al. 2013). Furthermore, there is a need for further exploration of comparing 3D CT/CBCT renderings and 3D models for volumetric measurements (Troy and Edwards 2018).

In order to initialize the process of virtual surgery planning the software that can correctly transform radiological images to surface 3D models to enable MM and SG modeling and 3D printing is also needed. Commercially available surgical navigation systems and software are limited to specific areas of surgery, with dental implant guide systems being the most common. Optical oral scanners in combination with CBCT have made dental implant guide fabrication more automated and easier compared to other fields of surgery. However, there is no commercially available software that can automatically design a reconstruction of a large bone defect or any irregular shape defect caused by disease or trauma. This highlights the need to focus on principles that can be applied in most surgery areas and open-source software, such as 3DSlicer (Brigham and Women's Hospital, Inc., Boston, MA), which has shown the highest compatibility and surface resolution for medical 3D printing and provides a wide range of tools for complex operations on digital radiological images (Bücking et al. 2017) to improve surgical outcomes and ensure success (Hou et al. 2020).

The second stream of bone tissue engineering research, which deals with bone tissue scaffolds fabrication, aims to integrate all the principles of SG and MM fabrication, because scaffold fabrication requires the same precision. However, this is only possible if researchers can mimic the micro-architectural and biological characteristics of natural bone tissue. One promising solution is medical 3D printing or 3D bio-printing of bone substitutes, which can meet the strict demands for 3D micro-architecture and material properties (Xu et al. 2012).

Recent research suggests that an ideal bone substitute material should provide primary stability and temporary mechanical integrity at the defect site until the bone tissue is regenerated, replacing the scaffold (Yang et al. 2018). It should also possess desirable compressive strength and toughness, bone-mimicking porosity (>50% porosity and >100 μm average pore size), and nanotopography surface features, including roughness and wettability (Cao et al. 2015). Thus, the final goal is to achieve adequate osteoconductivity (the capability of the material to provide the transport of nutritive agents through its pore system), osteoinductivity (the capability of the material to induce new bone formation in contact with

the substitute) and osteointegrativity (the capability of the material to incorporate into the surrounding bone structures) (Liu et al. 2017).

In addition, the micro- and nano-meter surface topography of the bone construct is crucial for directing cellular adhesion, cell spreading, and proliferation. Bone substitute manufacturing should be inspired by the natural processes of developmental biology and promote tissue remodeling, rather than merely supporting definitive form and function (Cao et al. 2015; Liu et al. 2017). Finally, customized 3D printing for bone construct manufacture is highly recommended, as critical-size defects usually have a complex shape in different clinical conditions (Lee et al. 2018).

Despite the significant progress made in creating bone substitutes that meet the requirements for long-term bone repair (Hutchens et al. 2016; Sohn and Oh 2019), researchers still face several challenges. Calcium sulfate products have very high solubility, hydroxyapatites (HAPs) have a low resorption rate, while coral-based substitutes are too brittle (Yang et al. 2018). However, a novel bone-mimicking resorptive bone substitute based on nanohydroxyapatite (nHAP) and poly(lactide-co-glycolide) (PLGA) has recently been introduced and shows numerous desirable characteristics (Karadzic et al. 2015). It demonstrated adequate surface characteristics for cell attachment, satisfactory solubility and desirable mechanical properties. Using this innovative material, complete bone repair in rabbit's calvaria was achieved in 12 weeks (Jokanovic et al. 2016, Jokanovic et al. 2017).

Traditional methods of bone scaffold fabrication, such as solvent casting and particulate leaching, require around eight days to prepare the material and additional time for machining and post-processing to personalize the scaffold (Xu et al. 2012). Despite progress in bone substitute fabrication, many issues remain unresolved, such as achieving an ideal balance between the replacement material's resorption and bone in-growth (Zhang et al. 2017).

To authors best knowledge, only two studies have reported successful reconstruction of bone osteotomy, where the complete long bone diameter was removed, by seeding stem cells on the construct's surface before implantation along with bone morphogenetic protein (BMP2) acting as an osteoinductor (Zhang et al. 2017; Zhang et al. 2009). The authors speculated that current developments are nearing the point where large bone defects can be restored without such stimulative biofactors.

The next issue concerns the possibilities for clinical utilization of virtual surgery planning with MM and SG fabrication protocol, optimized in the first step of the research. The current situation in Serbian clinical practice regarding SG, MM, and bone tissue engineering is such that their usage is insignificant compared to the number of medical cases that would benefit from their utilization. The situation is not very different in other countries, given that the number of scientific papers that deal with 3D printing in medicine has reached over 4.500 per year (Figure 1), and only a a small number of clinics use 3D printing techniques for human medical ends. Out of 757 scientific papers dealing with 3D printing from January 2011 to January 2015, according to the PubMed database, only 189 of those used it for human medical ends, according to Tack and associates (Tack et al. 2016 Even in the European Union countries with higher standards, involvement in these technologies is still unsatisfying. Della Bona et al. eport that 3D printing of restorative materials, even in dentistry, is in its early translation phase since the review found that only five studies actually applied 3D printed restorative structures to patients (searching MEDLINE/PubMed, Scopus, and Web of Science databases, with no time limitation) (Della Bona et al. 2021). Other reviews point out that studies often do not report complete guided surgery, MM and SG preparation time, but only the time needed to print the model. However, the studies that state the actual virtual planning, design, and 3D printing time – report up to 2 weeks needed to complete the procedure (Martelli et al. 2016).

This is usually because the production facilities, with necessary 3D printers and other equipment are, in the vast majority of cases, very distant from the clinic that the patient is in and where medical scanning is being done. Moreover, preoperative virtual planning requires considerable involvement of the surgeon, who is often not a part of the virtual planning and 3D printing team. The issue is further complicated because mandibular and maxillofacial injuries in general, as well as oncological patients with morbidity of this region, require urgent surgical procedures in most cases. It is clear that 14 days of planning and preparing the surgical procedure in these cases may mean inadequate healing and serious consequences.

The first issue in further research should address the possible influence of different radiological protocols and different radiological equipment on virtual surgical planning with MM and SG fabrication to ensure that chosen protocol is the most suitable for virtual surgical planning. Having in mind the stated problems with bone scaffold fabrication and long bone reconstruction, the shortening scaffold fabrication procedure and long bone defect reconstruction without complex and time-consuming procedures, like stem cells seeding (SC), growth factors (GF), and external fixation (Zhang et al. 2009; Xu et al. 2012; Fassbender et al. 2014) is desirable to achieve.

To address questions of clinical utilization of virtual surgical planning, MM and SG, we propose “in house 3D printing” concept, meaning that a small 3D printing facility should be built in the clinics where patients should be operated in. In this way the delay in the procedure, from acquiring DICOM files to fabrication of MM and SG might be avoided.

2. Research Aims and Objectives

To address the influence of different radiological protocols and various scanning technologies on dimensional accuracy of MM and SG, we aimed to determine the best radiological protocol, as well as most adequate technical procedure for 3D printing of MM and SG. Specific objectives to test the first hypothesis were:

1. To scan the dry mandible by using six different MSCT and two CBCT radiological protocols.
2. To transform DICOM data obtained by these protocols intoprintable 3D object and 3D-print them, using the same programs and the same software settings.
3. To measure and compare linear and volumetric measures taken on dry mandible (used as a reference) with the same measures on MSCT /CBCT scans and 3D-printed MM derived based on these scans.

Aim of the second part of this research was to produce personalized hydroxyapatite-based bone substitute for overcritical size (over ¼ of long bone length) bone defect on the rabbit model and reconstruction of the defect without SC seeding on the bone substitute, addition of bone morphogenetic proteins or external fixation.
Specific objectives of the second hypothesis were:

1. To design and fabricate a custom 3D printer for bone substitute prototyping.
2. To characterize the bone substitute after its production via 3D printing, for 3D micro-porosity testing, wettability and cytocompatibility in order to check its suitability for bone replacement.
3. To implant the construct and reconstruct segmental defect of rabbit's ulna following the most suitable methods based on the first part of the research.
4. To perform radiography and micro-CT evaluation, as well as histological and immunohistochemical analysis of the reconstructed area *ex vivo*, in order to assess level of graft osteointegration and bone regeneration.

Aim of the final part of the research was to determine the effects of clinical implementation of "in house" virtual surgical planning, MM and SG. Specific objectives to this aim was to measure and compare the results of experimental group (threated with the use of this technology) to the control group (threated without use of this technology) for these parameters:

1. Time to surgery (time required for the whole procedure of surgical planning, MM and SG fabrication)
2. Surgery time or surgery duration
3. Time of hospitalization
4. Surgical complications
5. Functional result
6. Final aesthetic result
7. Patient satisfaction
8. Clinical outcome

3. Materials and Methods

3.1. Material and patients included in the study

In the first part of the research (testing different scanning protocols), one dry human mandible from the osteological collection of the Center of Bone Biology was assessed with six MSCT scanning protocols and two CBCT imaging protocols. Then eight MM was 3D printed and subsequently compared with human mandible (used as a reference) to compare the accuracy of the MM fabrication using different imaging technologies and scanning protocols. The mandible was chosen due to its shape, which allows for testing of volume and metric contraction of 3D models in all three axes.

For the second part of the research (using the chosen protocol and 3D printing procedure for reconstruction of large bone defects), one New Zealand white adult rabbit (five months old, weighing 2.5 kg) was used in accordance with EU guidelines for animal model study procedures (86/609/EEC), the Guide for the care and use of laboratory animals, National good laboratory practice guidelines and principles of laboratory animal care. The rabbit was obtained from the Faculty of Veterinary Medicine, University of Belgrade. To reconstruct an overcritical size bone defect, nHAP and PLGA materials were used during 3D printing of bone scaffold. This part of the research was specifically approved by the Ethics Committee of the Faculty of Veterinary Medicine, University of Belgrade (approval number: 323-07-06340/2019-05/1, issued on 08.03.2016).

In the third part of our research, the total of 12 adult patients of both sexes (4 men and 8 women) with large bone defects of the mandible were selected from the Clinic for Maxillofacial Surgery,Faculty of Dentistry, University of Belgrade, to test clinical application of the most appropriate technical procedures for MM and SG fabrication. Of all included patients, seven individuals were included in experimental group (2 men and 5 women) treated with use of virtual planning and 3D printing technology, while five individuals (2 men and 3 women) were treated without the use of 3D printing technology (control group). This part of the research was approved by the Ethics Committee of the Faculty of Dentistry, University of Belgrade (approval number 36/30, dated 10th December 2021), and informed consent was obtained from the patients involved.

The inclusion criteria for study participants were large bone defects on the mandible and the patient's consent to the procedure. We classified the type of mandibular defect required for surgical treatment according to Ragbir et al. 2016, as follows:

- Class I (70 mm)/Ic (84 mm): Subcondylar region to the ipsilateral canine, and class Ic includes the condyle.
- Class II (85 mm)/IIc (126 mm): Hemimandibulectomy from the subcondylar region, including the ipsilateral canine, and class IIc includes the condyle.
- Class III (100 mm): Includes both canines but neither angle.
- Class IV (152 mm)/IVc (168 mm): This is an extensive mandibulectomy, including at least one angle and both canines.

Ethics Committee of the Faculty of Medicine, University of Belgrade confirmed that procedures conducted during this research are in accordance with Helsinki declaration and comparable ethical standards (approval number 1322/XII-5, dated 30th December 2021).

3.2. Methods

3.2.1. Radiological protocols

We used eight radiological protocols to determine the most suitable one for deriving 3D printed MM of bone tissue and to determine the influence of different radiological protocols on linear and volumetric mandibular measures. Scanora 3D CBCT scanner (Soredex, Tuusula, Finland) and SOMATOM Sensation 16 MSCT system (Siemens, Germany) were used to scan one human mandible. The human mandible was emersed in the water in order to mimic surrounding soft tissue (Mah, Reeves and McDavid 2010).

Table 1: Scanning protocols used in our study

Scanning methodology	Scanning protocol
MSCT	Dental 0.75 H60s
	Dental 0.75 H30s
	Dental 2.0 H60s
	Dental 2.0 H30s
	InnerEarUHR 0.6 U90u
	InnerEarUHR 0.6 U30u
CBCT	CBCT 0.25
	CBCT 0.35

On Table 1, used protocols for mandibular scanning are listed. In short, we used the following MSCT protocols:

1) Dental 0.75 protocols: the scanning protocol officially recommended by Siemens for jaw analyses on used scanning equipment; To determine the influence of kernel and window settings, protocol involved kernel and window reconstructions for bone and soft tissues (Dental 0.75 H60s and Dental 0.75 H30s protocols).

2) Dental 2.0 protocols: the wide collimation mode of the same scan protocol as the previous one, considering radiation dose reduction; To determine the influence of kernel and window settings, protocol involved kernel and window reconstructions for bone and soft tissues (Dental 2.0 H60s and Dental 2.0 H30s protocols).

3) InnerEarUHR 0.6 protocols: another scanning protocols designed for accurate assessment of delicate bone structures; To determine the influence of kernel and window settings, protocol involved kernel and window reconstructions for bone and soft tissues (InnerEarUHR 0.6 U90u and InnerEarUHR 0.6 U30u protocols).

We used clinically relevant scanning protocols that achieve only anisotropic MSCT voxels and compare them with two CBCT scan protocols (CBCT 0.25 and CBCT 0.35) that are known to produce isotropic voxels, in order to compare the anisotropic and isotropic voxel influence on dimensional accuracy.

MSCT examinations were carried out with the same FOV (150±1mm) without repositioning of the mandible. The body of the mandible was positioned on a flat surface during all scanning procedures, aligned to the axial plane of the scan. Anatomical landmarks on the condyles of the mandible were aligned to the coronal plane, while anatomical landmarks on the mandibular symphysis were aligned with the sagittal plane of the scan. MSCT and CBCT data were exported and saved in DICOM mode from the acquisition station to be used in 3D printing of mandibular MM.

3.2.2. 3D model creation

The acquired DICOM files were imported into 3DSlicer software version 4.10 (Brigham and Women's Hospital, Inc., Boston, MA, USA). The Volume Reconstruction tool and Editor Mode were used to segment the mandibular bone tissue from the rest of the DICOM volume, starting from a grayscale value of 400, based on grayscale bone values defined for Scanora3D scanner by Mah P. and associates (Mah, Reeves and McDavid 2010) and experience of the researcher with the attention to most segmentation-sensitive areas of mandible, like mandibular condyle. The segmentation was performed using thresholding and segmentation tools, which were used to exclude any non-connected voxels, resulting from artifacts or other surrounding structures. The segmentation was performed by two investigators, and the Dice Similarity Index (DSI) was calculated with the 3DSlicer Computation tool (Eltes et al. 2020; Bharatha et al. 2001). The DSI quantifies the relative volume overlap between two segmentation procedures, using the following formula: $DSI = 2V(I1 \cap I2) / V(I1) + V(I2)$, where V is the volume of the voxels inside the binary mask, and I1 and I2 are the binary masks from two segmentation processes performed by two investigators. The acquired segmentations were then converted to 3D surface models in the Editor Mode of the 3DSlicer and exported as STL files.

Meshmixer 2020 (Autodesk Inc.) and Autodesk 3Ds Max 2010 (Autodesk Media and Entertainment, San Francisco, California) software were used to remove inner shells, duplicates faces and edges, and create solid surface 3D models suitable for G-code generation. This software was also used to create 3D models of SG needed for seven patients treated at Clinic for Maxillofacial Surgery, Faculty of Dentistry, University of Belgrade. During all DICOM to 3D conversion procedures, there was no repositioning of the DICOM/3D model axis.

3.2.3. 3D printing procedure

The 3D printing procedure was performed using the Creality Ender-3 3D printer (Shenzhen Creality 3D Technology Co, Ltd, Shenzhen, China) and fused deposition modeling technique (FDM). The printer was calibrated and tested by printing ten 20x20x20 mm test cubes and ten 40x40x40 mm cubes using the same settings for G-code preparation and Creality PLA+ 1.75mm diameter 3D filament. All cube 3D models were aligned perpendicular to the X, Y, and Z axes of the printer before G code generation so that linear measurements taken

from the printed cube's sides reflected standard errors occurring on the related axis of the printer. For all cubes, errors related to the X and Y axes were in the range of 0 to +0.16mm, while errors on the Z axis were in a span from 0 to 0.1mm. These errors did not show any relation to the virtual 3D model size and were most probably the result of 3D printer design. The standard errors of the 3D printing process were dimensionally smaller than the scanning resolution or the volumetric reconstruction voxel of the radiological image, so they could not affect the study results. G-code files were prepared by importing the prepared solid surface 3D models into Cura software, version 4.0 (Lesser General Public License -LGPL). In the Cura 4.0 settings, the Creality Ender-3 3D printer was selected from the "Preset printers" menu, and the slicing settings were set to "Normal" mode, where the nozzle diameter was set to 0.4mm, the layer height was set to 0.15mm.

3.2.4. Linear and volumetric measurements on physical objects (mandible and 3D printed MM)

Linear and volumetric measurements were taken on radiological scans, 3D printed mandibular MM and dry mandible, all aligned with sagittal and coronal plane, as it was described previously. Firstly, eight anatomical landmarks were determined on dry mandible and then reproduced on MSCT, CBCT scans and MM 3D printed based on these scans. Then, five measures between these anatomical landmarks were established for comparison between dry mandible and each scan`s volume reconstruction and each 3D printed MM.

Anatomical landmarks were as follows:

a) Unilateral: most inferior (mentum - Me) and the most superior (interdentale - Id) point on the mandibular symphysis, most anterior point on the mandibular symphysis (pogonion – P), most posterior point on the mandibular symphysis.

b) Bilateral: most lateral points on the mandibular condyle (CDL), most posterior points on the mandibular condyle.

Between these anatomical landmarks, we analyzed the following linear measures: symphysial height (SH, Figure 3A), symphysial width (SW, Figure 3B), bicondylar width (BW, Figure 3C), left (L) pogonioncondyle line (from pogonion to the most posterior point on the left mandibular condyle -LPCL) and right (R) pogonioncondyle line (from pogonion to the most posterior point on the right mandibular condyle-RPCL, Figure 3D).

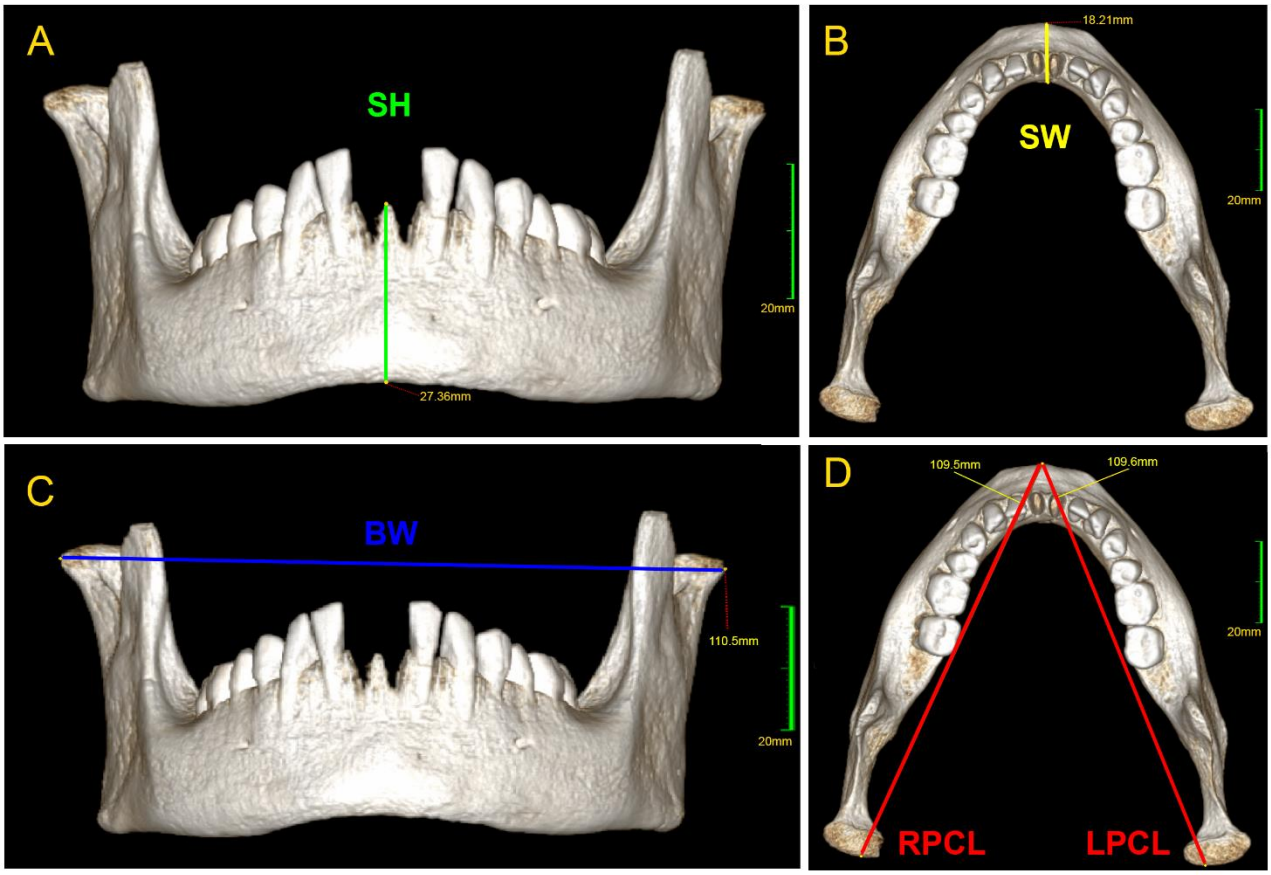

Figure 3: Positioning of the dry mandible during scanning and the procedure of 3D model creation ensured that SH measure is aligned with Z axis of the 3D model, SW is aligned with Y axis and BW with the X axis.

Linear measurements on dry mandible and MM were taken by digital caliper.

Following the method from work of Whyms and associates (Whyms et al. 2013), volume measurements on dry mandible and MM were taken by three separate water displacement trials. To prevent water from leaking in and underestimating the volume, the openings on the mandible and MM were covered with a thin layer of paraffin wax. Water displacement was measured on a digital scale, three separate measurements were taken and the mean value was used as a reference standard. Three trials were performed by one observer, in a one-week time span.

3.2.5. Linear and volumetric measurements on MDCT and CBCT scans

Linear and volumetric measurements on radiological scans were recorded using FDA-approved Carestream Vue PACS Power Viewer version 12.0.0.5756 in 3D application on reconstructed volume and following basic radiological principles in Multi-Planar Reformatting viewbox. Linear measurements analyses involved following measurements: BW, RPCL, LPCL, SH and SW. Volume measurements on DICOM data and 3D models derived from DICOM data were taken in Materialise Mimics software (Materialise NV, Leuven, Belgium).

Measurements on radiological scans were taken by two independent observers. The first observer was research associate and radiologist with PhD in Skeletal Biology, experienced in the field of oncology and paleoradiology. The second observer was teaching assistant and radiologist with PhD in Dental Medicine, experienced in the field of dento-maxillofacial

radiology. Intra-observer reliability was tested by repeated measurements in one month timespan.

The accuracy of all measures taken on CT, CBCT data and 3D models was measured by comparison to reference standard measured on human mandible by calculating the average relative error (ARE). Measurement ARE ≤ 0.05 are considered within experimental accuracy (Whims et al. 2013).

3.2.6. Correction of 3D model axis and volume

Average linear measurements on the mandible were compared to the same measures on the MM derived from DICOM images of the mandible. Average measure value, taken on the mandible, is considered to be 100% of the desired corresponding measure on the 3D model and MM. Correction percentage for every axis was calculated by dividing the value of corresponding measure on the mandible with one on the MM.

Example for 3D model axis and volume corrections:

SW measure corresponds to Y axis, its dry mandible value is 14.3425mm and its MM value for the CBCT0.25 radiological protocol is 14.865mm. Correction of the Y axis is then calculated by following formula:

1-(14.3425/14.865)=0.03515

Output value decimal number is expressed as a percentage (0.03515 = 3.515%). Value of standard deviation is recalculated as a percentage of average measure on the dry mandible: 0.0319/(14.3425/100)=0.2167%. And added to axis correction: 3.515% + 0.2167%=3.7317%. Finally, axis correction of Y axis for CBCT0.25 3D model is expressed with negative sign, since its SW measure is greater on the MM than on the dry mandible.

For calculating the volume correction, axis correction value for X, Y and Z axis of the 3D model or MM are added up and resulting volume correction percentage is applied to the volume value.

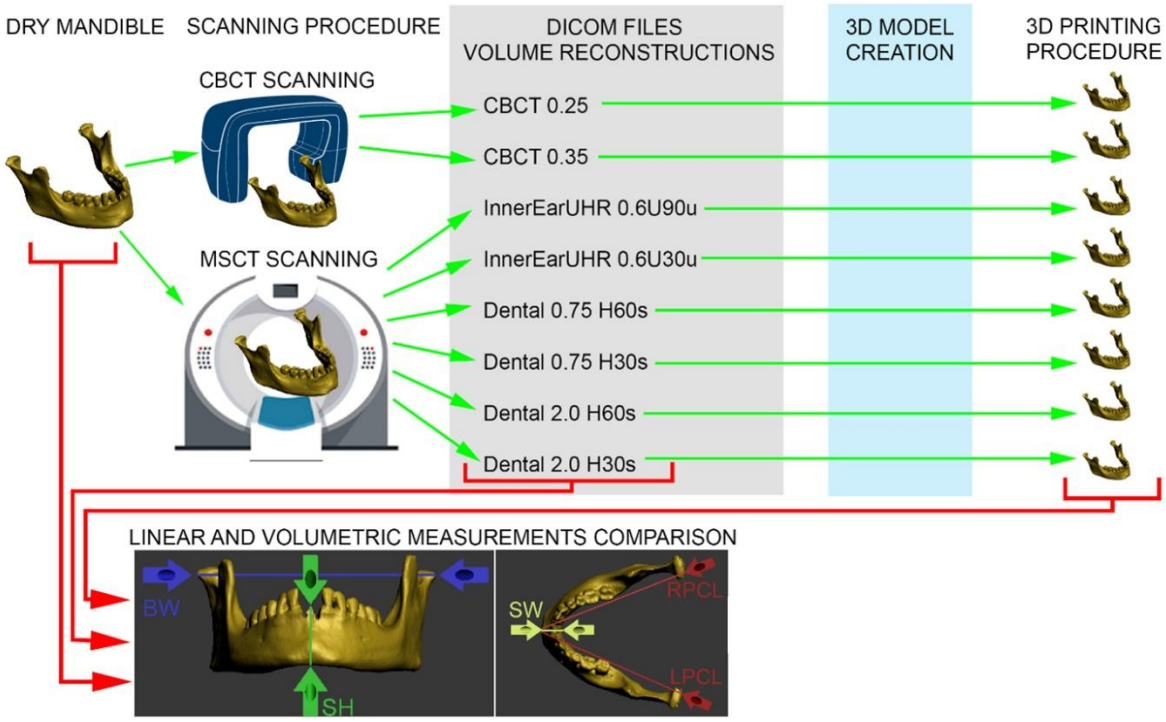

Figure 4: Graphical presentation of the first part of the research, showing measurement comparison

3.2.7. Bone replacement material synthesis and characterization

A novel bone substitute based on nHAP and PLGA, which mimics natural bone and can be resorbed by the body, was synthesized using a method described previously (Jokanovic et al. 2017), at Albos d.o.o. in Belgrade, Serbia. The nHAP was synthesized through a hydrothermal process using calcium oxide from eggshells and $(NH_4)_2HPO_4$. The eggshells were calcined at 900°C to remove carbon and the resulting powders were analyzed for their Ca, Mg, and P content, using adsorption atomic spectroscopy (PerkinElmer 3030B) and found to be 38.38 mass%, 1.11 mass%, and 0.2 mass%, respectively. A solution containing $Ca(OH)_2$ and $(NH_4)_2HPO_4$ was prepared, and the $(NH_4)_2HPO_4$ mixture was added to the $Ca(OH)_2$ mixture. The pH of the solution was adjusted to 7.4 using 0.1 M HCl or $(NH_4)OH$ and the solution was autoclaved at 150°C under 5x105 Pa pressure for eight hours. The resulting precipitate was dried, ground, washed, and ultracentrifuged to obtain pure nHAP.

To create the bone scaffold, 5g of nHAP and 1.5g of polyethylene-vinyl acetate/ polyethylene-vinyl versatate (PEVA/PEVV) were mixed and processed in the autoclave at 120°C for two hours. The resulting particles were filtered through a 200 nm pore size filter. The solubility, surface properties, pH value, micro-indentation properties and compressive strength of the nHAP granules were evaluated.

3.2.7.1 Solubility of the synthesized nHAP granules

Solubility of the nHAP granules was tested in Laboratory for Atomic Physics, Institute for Nuclear Sciences Vinca, University of Belgrade, Serbia. To observe the breakdown rate of nHAP granules, they were placed in a solution of phosphate buffer saline (PBS) with Tris buffer (tris hydroxymethyl-aminomethane) at a pH of 7.37. The speed of degradation was tracked by measuring the changes in calcium ion concentration using atomic absorption spectroscopy (Perkin Elmer 3030B). Samples of 3 ml of the solution were collected for multiple analyses at 10 and 30 minutes, one, four, and eight hours, one, two, five, and eight days, and 12, 15, 19, and 22 days after the granules were immersed. Each time a sample was taken, fresh PBS with Tris buffer was added to the solution to maintain a consistent volume. The results are depicted in Figure 5 and show how calcium ion concentration varies over time (Figure 5).

To compare the degradation rate of nHAP (the ceramic component of ALBO-OS) to that of biological apatite, the degradation rate in a fluid with a similar composition to bodily fluids needed to be established. The solubility product of nHAP was determined from the concentration of calcium ions in the saturation part of the curve and was found to be 7.85x10-44. This value is equivalent to the solubility product of biological apatite -BioOss(3.51x10-43, figure 6, indicating that the degradation rate of nHAP in ALBO-OS is comparable to that of natural bone.

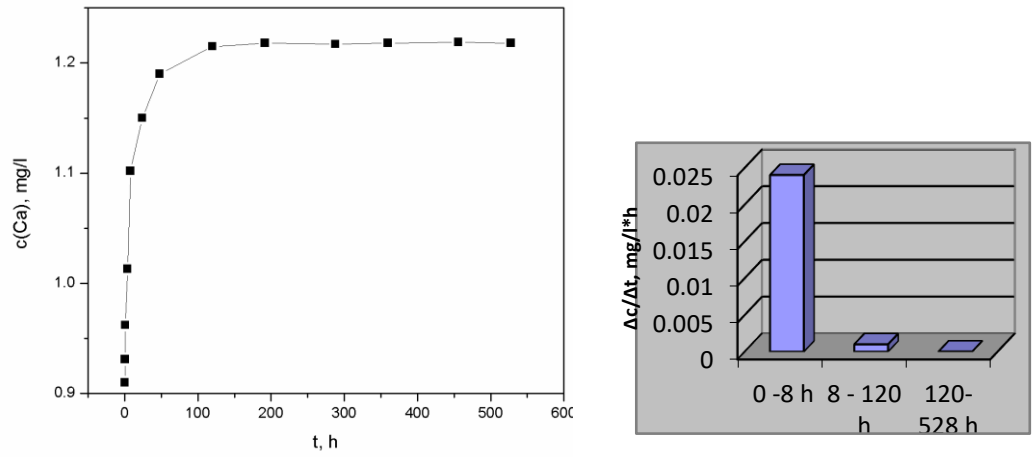

Figure 5: Time-dependent change of the Ca concentration in the solution containing investigated nHAP granules.

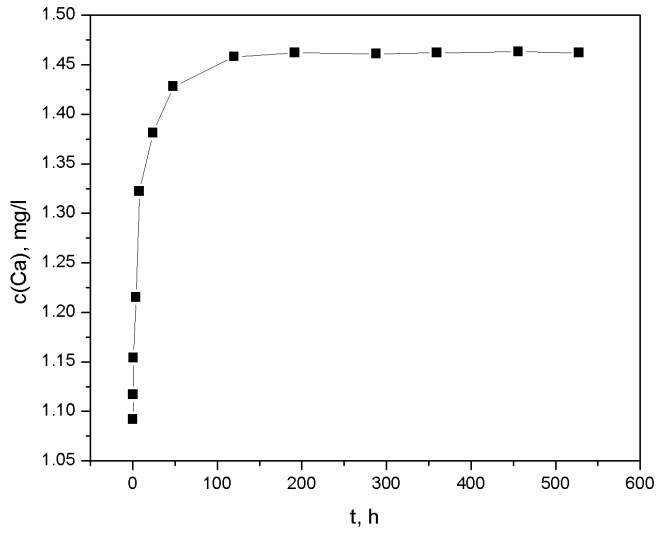

Figure 6: Change of the Ca concentration with time in biological apatite (BioOss).

In a static system it was shown that the dissolution rate for the first eight hours was the highest (0.024 mg/L per h), but after 120 hours, it was significantly lower (0.001 mg/l per h). After 528 h it was almost negligible ($7.4x10^{-6}$ mg/l per h). In the biological apatite, similar behavior was observed.

3.2.7.2. Compressive strength of the nHAP granules

The compressive strength test was done in Laboratory for Atomic Physics, Institute for Nuclear Sciences Vinca, University of Belgrade, Serbia, and involved measuring of the nHAP granules following various immersion periods in Hank's solution, a well-balanced salt solution that contains NaCl (8.00 g), $NaHCO_3$ (0.35 g), KCl (0.40 g), KH_2PO_4 (0.06 g), $MgCl_2x6H_2O$ (0.10 g), $CaCl_2$ (0.14 g), $Na_2HPO_4x2H_2O$ (0.06 g), $MgSO_4x7H_2O$ (0.06 g), glucose (1.00 g) in 1000 ml of distilled H_2O, and has a pH of 7.4. To determine the compressive strength, porous compacts of nHAP, with dimensions of 16 mm × 16 mm × 10 mm, were used. The specimens were immersed in a 10 ml solution for a predetermined period of time at 37 °C, and then their compressive strength was measured using Instron 5565, (Instron Corp., Canton, MA, USA). A total of 10 measurements were taken for each immersion period.

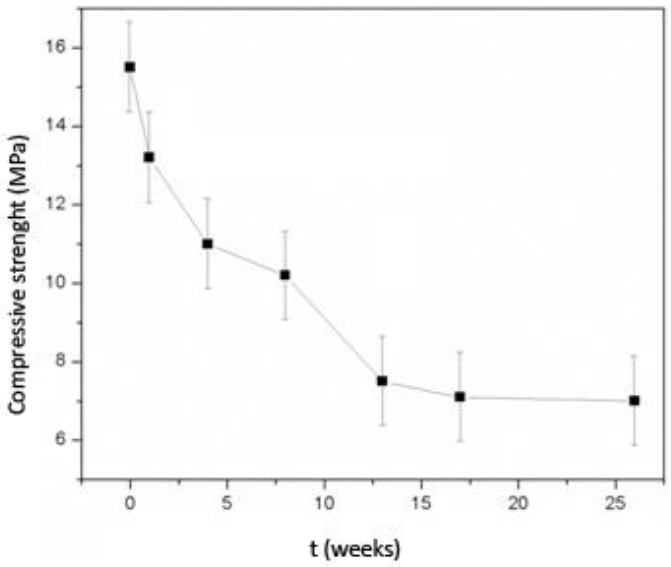

Figure 7: The correlation of the ALBO-OS compressive strenght and the time of the material's soaking in Hank's solution.

After 6 weeks in Hank's solution, the compressive strength decreased from 15.5 MPa to 7 MPa. From 13th to 26th week, changes were minimal (Figure 7).

3.2.7.3. Microindentation mechanical testing

Micro-indentation mechanical testing was done on Institute of Osteology and Biomechanics, University Medical Center Hamburg-Eppendorf, Germany, using a Biodent H RPI instrument (Active Life Scientific Inc, USA) on the polished nHAP block. The probe assembly was positioned on the surface of each cement specimen in a passive manner and tests were carried out according to the following measurement procedure: 2 N indentation force, 2 Hz indentation frequency, and 10 indentation cycles per measurement. The probe assembly calibration was done by making three indentations on a polymethyl-methacrylate block (Auburn Plastics and Rubbers, Inc., Indianapolis, IN, USA) after every 50 indentations. Seven specimens of ALBO-OS were subjected to indentation measurements. Several parameters were obtained as outcome variables: the first cycle indentation distance (ID), average unloading slope (Avg US), and indentation distance increase (IDI), the 1st cycle indentation distance (ID 1st, µm), 1st cycle unloading slope (US 1st), total indentation distance (TID, µm), indentation distance increase (IDI, µm), average creep indentation distance (Avg CID, µm), average energy dissipated (Avg ED, µJ), average unloading slope (Avg US), and average loading slope (Avg LS). The ID value was used to calculate the microhardness of the material by dividing the applied force over the estimated conical indentation area created by the test probe using the following equation of cone geometry:

$$microhardness = P/(\pi * r * \sqrt{r^2 + h^2})$$

where P is the constant load applied (2 N) and r and h are the first cycle ID values of radius and height obtained from the indenter.

The RPI results showed that the parameters obtained for nHAP correspond to some parameters found in the human skeleton. The microhardness of ALBO-OS (0.459 GPa) was in line with previous findings for human dentin (0.49 GPa) (Yassen et al. 2013). Additionally, the ID value in this study (10.13 μm) is in agreement with the result found for the human femur (12.64 μm), AVG CID (0.44 μm) is in accordance with 0.66 μm found previously, while IDI (3.54 μm) and AvgEd (1.81 μJ) are lower than that of IDI and AvgED of the human femur (1.28 μm and 2.5 μJ, respectively) (Milovanovic et al. 2014). Taken all RPI parameters into account it can be assumed that synthesized nHAP possess a high potential to mimics the human bone in micromechanical sense.

Table 2: Reference point indentation outcomes of the ALBOOS

MH (GPa)	ID 1st (μm)	US 1st (N/ μm)	CID 1st (μm)	TID (μm)	IDI (μm)	Avg CID (μm)	Avg US (N/ μm)	Avg LS (N/ μm)	Avg ED (μJ)
0.459	10.125	0.551	0.625	13	3.525	0.437	0.548	0.386	1.81

MH – microhardness, ID 1st - 1st Cycle Indentation Distance; US 1st - 1st Cycle Unloading Slope; CID 1st -1st Cycle Creep Indentation Distance; TID - Total Indentation Distance; IDI - Indentation Distance Increase; Avg CID - Avg Creep Indentation Distance; Avg US - Average Unloading Slope; Avg US - Average Unloading Slope; Avg LS - Average Loading Slope; Avg ED - Average Energy Dissipated.

3.2.7.4. Determination of pH value

To measure pH values of material extract, 1 g of nHAP granules were soaked in 5 ml of simulated body fluid (pH=7.4) and determined after 1 week and 1 month using pH/ORP meter (HI 2211, Hanna Instruments Inc, USA).

Table 3: pH of nHAP after soaking in simulated body fluid

	7 days	1 month
ALBO-OS	7.64	7.41
SBF	7.4	7

3.2.7.5. Scanning electron microscopy (SEM) and atomic force microscopy (AFM) of the nHAP

The microstructure and surface properties of nHAP were analyzed using scanning electron microscopy (SEM) and atomic force microscopy (AFM). SAM analysis was done at Laboratory for Microbiology, Center for Electron Microscopy, University of Novi Sad. AFM was done at Laboratory for Atomic Physics, Institute for Nuclear Sciences Vinca, University of Belgrade, Serbia. For SEM observations (SEM, JEOL JSM -5300, Peabody, MA, USA), the specimens were coated with a thin layer of gold using sputter coating. AFM analyses were conducted using NanoscopeIIIe controller (Veeco Instruments Inc., New York, NY, USA) AFM tapping mode using a commercial SNC (solid nitride cone) AFM probe (NanoScience

Instruments, Inc. Phoenix, Arizona, USA) having a resonant frequency of 275 kHz and force constant of 40 N/m. The number of lines per frame was 512, and the scan rate was 1 Hz.

SEM analysis revealed the presence of cylindrical-shaped particles with lengths ranging from 300-900 nm and widths of 180-250 nm. Pores with sizes between 90-300 nm were observed between the particles. AFM assessment showed a comb-like wall structure with channels measuring 10-30 μm in length and approximately 1 μm in width. The wall dimensions measured 30 μm in length, ~3 μm in width, and 3-5 μm in thickness.

3.2.8. 3D modeling and printing of the construct

A preoperative CBCT scan of the rabbit's ulna was obtained using the Scanora 3D scanner (Soredex, Tuusula, Finland), while the animal was anesthetized usig following parameters: 13mA, 90kV, and a voxel resolution of 0.2mm. Subsequently, a Standard Tessellation Language (STL) file was generated from the CT data using Slicer software version 4.3.1 and Blender (Autodesc Inc., USA) software. The resulting STL file was imported into Autodesk 3D Max 2010 (Autodesc Inc., USA).

To prepare the bone for the experiment, a plane cut was preplanned from 22 mm to 44 mm distally from the proximal end of the bone, perpendicular to the longitudinal axis of the bone. This resulted in a defect length of 22 mm and a diameter of around 7 mm, which is approximately one-quarter of the total length of the rabbit's ulna (88 mm). Based on this surface 3D model of the bone, a construct was modeled layer by layer using a maze forming algorithm.

3.2.8.1. Custom 3D printer fabrication

In order to print personalized bone construct for rabbit’s ulna, custom made 3D printer was fabricated in Center of Bone Biology on the basis of original Prusa I3 (Prusa Research, Czech Republic) design as a fused deposition modeling 3D printer (Figure 8).. Several important modifications had to be made to original design of Prusa I3 3D printer: robust single piece cubic aluminum frame was welded and used instead of original frame, axis rails are also scaled up – from original 8mm in diameter to 20mm in diameter and beside thermoplastic extruder – paste extruder for nHAP was made and added to the printer head, together with 45 vats of power air turbine on X axis carriage. Paste extruder for nHAP was made as a syringe extruder, driven by NEMA 17 stepper motor with 6:1 gear ratio and steel-glass syringe of 10cc. Increase in overall size, frame and thickness of the rails were done for stability and so that printer could carry both extruders and air turbine and print without vibrations.

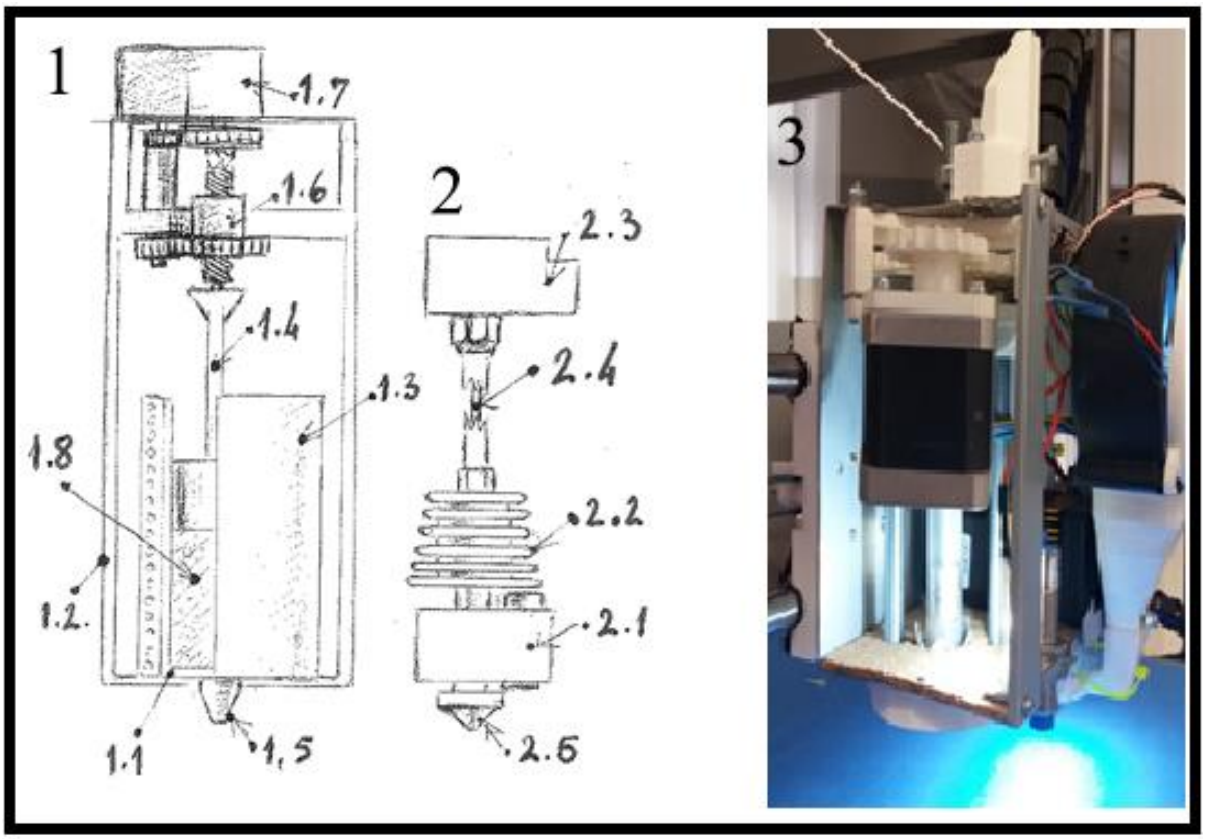

Figure 8: Schematic representation of the extruder design in custom made laboratory 3D printer: from technical reasons, 3D printer was modified to include two extruders: 1 – syringe extruder, 1.1 – glass syringe, 1.2 – external frame of the extruder 1, 1.3 – electrical heater coil, 1.4 –metal piston of the syringe, 1.5 – syringe nozzle (0,8mm in diameter), 1.6 – gears of the piston drive, 1.7 – piston drive motor with reduction, 1.8 – HAP PLA mixture, 2 – PLA extruder, 2.1 – heater block of the PLA extruder, 2.2 – extruder cooler, 2.3 – PLA extruder motor drive with reduction, 2.4 – PLA filament 1.75mm in diameter, 2.5 – PLA extruder nozzle 0,4mm in diameter. 3 - paste extruder attached to the head of the printer, with removed electrical heater coil, so the syringe with the metal piston can be visible.

3.2.8.2. Modeling the construct with desired porosity

To ensure the desired porosity and interconnectivity of pores in the customized bone replacement construct, we utilized the randomized Kruskal's maze generating algorithm (RKA) in combination with Piton software. By forming a planar maze structure in the x and z axes of the coordinate system (15x15mm), the RKA algorithm allowed us to control the porosity and total "bone" volume of the construct by adjusting the ratio of maze wall thickness to maze path width. The RKA algorithm also eliminated any enclosed cells in the planar maze structure by removing cell walls, ensuring interconnectivity of the pores.

We set the values of both the wall and path width of the maze to 225μm. After generating the 2D maze, we extruded the planar structure 225μm perpendicular to the Z-axis direction, creating a 3D object. We repeated the process of 3D maze generation, and the resulting objects were fused in the Z-axis direction until they exceeded the dimensions of the surface model of the bone construct (X-15mm, Y-15mm, Z-25mm), achieving additional random vertical interconnectivity of the maze cells. In this way, we created a 3D object of the

bone construct with 50% porosity and trabecular thickness of 225μm, where the maze walls represented the trabeculae of the construct, and the maze paths represented the voids.

We imported both the 3D models of the maze and the bone construct into Autodesk 3D Max software, where we immersed the bone construct model into the maze model and performed a Boolean union operation. This resulted in the formation of the 3D object of the bone construct. We then imported the model into Slice3R software (Affero Inc.) for G-code generation with the following settings: layer height of 0.2mm, 100% infill, printing speed of 10mm per second, shell thickness of 0, and no support material. To fabricate the bone construct, we used Pronterface software for 3D printing. We combined biodegradable PLGA as a support material with nHAP paste with gradually increasing percentages of nHAP towards the central part of the construct.

3.2.8.3. 3D micro porosity testing of the printed scaffold

In Center of Bone Biology, the fabricated structure was imaged using micro-computed tomography (Skyscan 1172, Bruker, Belgium) under following protocol: 100 kV, 100 μA, exposure time of 1200 ms,10 μm resolution, aluminum copper filter, rotating angle of 180° and 0.4° rotation steps. The resulting images were reconstructed using NRecon v.1.6.9.8 software (Skyscan-Bruker) with beam hardening correction of 45%, ring artefact correction of 6%, postaligment of -1, and smoothing of 4. After the reconstruction process, the CTAn 1.16.4.1 software (Skyscan) was used to analyze 3D images of the construct, with a global threshold set at 60 – 255 on the grayscale. The analysis yielded the following parameters: total porosity (%), closed porosity (%), open porosity (%), average pore size (μm), and connectivity density ($1/mm^3$).

3.2.8.4. Wettability of the construct

To evaluate the hydrophilicity of the construct in bodily fluids, two μl droplets of human plasma were deposited onto the surface of the material and analyzed using a contact angle measuring device (Institute for Nuclear Sciences Vinca, University of Belgrade, Serbia, where hydrophilicity assessment was also conducted) [17]. Human plasma was chosen as the reference liquid instead of distilled water as it better reflects the wetting characteristics of biological fluids, owing to the presence of proteins that cover the microfluidic channel walls [18]. However, a preliminary study demonstrated that it was impossible to determine the contact angle of the reference liquid on the surface of the manufactured HAP, as the HAP surface entirely absorbed the plasma in part of second (video in the supplement material). Therefore, instead of measuring contact angles, the time taken for the sample to fully absorb human blood was recorded.

3.2.8.5. Cytocompatibility assays

Assays were conducted at School of Dental Medicine, University of Belgrade, where the ISO standard 10993-5 was utilized to perform the mitochondrial activity assay. For the direct contact test, six specimens of 3D printed bone constructs were put in the wells of 96 well plates and submerged in 100 µl growth medium, to adjust the pH, for 24 hours. The next day, after the medium was removed, stem cells of the apical papilla (SCAP) were seeded onto the constructs and control wells at a concentration of 10,000 cells/100 µl. The plates were then placed in the incubator, at 37°C, with 5% CO2 for 72 hours. The 3-([4,5-dimethylthiazol-2-yl]-2,5-diphenyl-tetetrazolium bromide (MTT) cell metabolic activity assay (Sigma-Aldrich) was used to evaluate the cytotoxicity of the material. To measure cell metabolic activity, the growth medium was removed from the wells, and new growth medium, that contained 5 mg/ml of (MTT) was added. The cells were incubated in the dark at 37°C for 4 hours, and then, 100 µl dimetilsulfoxid (DMSO) was added to extract tetrazolium bromide salts from the cells' mitochondria. The absorbance was measured at 540 nm using an ELISA microplate reader (RT-2100c, Rayto, China).

The osteogenic differentiation experiment was conducted in compliance with the approval of the ethics committee (Faculty of Dentistry, University of Belgrade number 36/8). The attachment of cells to the manufactured constructs was examined using a human apical papilla stem cell-derived osteoblast cell line. The apical papilla tissue was collected with the informed consent of an 18-year-old patient undergoing extraction of an impacted third molar for orthodontic reasons. The tooth tissue was placed to Gibco Dulbecco's modified Eagle's F12 medium (D-MEM/F12; Thermo Fisher Scientific, Inc., Waltham, MA, USA), supplemented with 20% fetal bovine serum (FBS; Thermo Fisher Scientific, Inc.) and 1% antibiotic/antimycotic (ABAM; Thermo Fisher Scientific, Inc.) solution. 30 minutes after extraction, the tooth tissue was rinsed in phosphate-buffered saline (PBS; Sigma-Aldrich, St. Louis, MO, USA) and subjected to an outgrowth isolation technique as previously reported [19]. Sterilized constructs were immersed in growth medium for 24 hours at 37°C in 5% CO_2 to prevent pH changes before seeding. The medium was then removed, and stem cells were seeded onto the constructs at a concentration of 20,000 cells/10 µl. Growth medium was added after allowing the cells to migrate into the scaffolds for two hours. On the third day, freshly prepared osteogenic medium containing growth medium supplemented with 10 nM dexamethasone disodium phosphate, 1.8 mM monopotassium phosphate (KH_2PO_4), 10 mM b-glycerophosphate, and 50 µg/ml vitamin C (Sigma Aldrich, St. Louis, Missouri, USA) was added [20]. Cells were cultured for an additional 7, 14, and 21 days in osteogenic and growth medium, with the mediums being changed every 2 to 3 days. The experiment was performed in triplicate.

The scratch assay was used to assess cell migration *in vitro*. Extracts of the material under investigation were obtained by soaking the construct in Dulbecco's Modified Eagle Medium (DMEM) at a concentration of 0.1 g/mL and incubating it for 24 hours at 37°C in a humidified atmosphere of 95% with 5% CO2, according to ISO 10993-12. Serial dilutions of the extracts were made in DMEM at ratios of 1:1, 1:2, 1:4, 1:8, and 1:16. Single-cell suspensions were added to 24-well plates (2×105 cells/0.5 mL) and cultured for 3 days until reaching 80% confluence. Thereafter, the cells were incubated for 24 hours in medium containing 2% FBS to prevent proliferation of SCAP during the experiment. The following day, a sterile 1.2 mm wide rubber was used to scratch a wound in the cell monolayer across the center of the well in a straight line. The wells were then washed twice with PBS, and new 2% FBS medium and material extracts were added to the corresponding groups before being placed

in the incubator (37°C, 5% CO_2). Images were captured 1 and 24 hours after the scratch was made, using an inverted microscope (BIB-100/T, BOECO, Germany) with an HDCE-90D camera (BOECO, Germany). The closest area of the scratch was measured using Scope Image 9.0 software. The experiment was performed in triplicate.

The alkaline phosphatase (ALP) activity assay was carried out one week after osteogenic differentiation, utilizing the *pNPP* Alkaline Phosphatase assay kit (Sigma-Aldrich). Following the induction, the media was extracted, and the cell layers were washed three times with PBS. Afterwards, 0.1% Triton X-100 was utilized to permeabilize the cell layers overnight at 4^0C. The following day, a 50 µl lysate was mixed with 1 M diethanolamine buffer (pH 9.8, with 0.5 mM $MgCl_2$) that contained 1 mg/ml pNPP (4-nitrophenyl phosphate disodium salt hexahydrate). In each well, 100 µl of pNPP substrate was included. The plates were incubated at room temperature for 30 minutes until a yellow water-soluble reaction product was formed. To stop the reaction, 3M NaOH was added, and the absorbance was measured at 405 nm using an ELISA microplate reader (RT-2100c, Rayto, China). The ALP activity was normalized by the total protein concentration of each well, which was determined using a Biospec-nano (Shimadzu, Kyoto, Japan).

The impact of scaffold on the development of mineralized nodules was evaluated by using alizarin red S staining (ARS) technique. After 21 days, cells cultured in 96 well plates were treated with 4% neutral formalin buffer for 15 minutes and stained with 2% ARS , (Sigma-Aldrich, Germany). To determine the extent of mineralization, ARS bound to cells was extracted by incubation with 250 µl of 1% hydrochloric acid in 70% ethanol for 20 minutes. The absorbance was read at 450 nm in an ELISA microplate reader (RT- 2100c, Rayto, China). The absorbance of ARS bound to scaffolds cultured under the same conditions, but without cells seeded on them, was measured and subtracted from the groups with cells seeded on scaffolds to prevent false-positive results. After seven, 14 and 21 days of osteogenic differentiation, cells seeded on scaffolds were fixed with 2% glutaraldehyde for 2 hours at 4°C, dehydrated with increasing concentrations of ethanol (30%, 50%, 70%, 90%, 100%), each concentration for 10 minutes, and then gold coated before scanning electron microscopic analysis (JEOL, JSM-5300, Tokyo, Japan).

3.2.9. *In vivo* implantation of the personalized construct in rabbit's ulna

Firstly, the New Zealand White adult rabbit was scanned to obtain DICOM data for designing the bone construct. It then underwent intramuscular premedication using a combination of Ketamidor (Ketamine hydro-chloride) 10% (Richter Pharma Ag, Austria) at a dose of 35mg/kg, and Ksilazin (Xylased) 2% (Bioveta, Czech Republic) at a dose of 5mg/kg. For analgesia, Butorfanol at a dose of 0.1 mg/kg (Richter Pharma Ag, Austria) was used. A linear 3.5 cm skin incision was made in the ulnar area under local anesthesia (Lidokain-hlorid 2%, Galenika a.d. Srbija). The soft tissues were lateralized and the ulnar bone was exposed. Afterward, an osteotomy was made through the entire thickness of the bone using a bur (length of 22 mm), according to the previous virtual planning and use of resection SG. The construct was designed to exactly correspond to the shape of the defect, which was made at a known distance from the proximal part of the ulna (30 mm). A 3D-printed bone construct, sterilized with ultraviolet light for 12 hours, was implanted in the rabbit's ulna using SG, without any SC or GF added. The surgical wound was closed on multiple tissue levels with interrupted sutures (Vicryl, Ethicon, 3-0).The rabbit was placed in an enclosed comfortable surrounding after the surgery and had *ad libitum* access to food and water. It resumed its normal routine, activities,

and appetite within three days following the surgery. The incision site was clean, as was the surrounding skin. The surgical sutures on the skin were removed ten days after the operation. During the five-day postoperative period, 0.1 mg/kg Buprenorphine (twice a day) and oxytetracycline 20 mg/kg were administered subcutaneously for pain and infection control. To assess pain, a rabbit grimace scale, which is a standardized behavioral coding system that evaluates facial expressions, was used (Keating et al. 2012). The rabbit was sacrificed 12 weeks after the surgery. The implanted construct and 10 mm of the surrounding old bone tissue of ulna were sampled and fixed in 4% neutral formalin for further analyses (Figure 9). Complete procedure was done at the Faculty of Veterinary Medicine, University of Belgrade.

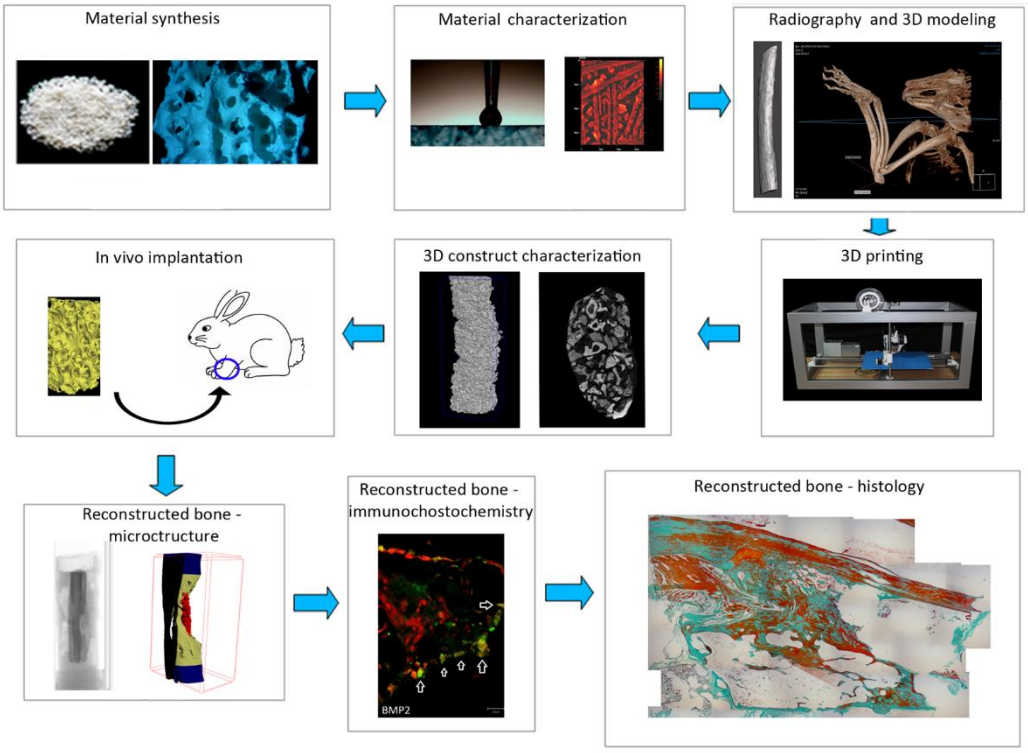

Figure 9: Graphical presentation of second phase of the research, describing its main steps from material synthesis to characterization of the bone material taken from the reconstruction site on the rabbit's ulna.

3.2.10. Radiography and micro-CT evaluation

An X-ray image of the rabbit's ulna was taken while animal was under anesthesia using a ZooMax White DR machine (Control-X Medical, Ltd.) in a medio-lateral projection. The imaging parameters used were 47kV, 6.4mAs, and a focus-to-film distance of 70cm. The resulting X-ray images were digitized using a CR10-x scanner (Agfa HealthCare NV, Septestraat 27, B-2640 Mortsel - Belgium). After seven days of fixation, the sampled material was evaluated using micro-CT (SkyScan) imaging, performed in Center of Bone Biology, using the following parameters: 65 kV, 153 μA, exposure time of 640 ms, an aluminum-copper filter, rotating 180° in 0.4 steps, and a resolution of 10 μm. The images were then reconstructed using CTAn 1.16.4.1 software (Skyscan, Bruker). The new and old bone tissues and bone construct were reconstructed separately using appropriate global threshold ranges. Given that the bone characteristics in the defect region (new bone) are likely different from those in the surrounding region (old bone), micro-architectural parameters were determined in each area,

including total porosity (%), closed porosity (%), open porosity (%), cortical thickness (mm), connectivity density (1/mm^3), average pore size (μm), and pore size distribution (%).

3.2.11. Histological and histomorphometric analysis

Specimens for histological analysis were prepared using a standard procedure, which included fixation in 4% buffered formaldehyde, decalcification in formic acid, dehydration, and embedding in paraplast, at Faculty of Dental Medicine, University of Belgrade. Longitudinal sections of 4μm thickness were obtained and stained with hematoxylin and eosin, Goldner trichrome, which is suitable for bone tissue presentation, and Toluidine Blue, which is suitable for assessing bone vitality.

To assess the difference in regeneration efficiency between the central and peripheral regions of the defect, histological and histomorphometric parameters were determined in both areas. Four sections with a spacing of 50 μm were made and analyzed from both the central defect region and the peripheral defect region. At a final magnification of 400x Morphometric assessment was performed, and two-dimensional photographs were taken using a digital camera (Leica DFC295, Germany). Histological and histomorphometric analyses were conducted using a light microscope (Leitz Labor Lux S Fluorescence Microscope, Ernst Leitz Wetzlar GMBH, Germany) and a software package (Leica University Suite, version 4.3, Leica Microsystems, Germany), respectively.

The parameters evaluated during histological and histomorphometric analyses included the presence, total area, and histological characteristics of newly formed bone tissue (NFB), which is the most important parameter for bone regeneration performance. Additionally, the total surface of mineralized (MSA) and non-mineralized bone (NMSA) was assessed using the Goldner trichrome method, which allowed non-mineralized bone to be displayed in the red spectrum and mineralized bone in the green spectrum. The presence of non-mineralized bone is important in evaluating active osteogenesis and bone remodeling. The total surface of newly formed bone marrow (NFBSA), graft (GPA), and connective tissue particles (CNT) were also evaluated. Finally, the presence and number of inflammatory infiltrate cells, the most important parameter of the tested material biocompatibility *in vivo*, was assessed.

3.2.12. Immunochemical staining for confocal microscopy

At Faculty of Dental Medicine, University of Belgrade, slides were prepared from formalin-fixed and paraplast-embedded rabbit tissue sections. These slides were treated with a series of alcohol solutions including xylene, absolute, 96%, 70% ethanol, and distilled water for a duration of 2x5 minutes each to deparaffinize them. The antigenicity of the tissue was then retrieved using an antigen demasking solution (Vector Laboratories, USA) by heating the sections at 90°C for 25 minutes. To prevent nonspecific staining, the sections were treated with a solution of 5% BSA solution in PBS (Sigma-Aldrich, Germany) for 30 minutes before application of primary and secondary antibodies. Primary polyclonal anti-rabbit antibodies against osteopontin (OPN), bone morphogenetic protein 2 (BMP2), and osteocalcin (OCN) (Thermo Fisher Scientific) were applied to the sections, which were then incubated for 24 hours at 4°C. This was followed by incubation with an appropriate secondary Alexa Fluor 488-conjugated antibody (Thermo Fisher Scientific) for one hour in a dark humidified chamber.

Propidium iodide (Thermo Fisher Scientific) was added to the sections to stain the nuclei. Sections were washed three times in PBS for 5 minutes after each step. The sections were covered with fluorescent mounting medium (DAKO, Glostrup, Denmark) and examined under a confocal microscope (Laser Scanning Microscope, LSM META 510, Carl Zeiss, USA) with a 20x or 40x objective lens. Incubation with 5% BSA was performed for negative control staining for the secondary to confirm the specificity of the staining.

3.2.13. Clinical implementation of virtual surgical planning, medical models and surgical guides

In third part of research, we used the radiological protocol and technical procedure that we previously determined as the most adequate for MM and SG fabrication on seven patients who underwent surgical treatment for large bone defects of the mandible at the Clinic for Maxillofacial Surgery at the Faculty of Dentistry, University of Belgrade to test the implementation of the procedure in a clinical environment. Although the methods we used are universal and not limited to mandibular region surgeries only, we focused on mandibular defect reconstruction cases for the sake of uniformity and comparability of the results of the experimental and practical parts of the research.

In short, preoperatively, all patients underwent CT scans (CBCT or MSCT scans were used for mandibular region, and MSCT with angiography contrast were used for fibula as the donor site). Obtained DICOM files were imported to 3DSlicer software for segmentation and the process of 3D model creation. After generation of suitable STL files for experimental group of patients, files were imported in to Autodesk Meshmixer and 3DStudio Max program for the procedure of surgery planning and SG 3D model creation. After localizing the lesions on the 3D mesh, during surgery planning with operating surgeon, safe zone borders were determined and cutting guides were modeled (Figure 10). Anatomical landmarks like mandibular ramus and mandibular angle, as well as present teeth were used to position each guide on the mandible. Distal end and lateral malleolus of fibula were used as anatomical landmarks for the donor site. To identify most suitable regions of the donor site, 3D models of recipient and the donor site were imported in to Autodesk 3D Studio Max software where series of superimposing of two regions were done in order to plan the cutting plains and cutting angles in such fashion that the resulting auto-graft minimally alters the form of both recipient and donor region, preserving the necessary vascular structures in the process. Cutting planes were determined in silico and virtual resections were done in both donor and recipient region. For all cases, we modeled the most desirable morphology of the graft and resection planes to accomplish the best functional and aesthetic results. By this technique, even in cases of severe destruction of the mandible by malignant disease, natural margins of the mandible could be preserved which is enough to define proper outer borders of the graft and make latter comparison between the mandible before and after surgery. In the cases where the outer shape of the mandible was preserved, 3D model derived from the preoperative MSCT or CBCT was used as an ideal “mold” for the designed shape and size of the autograft. In one case of traumatic fracture, where part of the mandible was resected previously and where no radiological scan prior to the injury was done, shape and position of the missing part of the mandible was restored by the mirroring technique, occlusion and condyle position.

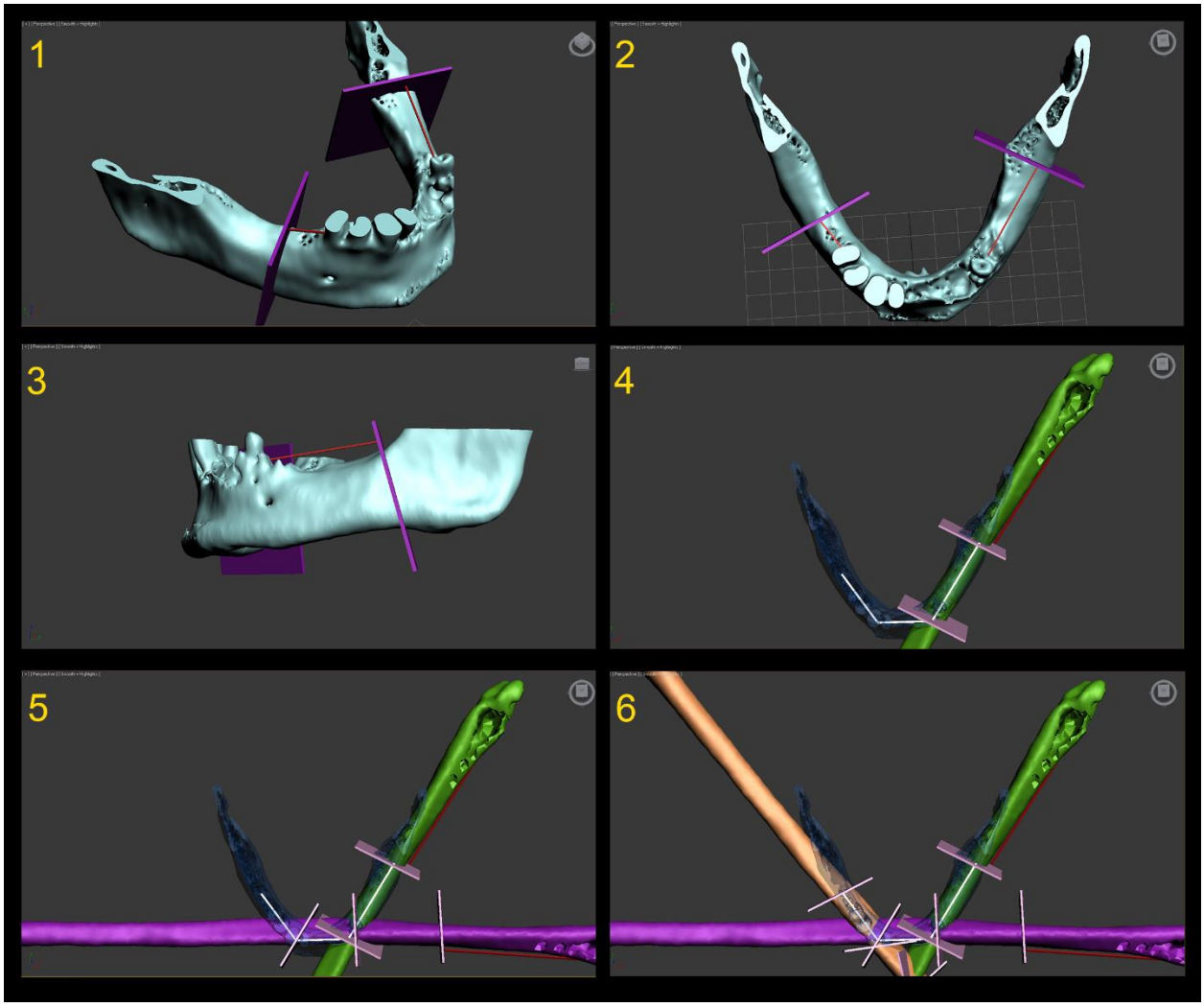

Figure 10: Virtual surgery planning procedure.1-3; identifying the „safe zone" 20mm from alterations borders visible in the bone and positioning the resection planes (subsection 1-3 purple color) in Autodesk 3D Max software on the 3D model of the mandible (subsection 1-3 pale blue color). Red arrow lines, visible on subsections 1-3 are distance measurements based on anatomical landmarks of existing teeth. Aligning of the donor region with the recipient region starts by importing the 3D model of the donor region (subsections 4-6, green color) to the 3D max scene with 3D model of the mandible (subsections 4-6 transparent blue color) and aligning it the best possible way with the first part of the recipient region. In this phase the left mandibular resection plane becomes the first resection plane for the donor region, and on the base on 3D shape of the mandible – second cutting plane on the donor region is determined. During next steps, illustrated on subsections 5 and 6, copy of the donor region is made (marked with purple color in subsection 5 and orange color in subsection 6) with the cutting planes determined in the previous step attached, and translated to the next part of mandible to be reconstructed in such way that contact points of the second donor region cutting plane and its copy, that in this way became the third cutting plane, allow for minimal tissue loss of the donor region with optimal mimicking of the recipient region shape and volume. Described steps include multiple perspectives in the 3D space, in order to check for the optimal fitting of the donor and recipient region, as well as importing 3D models of the vascular structures, but the top perspective was chosen for subsections 4-6 for clear and comparable presentation of the procedure steps.

After resection planes for both recipient and the donor region are determined, based on their position and the attached thickness of 1mm (because of predicted bone loss due to resection), SG are modeled in Autodesk 3D Studio Max.

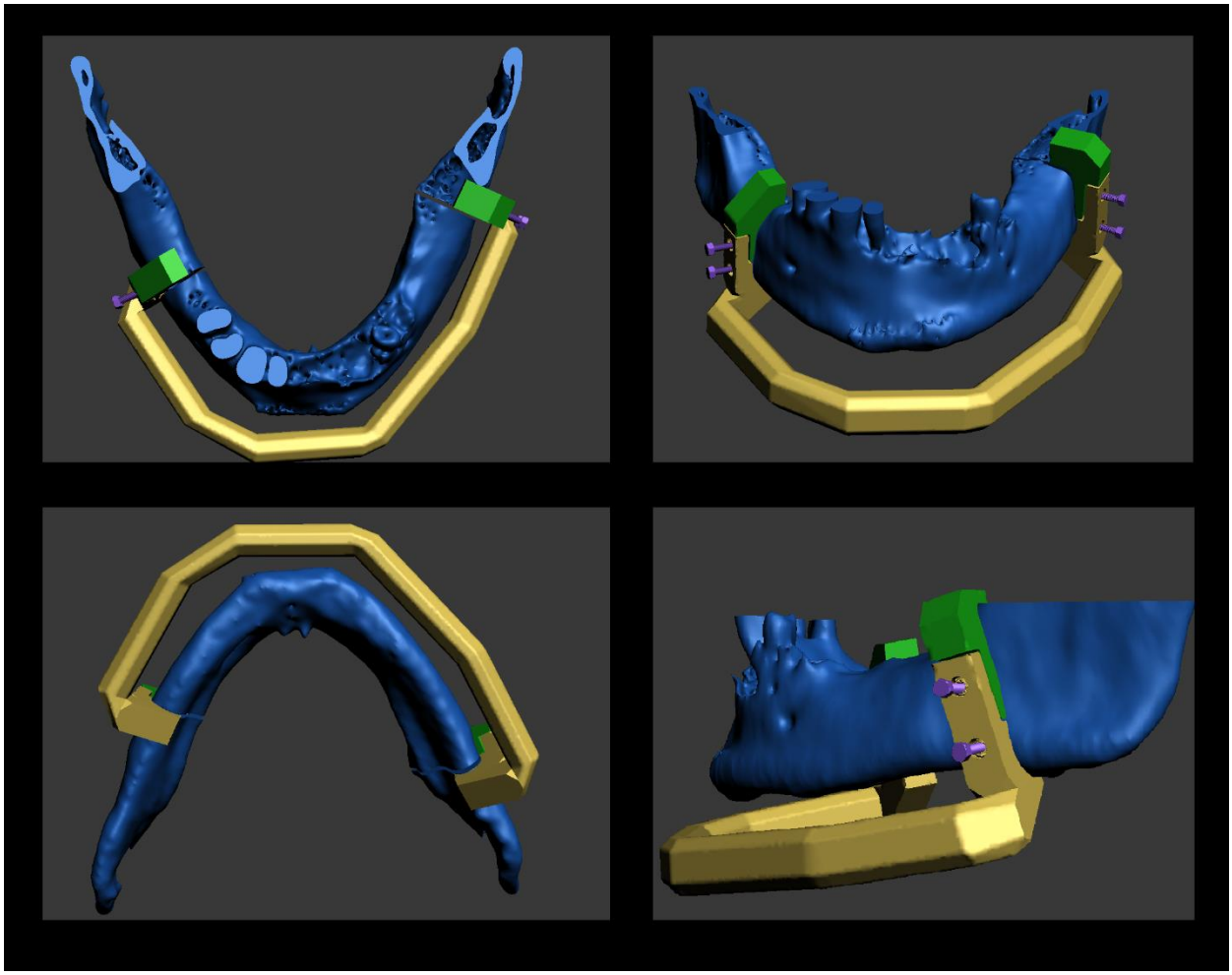

Figure11: 3D modeling of the SG and MM. Ideal-type example of the two component, or two-in-one mandibular SG. Resection is done virtually, visible on the blue color body of the mandible, along the mesial border of the green and yellow SG attachments. Parts of the SG that are in contact with mandibular body are shaped to fit exactly the topography of the mandible on the place of contact. The first component, yellow, arc shape body of the mandibular SG enables fixation after resection, ease of access and manipulation during whole operation. The second, green component, can be removed after resection to allow for auto graft to be placed and fixed with appropriate titanium plates.

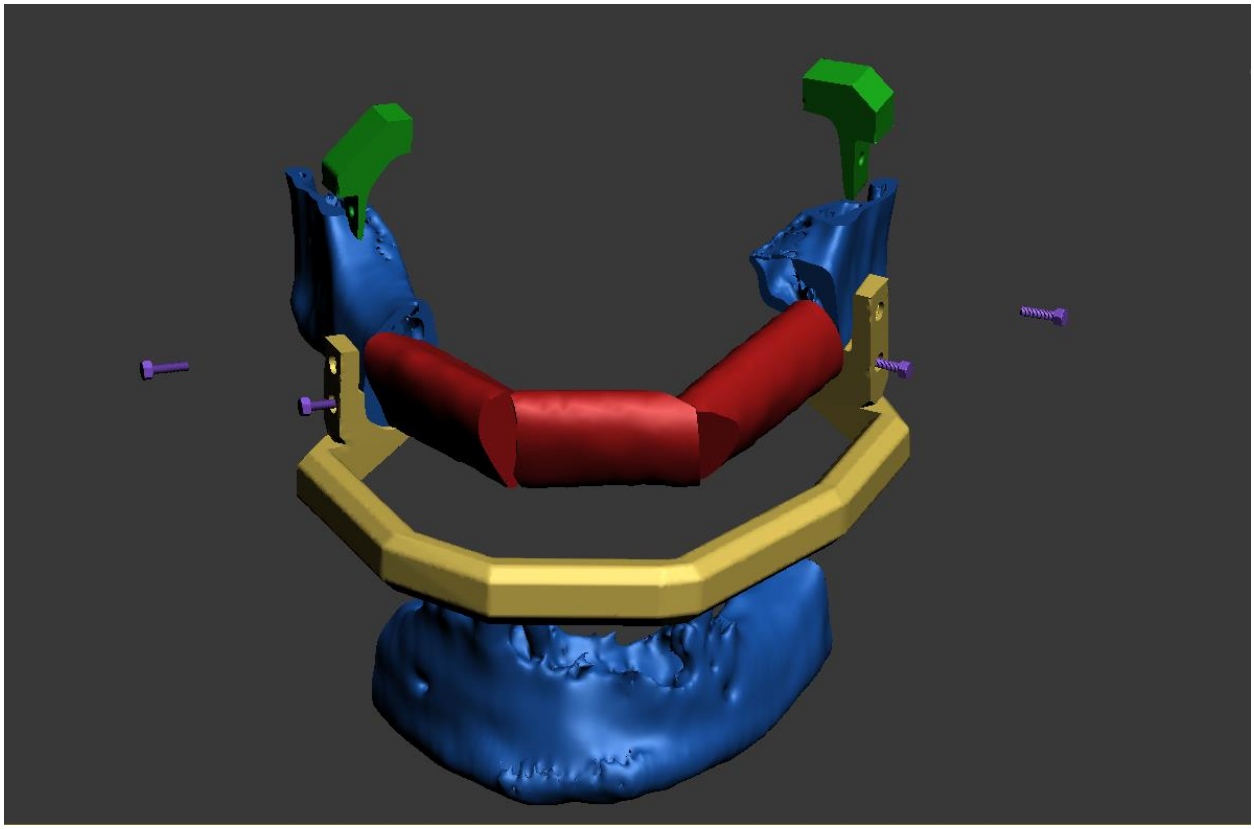

Figure 12: 3D modeling of the neomandible with SG. Removing the middle part of the mandible (blue color) after resection, detachment of the screws that hold the second component (green color) of the mandibular SG in place and removing it, while the first component (yellow color) of the mandibular SG holds the remaining parts of the mandible in the correct position. Placing the auto graft (red color) in the correct position.

MM of the mandibular region before and after the resection, as well as MM of the donor region are made to test fitting of the SG preoperatively to ensure successful bone replacement.

Figure 13: MM of the fibula donor site and fitting of the fibular SG, as part of the preoperative surgery planning. Distance from the distal end and lateral malleolus was used as the positioning landmark for SG. Placing of the fibular SG is secured with two 1,5mm diameter screws, preplanned in the SG design.

Figure 14: MM of the mandible, with single component resection SG placed in the process of the preoperative planning. Mandibular angle was used as anatomical landmark for SG placing. SG was secured on the MM with two 1,5mm diameter screws, using holes preplanned on the SG.

In the cases of secondary mandibular resection, with discontinuity of the mandible, 3D models of the patient mandible were duplicated and imported in to Autodesk 3D Max software, where each copy was assigned different color pattern and volumes were virtually overlapped. Mandibular ends from one of the 3D models were then virtually moved to most suitable position according to the condyle position in the mandibular fossa and the upper jaw:

Polylactic acid (PLA), material we use for MM and SG production, because it is proven as safe and biodegradable plastic, and commonly used for 3D printing in biomedical purposes. (Elsawy et al., 2017). Because of its biodegradability, it is used as a slow-release carrier of drugs and medications (Schliephake et al. 2008), as a membrane for guided tissue regeneration (Robert et al. 1993), for making antibacterial membranes for bone regeneration purposes (Pierchala et al. 2017) or as a base for porous scaffolds for bone regeneration (Gandolfi et al. 2018).

After 3D printing, surgical guides are subjected to UV and chemical sterilization before use.

3.2.14. Evaluation of clinical implementation of virtual surgical planning, medical models and surgical guides

To evaluate the results of MM and SG clinical use, following parameters were recorded in both experimental and control group of patients:

1. Surgery time or surgery duration (recorded in minutes)
2. Time of hospitalization (recorded in days)
3. Surgical complications
4. Final functional and aesthetic result
5. Patient satisfaction by the surgery, assessed on the scale from 1 to 5

Final functional and aesthetic result was assessed by comparing patient mandible pre- and post-surgery. Comparison was done by superimposing pre- and post-operative 3D model of the patient mandible in Autodesk 3D max software. Pre-operative 3D model of the mandible was used as an ideal situation for the patient, as in preoperative virtual planning. In cases of secondary resection, CT or CBCT predating first operation was used. Healthy side of the mandible on both pre- and post-operative 3D model was used as a marker for overlapping two 3D models. Orthogonal AP and lateral projection of the overlapping 3D models was used to record lateral and anterior-posterior linear measure deviation. BW, bi-gonial with and SH were used to reconstruct the AP and lateral projection of the mandibular 3D model. Different color and transparency were used for easier measuring. After linear measuring, 3D models of pre- and post-operative mandible were solidified to eliminate inner voids. Volume of the neomandible was calculated by virtual resection. By Bulian operation of subtracting two volumes: discrepancy between neomandible volume and the volume of preoperative mandible was recorded as an indicator of precision.

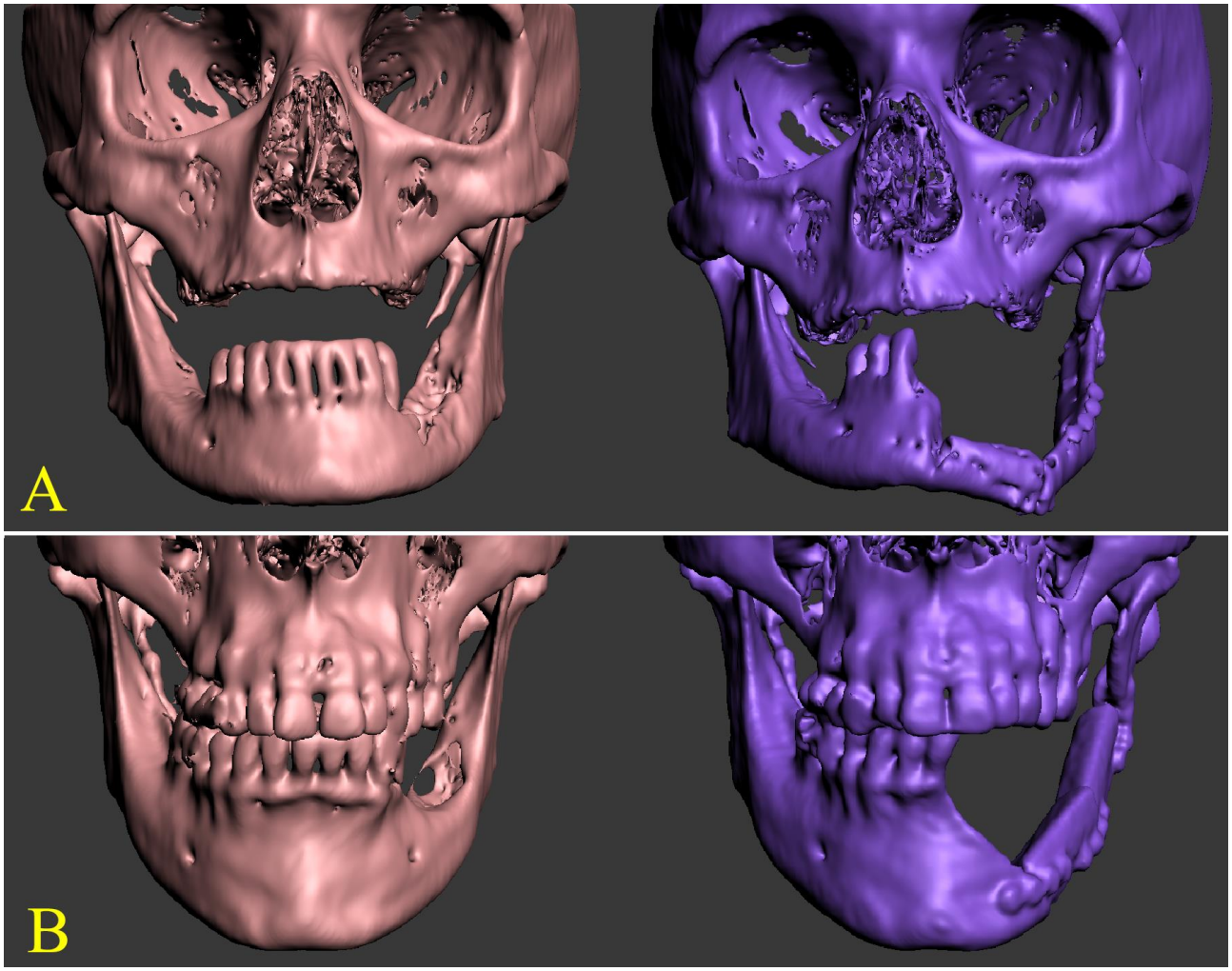

Figure 15: AP perspective of pre-operative 3D model of the mandible on the left, post-operative 3D model of the mandible on the right. A – patient from the control group, B – patient from the experimental group.

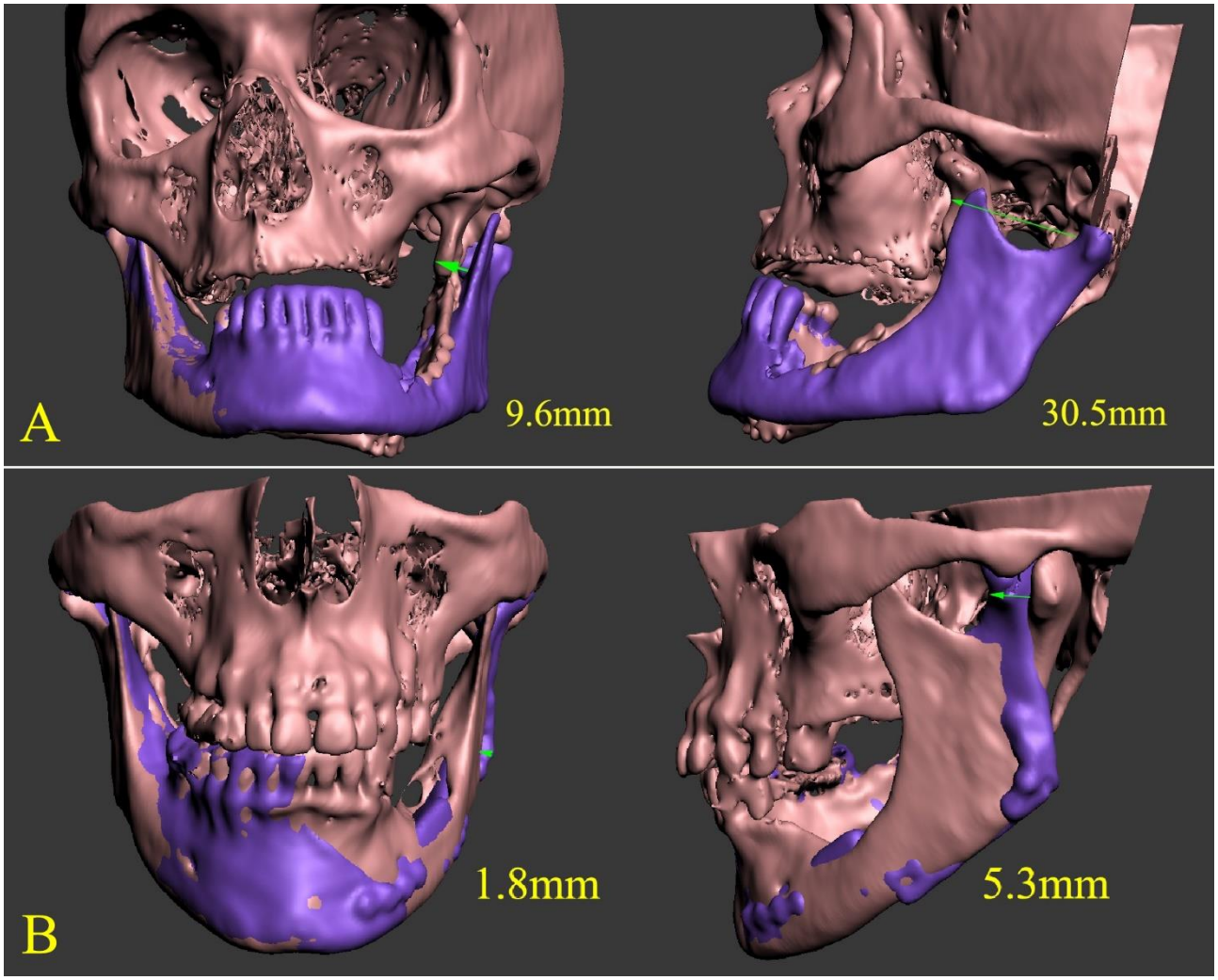

Figure 16: Overlapping of pre-operative and post-operative 3D models of the mandible, AP and lateral perspective, representing same patients as on previous figure. A – patient from the control group, B – patient from the experimental group. Green arrows represent sites of largest discrepancies.

3.2.15. Statistical analyses

Statistical analyses were made in Statistical Package for the Social Sciences software (SPSS, version 17.0, for Windows operative system), with 95% confidence interval and statistical significance level of 5%. The Kolmogorov–Smirnov test was used to assess the data distribution normality.

Intraclass Correlation Coefficient (ICC) test was used to determine intra- and inter-observer reliability for measurements taken on both digitally on MSCT/CBCT scans and on physical models (dry mandible and 3D printed medical models). One sample t-test was used to estimate the significance of the difference between MSCT/ CBCT scans and scanned mandible, as well as between 3D-printed MM derived based on MSCT/CBCT scans, and scanned mandible.

For cytotoxicity assay tests, one-way analysis of variance (ANOVA) was used to compare values between the groups. A paired sample t-test was used to compare the micro-CT porosity data found in new bone to that found in old bone as well as to compare the histomorphometric data found in the central and peripheral parts of the reconstructed bone defect.

During evaluation of clinical implementation of virtual surgical planning, MM and SG, independent samples t -test was used to compare the clinical outcomes between experimental and the control group. Due to nonhomogeneous variance of data regarding time of hospitalization, nonparametric Mann-Whitney U test was used for comparing for experimental and the control group.

4. Results

4.1 3D model creation procedure

The DSI value of the described segmentation process in 3DSlicer software was 0.97, indicating a high accuracy or high similarity between the binary mask representing the actual dry mandible image and the 3D models created by the segmentation process.

4.2 Measurements on dry mandible and 3D-printed medical models

All measures taken are listed by radiological protocols, assessed by the tested visualization and measuring techniques and compared to the reference standard. Measures are expressed as a numerical and ARE values (Table 4 and Table 7).

Differences of linear measures of both MM and CT/MSCT scans from the reference standard were analyzed by one-sample T-test, for the test value of 0, of the results in columns *3D-printed Medical Models – Mandible* and *CT, CBCT 2D – Mandible* in Table 4. The analysis demonstrated highly significant values, p=0.000 and p=0.001, respectively. In contrast, p values of one-sample t-test with the test value of 0, for the individual differences of measurements of every MM and the mandible from Table 4 were as follows: CBCT0.25: 0.745, CBCT0.35: 0.572, InnerEarUHR0.6 U90u: 0.74, InnerEarUHR0.6 U30u: 0.080, Dental 0.75 H60s: 0.110, Dental 0.75 H30s: 0.104, Dental 2.0 H60s: 0.239, Dental 2.0 H30s: 0.063. One-sample t-test, for the test value of 0, of the results (*(3D-printed Medical Models – Mandible) – (CT, CBCT 2D – Mandible)*) shown in Table 4, showed no statistical significance (p=0.566).

Table 4: Linear measures on the mandible, scans and medical models

Radiological protocol linear measure	Linear measure value on 3D-printed medical models (mm) / ARE value	Linear measure value on dry mandible (mm)	3D-printed medical model – Dry mandible (mm)	CT, CBCT 2D measures (mm) / ARE value	CT, CBCT 2D – Dry mandible (mm)	CT, CBCT 3D measures (mm) / ARE value	CT, CBCT 3D – Dry mandible (mm)	(3D-printed medical model – Dry mandible) – (CT, CBCT 2D – Dry mandible) (mm)
CBCT0.25 SH	27.2600 / 0.0036	27.3575	-0.0975	26.4825 / 0.0320	-0.8750	48.0375/ **0.7559**	20.6800	-0.7775
CBCT0.25 SW	14.8650 / 0.0364	14.3425	0.5225	14.9375 / 0.0415	0.5950	19.5250 / **0.3613**	5.1825	-0.0725
CBCT0.25 BW	107.1450 / 0.0070	107.91	-0.765	107.3750 / 0.0050	-0.5350	109.925 / 0.0187	2.0150	0.2300
CBCT0.25 RPCL	114.5025 / 0.0039	114.055	0.4475	114.3000 / 0.0021	0.2450	111.4500 / 0.0228	-2.6050	0.2025
CBCT0.25 LPCL	113.3975 / 0.0049	113.955	-0.5575	113.5250 / 0.0038	-0.4300	110.7250 / 0.0283	-3.2300	0.1275

CBCT0.35 SH	27.6675 / 0.0113	27.3575	0.3100	25.7700 / **0.0580**	-1.5875	48.1150 / **0.7587**	20.7575	-1.2775
CBCT0.35 SW	15.0275 / 0.0478	14.3425	0.6850	14.9675 / 0.0436	0.6250	20.6325 / 0.4386	6.2900	0.0600
CBCT0.35 BW	107.1275 / 0.0073	107.91	-0.7825	107.3250 / 0.0054	-0.5850	108.8000 / 0.0082	0.8900	0.1975
CBCT0.35 RPCL	113.4425 / 0.0054	114.055	-0.6125	113.8500 / 0.0018	-0.2050	109.8250/ 0.0371	-4.2300	0.4075
CBCT0.35LPCL	113.4775 / 0.0042	113.955	-0.4775	113.6250 / 0.0029	-0.3300	110.9750 / 0.02615	-2.9800	0.1475
InnerEarUHR 0.6U90u SH	26.6250 / 0.0268	27.3575	-0.7325	27.3275 / 0.0011	-0.0300	43.2675 / **0.5816**	15.9100	0.7025
InnerEarUHR 0.6U90u SW	14.7350 / 0.0274	14.3425	0.3925	14.9250 / 0.0406	0.5825	29.3350 / **1.0453**	14.9925	-0.1900
InnerEarUHR 0.6U90u BW	107.1075 / 0.0074	107.91	-0.8025	106.2750 / 0.0151	-1.6350	106.7750 / 0.0105	-1.1350	-0.8325
InnerEarUHR 0.6U90u RPCL	112.7425 / 0.0115	114.055	-	113.6000 / 0.0040	-0.4550	110.7250 / 0.0292	-3.3300	0.8575
InnerEarUHR 0.6U90u LPCL	112.4725 / 0.0130	113.955	-1.4825	113.3250 / 0.0055	-0.6300	110.2250 / 0.0327	-3.7300	0.8525
InnerEarUHR 0.6U30u SH	26.5550 / 0.0293	27.3575	-0.8025	26.9500 / 0.0149	-0.4075	44.5850 / **0.6297**	17.2275	0.3950
InnerEarUHR 0.6U30u SW	14.8050 / 0.0322	14.3425	0.4625	15.0550 / 0.0497	0.7125	29.4925 / **1.0563**	15.1500	-0.2500
InnerEarUHR 0.6U30u BW	105.7875 / 0.0197	107.9100	-2.1225	105.6500 / 0.0209	-2.2600	109.8750 / 0.0182	1.9650	-0.1375
InnerEarUHR 0.6U30u RPCL	113.0625 / 0.0087	114.0550	-0.9925	113.3250 / 0.0064	-0.7300	111.5500 / 0.0220	-2.5050	-0.2625
InnerEarUHR 0.6U30u LPCL	112.0575 / 0.0167	113.9550	-1.8975	113.1000 / 0.0075	-0.8550	111.2000 / 0.0242	-2.7550	-1.0425
Dental 0.75 H60s SH	26.5000 / 0.0313	27.3575	-0.8575	27.1450 / 0.0078	-0.2125	41.2650 0.0078	13.9075	-0.6450

Dental 0.75	14.9350 /	14.3425	0.5925	14.8475 /	0.5050	28.1100 /	13.7675	0.0875
H60s SW	0.0413			0.0352		**0.9600**		
Dental 0.75	106.6275 /	107.9100	-1.2825	107.0750	-0.8350	107.7500	-0.1600	-0.4475
H60s BW	0.0119			/ 0.0077		/ 0.0015		
Dental 0.75	113.2200 /	114.0550	-0.8350	114.3750	0.3200	109.9500	-4.1050	-1.1550
H60s RPCL	0.0073			/ 0.0028		/ 0.0373		
Dental 0.75	113.0225 /	113.9550	-0.9325	113.6750	-0.2800	109.3500	-4.6050	-0.6525
H60s LPCL	0.0082			/ 0.0025		/ 0.0404		
Dental 0.75	26.6825 /	27.3575	-0.6750	26.6225 /	-0.7350	54.5550 /	27.1975	
H30s SH	0.0247			0.0269		**0.9942**		0.0600
Dental 0.75	14.8500 /	14.3425	0.5075	15.0425 /	0.7000	27.6775 /	13.3350	
H30s SW	0.0354			0.0488		**0.9298**		-0.1925
Dental 0.75	105.3825 /	107.9100	-2.5275	105.5250	-2.3850	109.0750	1.1650	
H30s BW	0.0234			/ 0.221		/ 0.0108		-0.1425
Dental 0.75	113.1325 /	114.0550	-0.9225	113.8250	-0.2300	108.0750	-5.9800	
H30s RPCL	0.0080			/ 0.0020		**/ 0.0524**		-0.6925
Dental 0.75	112.1575 /	113.9550	-1.7975	113.7000	-0.2550	109.0250	-4.9300	
H30s LPCL	0.0158			/ 0.0022		/ 0.0433		-1.5425
Dental 2.0	27.8025 /	27.3575	0.4450	27.4450 /	0.0875	44.0150 /	16.6575	0.3575
H60s SH	0.0163			0.0032		**0.6089**		
Dental 2.0	14.5100 /	14.3425	0.1675	14.7600 /	0.4175	25.8975 /	11.5550	-0.2500
H60s SW	0.0117			0.0291		**0.8056**		
Dental 2.0	106.4225 /	107.9100	-1.4875	106.0250	-1.8850	105.8250	-2.0850	0.3975
H60s BW	0.0138			/ 0.0175		/ 0.0193		
Dental 2.0	113.6625 /	114.0550	-0.3925	113.7500	-0.3050	111.2250	-2.8300	-0.0875
H60s RPCL	0.0034			/ 0.0027		/ 0.0248		
Dental 2.0	112.0875 /	113.9550	-1.8675	113.0750	-0.8800	110.4250	-3.5300	-0.9875
H60s LPCL	0.0164			/ 0.0077		/ 0.0310		
Dental 2.0	26.3375 /	27.3575	-1.0200	27.2975 /	-0.0600	42.7300 /	15.3725	-0.9600
H30s SH	0.0373			0.0022		**0.5619**		
Dental 2.0	14.5550 /	14.3425	0.2125	14.8275 /	0.4850	26.0450 /	11.7025	-0.2725
H30s SW	0.0148			0.0338		**0.8160**		

Dental 2.0	103.3925	107.9100	-4.5175	105.2750	-2.6350	110.0750	2.1650	1.8825
H30s BW	0.0419			/ 0.0244		/ 0.0201		
Dental 2.0	111.7775 /	114.0550	-2.2775	113.0750	-0.9800	109.9750	-4.0800	1.2975
H30s RPCL	0.0200			/ 0.0086		/ 0.0358		
Dental 2.0	111.4825 /	113.9550	-2.4725	113.3000	-0.6550	112.3000	-1.6550	1.8175
H30s LPCL	0.0217			/ 0.0057		/ 0.0145		

ARE values of linear measurements on 3D-printed medical models (MM) are presented in *Linear measure value on 3D-printed medical models (mm) / ARE value* column; linear measurements on dry mandible are presented in *Linear measure value on dry mandible* column; difference of measurements on 3D-printed MM and dry mandible are shown in *3D-printed medical model – Dry mandible* column. 2D measurements on MSCT and CBCT are shown in *CT, CBCT 2D measure* column; difference of 2D measurements on MSCT/CBCT and dry mandible measurements are shown in *CT, CBCT 2D – Dry mandible* column. 3D measurements on MSCT and CBCT are shown in *MDCT, CBCT 3D measures* column; difference of 3D measures on MSCT/CBCT and dry mandible measurements are shown in *CT, CBCT 3D – Dry mandible* column. Discrepancy of the difference shown in *3D-printed medical model – Dry mandible* column and the difference shown in *CT, CBCT 2D – Dry mandible* column is shown in (*3D-printed medical model – Dry mandible*) – (*CT, CBCT 2D – Dry mandible*) column. Next to every measure taken from 3D model, CT and CBCT data, ARE value is given. Marginal ARE values are underlined, while bold numbers represent measures of ARE that are considered out of acceptable accuracy (Whyms et al. 2013).

To visualize the precision of each radiological protocol–derived MM measures compared with the mandible measures, we made rankings presented in Table 5. Based on similarity to the measures taken on the mandible, we made ranking separately for every measure taken and for every set of five measures for every MM, from 1 (the closest) to 8 (the farthest). As explained in the legend of Table 5, the *Sum of difference* rows of the *Measurement score* column show the ranking of every radiological protocol. However, when compared in this way, the standard-resolution CBCT (CBCT0.35) and Dental 2.0 H60s radiological protocols, with the summed score for all 5 measurements being 16, were both ranked on the second place. That made us believe that we need to compare the models more precisely, and we calculated the *Sum of difference*, marked with the underline in the *Difference* column, to sum up the total discrepancy for all 5 measures of each MM relative to the mandible. The ranking of this category is shown in the *Sum of difference rank* column. In this way, not only were we able to identify the more precise protocol among CBCT0.35 and Dental 2.0 H60s, which ranked the second, but we also found that Inner Ear UHR06 U90u went from the third position on the overall ranking on *Measurement rank* column to the fifth position in the *Sum of difference rank* column. The same applies to Dental 0.75 H30s, which shifted from the fifth to the seventh position in the same column.

Table 5: Linear measure rankings

Radiological protocol	Difference: linear measurements on MM – linear measurements on the dry mandible (mm)	Measurement score	Measurement rank	Sum of difference rank
CBCT0.25	SH -0.1000 SW 0.5200 BW -0.7700 RPCL 0.4500 LPCL -0.5600	SH 1 SW 6 BW 1 RPCL 2 LPCL 2	1	
Sum of difference	2.400	12		1
CBCT0.35	SH 0.3100 SW 0.6900 BW -0.7800 RPCL -0.6100 LPCL -0.4800	SH 2 SW 8 BW 2 RPCL 3 LPCL 1	2	
Sum of difference	2.8700	16		2
InnerEarUHR 0.6U90u	SH -0.7300 SW 0.3900 BW -0.800 RPCL -1.3100 LPCL -1.4800	SH 5 SW 3 BW 3 RPCL 7 LPCL 4	3	
Sum of difference	4.7000	22		5
InnerEarUHR 0.6U30u	SH -0.8000 SW 0.4600 BW -2.1200 RPCL -0.9900 LPCL -1.9000	SH 6 SW 4 BW 6 RPCL 6 LPCL 7	6	
Sum of difference	6.2700	29		6
Dental 0.75 H60s	SH -0.8600 SW 0.5900 BW -1.2800 RPCL -0.8400 LPCL 0.9300	SH 7 SW 7 BW 4 RPCL 4 LPCL 3	4	
Sum of difference	4.5000	25		4
Dental 0.75 H30s	SH -0.6800 SW 0.5100 BW -2.5300 RPCL -0.9200 LPCL -1.8000	SH 4 SW 5 BW 7 RPCL 5 LPCL 5	5	
Sum of difference	6.4400	26		7
Dental 2.0 H60s	SH 0.4400 SW 0.1700 BW -1.4900 RPCL -0.4017 LPCL -1.8700	SH 3 SW 1 BW 5 RPCL 1 LPCL 6	2	
Sum of difference	4.3717	16		3
Dental 2.0 H30s	SH -1.0200 SW 0.2100 BW -4.5200 RPCL -2.2800 LPCL -2.4700	SH 8 SW 2 BW 8 RPCL 8 LPCL 8	7	
Sum of difference	10.5000	34		8

The differences in linear measurements obtained on mandible and 3D-printed medical models (MM) is visible in *difference: linear measurements on mm – linear measurements on the dry mandible* column. *Sum of difference* rows of *difference: linear measurements on MM – linear measurements on the dry mandible* column, are calculated by adding up difference value of one MM set of measurements regardless of positive or negative sign. *Measurement score* column presents overall ranking score of every measure from *1* as the smallest and the most precise number to *8* as the least precise one. Sum of these rankings for every MM is given in the same column in the *Sum of difference* rows. *Measurement rank* column presents the overall ranking of MM by the sum of measure score, starting from the smallest and the most precise number marked by *1* to the largest and the least precise one marked with *7*. *Sum of difference rank* column presents the rank of every MM by the *Sum of difference* rows score of all five measurements, starting from the smallest, and there for most precise one, marked with *1*, to the largest and least precise, marked with *8*.

To emphasize the importance of attention on small measurements and illustrate the amount of deviation during repeating radiological measurements on CT and CBCT scans as well as its impact on measurement accuracy, we divided the average measurements with their

standard deviations. The results were as follows: SH: 35.891, SW: 79.375, BW: 93.835, RPCL: 199.475, LPCL: 213.483. Larger numbers depict the measures repeated with higher accuracy, and we generally observed larger numbers in the longer measures: RPCL, LPCL and BW. Although with the lowest standard deviation of 0.2 mm, SW as the shortest measure had the second lowest score.

We also determined and compared the average discrepancy of all MDCT and CBCT measurements from the measurements on the mandible, from the column *CT, CBCT 2D – Mandible* of Table 4, and the average discrepancy of only SW measure from the same table, and found that these values were 0.4652 and 0.5778, respectively. The two average discrepancies were similar and close to 0.5 mm, and the one related to SW was slightly larger.

As described in the Methods/Linear and volumetric measurements section, SH, SW and BW measures are aligned with the corresponding 3D axis of Cartesian coordinate system. Based on that, we can recommend the corrections, shown in Table 6, for every 3D model axis, after transformation of DICOM volume reconstruction into 3D model, to fabricate MM of accurate dimensions.

The physical measure of volume on MM compared with the mandible, shown in Table 7, demonstrated that the best results are obtained with CBCT0.25 and InnerEarUHR1 0.6 U30u protocols (Table 7, *Medical Model – Mandible* column). The attempt of volume measure correction by cumulative adding of 3D axis correction percentage (Table 7, *Axis correction of physical measure – dry mandible* column) showed negative effect on isotropic volume reconstruction protocols (CBCT0.25 and CBCT0.35), but improved volume measure accuracy of anisotropic volume reconstruction protocols in 4 out of 6 cases.

Table 6: 3D axis corrections

Radiological protocol	SD 3D-printed medical model	3D printed medical model-dry mandible	2D measurement / 3D axis correction / correction %
CBCT0.25	SH 0.0216 SW 0.0311 BW 0.0545 RPCL 0.1698 LPCL 0.4502	SH -0.0975 SW 0.5225 BW -0.7650 RPCL 0.4475 LPCL -0.5575	SH / Z 0.0316 / +0.1160% SW / Y -0.5536 / -3.7317% **-4.2237%** BW / X 0.8195 / +0.7649% RPCL / XYZ -0.6173 LPCL / XYZ 1
CBCT0.35	SH 0.0236 SW 0.0590 BW 0.0450 RPCL 0.2222 LPCL 0.1372	SH 0.3100 SW 0.6850 BW -0.7825 RPCL -0.6125 LPCL -0.4775	SH / Z -0.3336 / -1.2057% SW / Y -0.7441 / -4.9516% **-2.5976%** BW / X 0.8275 / +0.7724% RPCL / XYZ 0.8347 LPCL / XYZ 0.6147
InnerEarUHR 0.6U90u	SH 0.1028 SW 0.0058 BW 0.0699 RPCL 0.2871 LPCL 0.1780	SH -0.7325 SW 0.3925 BW -0.8025 RPCL -1.3125 LPCL -1.4825	SH / Z 0.8353 / +3.1373% SW / Y -0.3983 / -2.7030% **-1.7637%** BW / X 0.8724 / +0.8145% RPCL / XYZ 1.5996 LPCL / XYZ 1.6605
InnerEarUHR 0.6U30u	SH 0.1731 SW 0.0827 BW 0.0499 RPCL 0.0974 LPCL 0.3850	SH -0.8025 SW 0.4625 BW -2.1225 RPCL -0.9925 LPCL -1.8975	SH / Z 0.9756 / +3.6739% SW / Y -0.5452 / -3.6825% **-2.5645%** BW / X 2.1724 / +2.0536% RPCL / XYZ 1.0899 LPCL / XYZ 2.2826
Dental 0.75 H60s	SH 0.0648 SW 0.0208 BW 0.0818 RPCL 0.1855 LPCL 0.1424	SH -0.8575 SW 0.5925 BW -1.2825 RPCL -0.8350 LPCL -0.9325	SH / Z 0.9223 / +3.4804% SW / Y -0.6133 / -4.1065% **-2.4319%** BW / X 1.3643 / +1.2795% RPCL / XYZ 1.0204 LPCL / XYZ 1.0749
Dental 0.75 H30s	SH 0.0236 SW 0.0638 BW 0.0359 RPCL 0.1640 LPCL 0.3023	SH -0.6750 SW 0.5075 BW -2.5275 RPCL -0.9225 LPCL -1.7975	SH / Z 0.6986 / +2.6182% SW / Y -0.5713 / -3.8471% **-2.0989%** BW / X 2.5634 / +2.4325% RPCL / XYZ 1.0865 LPCL / XYZ 2.0998
Dental 2.0 H60s	SH 0.0330 SW 0.0455 BW 0.0695 RPCL 0.1441 LPCL 0.3165	SH 0.4450 SW 0.1675 BW -1.4875 RPCL -0.3925 LPCL -1.8675	SH / Z -0.4780 / -1.7193% SW / Y -0.2130 / -1.4680% **-0.0522%** BW / X 1.5570 / +1.4630% RPCL / XYZ 0.5365 LPCL / XYZ 2.1840
Dental 2.0 H30s	SH 0.0499 SW 0.0129 BW 0.0789 RPCL 0.3137 LPCL 0.3596	SH -1.02 SW 0.2125 BW -4.5175 RPCL -2.2775 LPCL -2.4725	SH / Z 1.0700 / +4.0626% SW / Y -0.2254 / -1.5486% **-0.3990%** BW / X 4.5964 / +4.4456% RPCL / XYZ 2.5912 LPCL / XYZ 2.8320

Standard deviation of measures observed on 3D-printed medical models derived from every radiological protocol are shown in *SD 3D-printed medical model* column, and difference from the same measure on dry mandible in *3D-printed medical model- mandible* column. Corresponding axis of the 3D model, maximum error per 3D axis and in the same time a proposed correction is indicated *in 2D measurement / 3D axis correction / correction %* column. Value of Y axis correction percentage, recalculated under 15X magnification is given in bolded letters.

Table 7: Volume measures and comparison

Radiological protocol	Volume reconstruction / ARE value		Physical measure / ARE value					
	Tissue (cm^3)	SD (cm^3)	Average (cm^3)	SD (cm^3)	3D printed medical model – Dry mandible (cm^3)	Axis correction of physical measure (cm^3) / ARE value	Axis correction of physical measure – Dry mandible (cm^3)	Materialize mimics volume measure (cm^3) / ARE value
CBCT 0.25	53.7500 / 0.0194	0.7300	53.6075 / 0.0220	2.2026	-1.2075	52.1380 / 0.0488	-2.6770	52.3048 / 0.0458
CBCT 0.35	57.7900 / **0.0543**	0.9500	52.7750 / 0.0372	0.8839	-2.0400	50.2930 / **0.0825**	-4.5220	52.6337 / 0.0398
InnerEarUHR 1 0.6 U90u	58.7700 / **0.0722**	1.0000	52.790 / 0.0370	0.3677	-2.0250	54.4460 / 0.0067	-0.3690	52.8911 / 0.0351
InnerEarUHR 1 0.6 U30u	57.0100 / 0.0400	0.9800	53.5950 / 0.0223	0.2758	-1.2200	54.6253 / 0.0035	-0.1897	58.1894 / **0.0616**
Dental 0.75 H60s	56.1600 / 0.0245	1.0000	51.4150 / **0.0620**	1.1102	-3.4000	51.6760 / **0.0573**	-3.1390	53.5105 / 0.0238
Dental 0.75 H30s	53.9500 / 0.0158	0.9000	57.1550 / 0.0427	0.0778	2.3400	57.9810 / **0.0578**	3.1660	57.8436 / **0.0552**
Dental 2.0 H60s	72.7700 / 0.3276	1.9700	52.0950 / 0.0496	0.9970	-2.7200	51.4550 / **0.0613**	-3.3600	54.4654 / 0.0064
Dental 2.0 H30s	71.9600 / 0.3128	1.9200	52.2450 / 0.0469	0.5020	-2.5700	55.9014 / 0.0198	1.0864	58.5065 / **0.0673**
MANDIBLE			54.8150	0.5445				

Digital volume reconstruction of Digital Imaging and Communication in Medicine (DICOM) data is given in the *Volume reconstruction / ARE value* column, and the medical model and the dry mandible physical volume measures by water immersion in volume measuring vessel (VMV) are shown in the *Physical measure / ARE value* column. Differences between 3D-printed medical model and dry mandible physical volume measures are shown in the *3D printed medical model – Dry mandible* column. The effect of the proposed axis corrections on the physical volume measure is shown in the *Axis correction of physical measure / ARE value* column; the effect of axis correction on the difference in the physical volume measures between medical models and dry mandible is shown in the *Axis correction of physical measure – Dry mandible* column; and the volume measure of the corresponding 3D model in Materialize Mimics software is shown in the *Materialize mimics volume measure / ARE value* column. Values of average relative error (ARE) are given after "/" sign. Values of ARE that are considered out of acceptable are marked in bold, while marginal ARE values are underlined.

4.3 Intra- and inter-observer tests

ICC values showed high intra- and inter-observer agreement in linear measurements of the 3D medical models, MSCT-CBCT 2D, MSCT-CBCT 3D, and mandible, all in the range from 0.959 to 1. Inter-observer ICC score for the volume measurements was 0.929.

4.4 Microstructural assessment and wettability determination of 3D-printed bone construct

3D-printed bone scaffold micro-porosity assessment revealed the following: total porosity of 64%, closed porosity of 0.54%, open porosity of 63.46%, average trabecular-like structures thickness of 177 μm, average pore size of 256 μm and number of closed pores per mm^3 of 34,8.

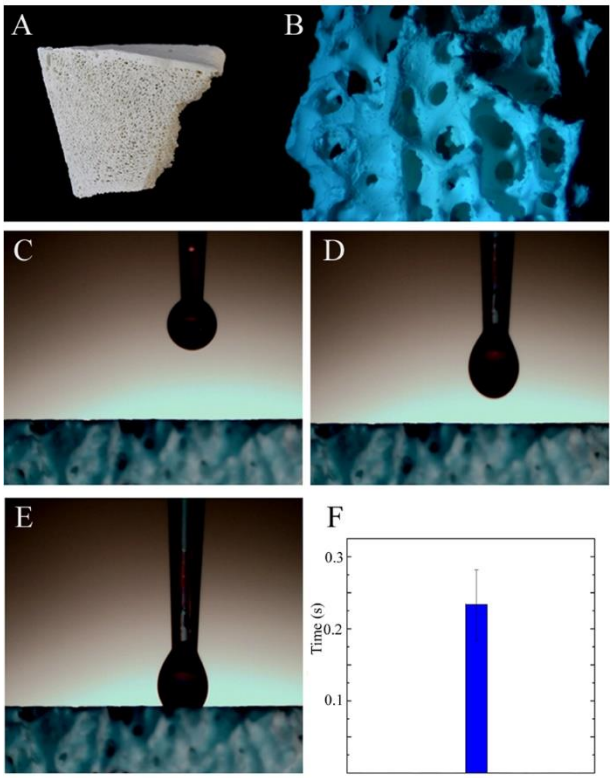

Figure 17: A) The engineered construct used for the experiments and B) its structure after magnification (X200). C-E) Wettability of the construct. Administration of the reference liquid droplet on the construct surface. F) Histogram showing the time required for reference liquid to completely wet the construct surface. Note that the droplet is absorbed within the part of the second.

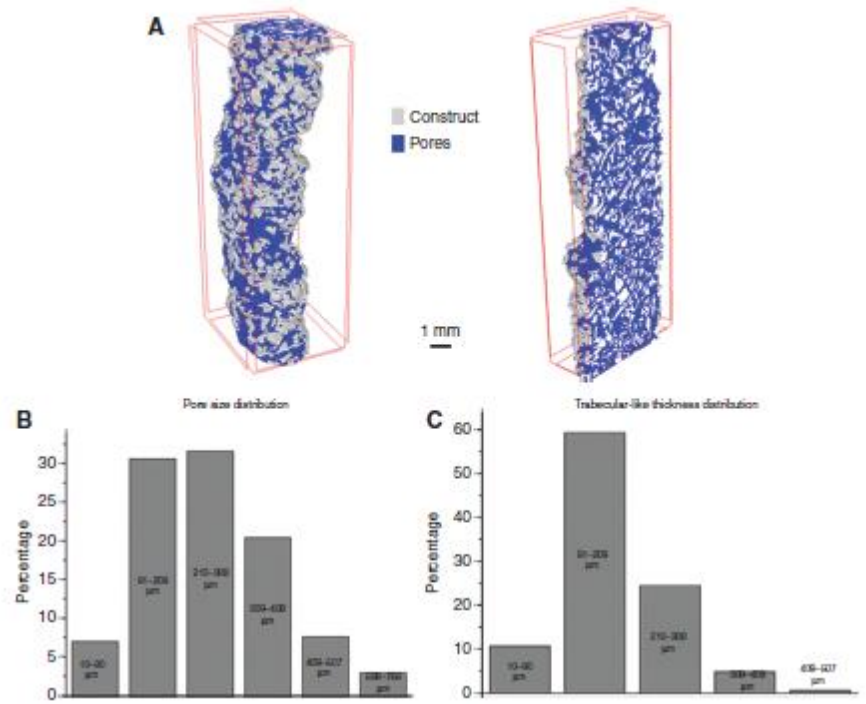

Figure 18: Micro-architectural properties of the 3D-printed bone replacement scaffold as measured by micro-computed tomography. The total porosity of 64% provided promising conditions for new bone conductivity. (A) Three-dimensional reconstruction of the construct's micro-CT image. (B) The construct's pore size distribution. (C) The construct's trabeculae-like bars' thickness distribution.

4.5 Cytocompatibility assays

The assessment of mitochondrial activity demonstrated a strong connection between the construct and SCAP, as indicated by the high uptake of tetrazolium salts in both the experimental and control groups of cells (Figure 19 A, B). Figure 19 C presents the absorbance values obtained from the measurements taken in the wells where the construct directly contacted SCAP and the control wells. No statistically significant differences were observed between the groups.

In the *in vitro* scratch assay, cell migration during the 24-h exposure to the serial dilutions of the investigated material extracts was found to be concentration-dependent. Higher concentrations of GM and OM significantly stimulated cell migration. Statistical significance was observed for the 1:1 ($p<0.05$), 1:2 ($p<0.0001$) and 1:4 ($p<0.0001$) dilutions, while no statistical significance was found for the 1:8 and 1:16 dilutions compared with the control group in 2% FBS medium (Figure 19 D).

The ALP activity assay revealed a significantly higher values of ALP activity in groups of cells seeded on scaffolds (Figure 19 E).

The mineralization assay test showed significant difference in the extracellular deposition of mineralized globules between two groups of cells cultured in OM and GM and cells seeded on the construct and cultured in either GM or OM ($p<0.05$) (Figure 19 F).

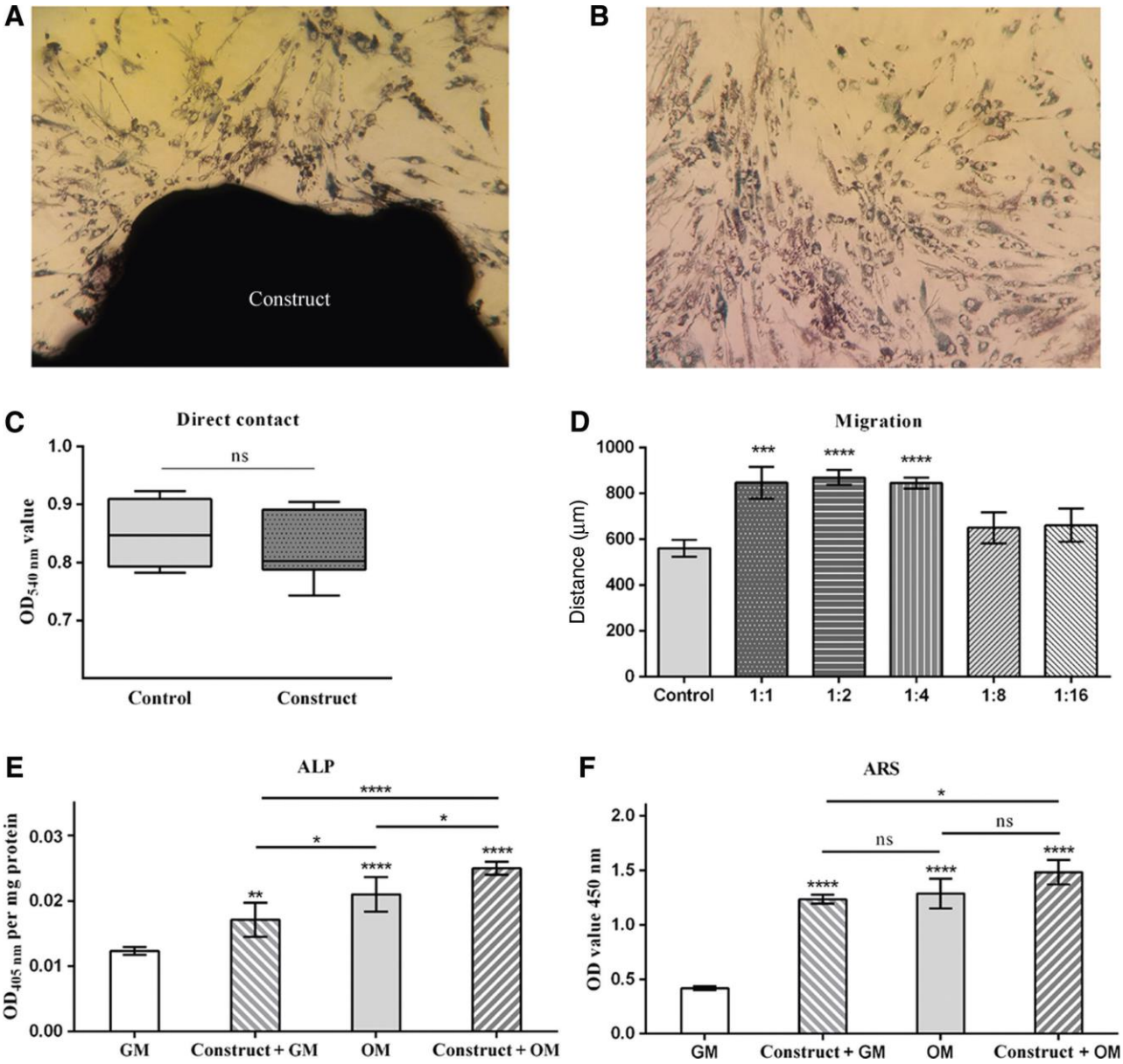

Figure 19: Cytocompatibility evaluation of the construct extracts. A: Image of the intimate contact of stem cells of the apical papilla (SCAP) and the bone construct 72 h after cell seeding. There is visible high level of formazan salt uptake in SCAP in contact with the scaffold. B: Image of control cells under phase-contrast microscopy, 100 ×. C: Absorbance measures from the control wells and the wells from the direct contact of the scaffold and cells. D: Scratch assay results of SCAP exposed to serial dilutions of material extracts. Results are presented as cells' migration distance at 24 h interval. Statistical significance is marked with asterisks (***$p < 0.05$, ****$p < 0.0001$). E: Alkaline phosphatase enzyme extracted on day 7 from SCAP cultured in growth medium (GM), osteogenic medium (OM), on construct in GM and on construct in OM (*$p < 0.05$, **$p < 0.01$, ****$p < 0.0001$, one-way ANOVA). F: Quantification of Alizarin red S bound to cultures extracted on day 21 from SCAP cultured in GM, SCAP in OM, on construct in GM and on construct in OM (*$p < 0.05$, ****$p < 0.0001$).

SEM images of the osteoblasts seeded on scaffolds for 7, 14 and 21 days (cultured in growth and osteogenic medium) are presented in Figure 20. The cellular morphology underwent changes over time, transitioning from a fibroblast-like appearance, which is characteristic of mesenchymal stem cells and predominates on the 7th day of culturing in growth

medium, to flattened bone-lining cells with numerous cytoplasmic processes and intercellular connections, a morphology specific to osteoblasts on the 21st day of culturing in growth medium. The stem cells transitioned into osteoblast-like cells by the 7th day of culturing in the osteogenic medium.

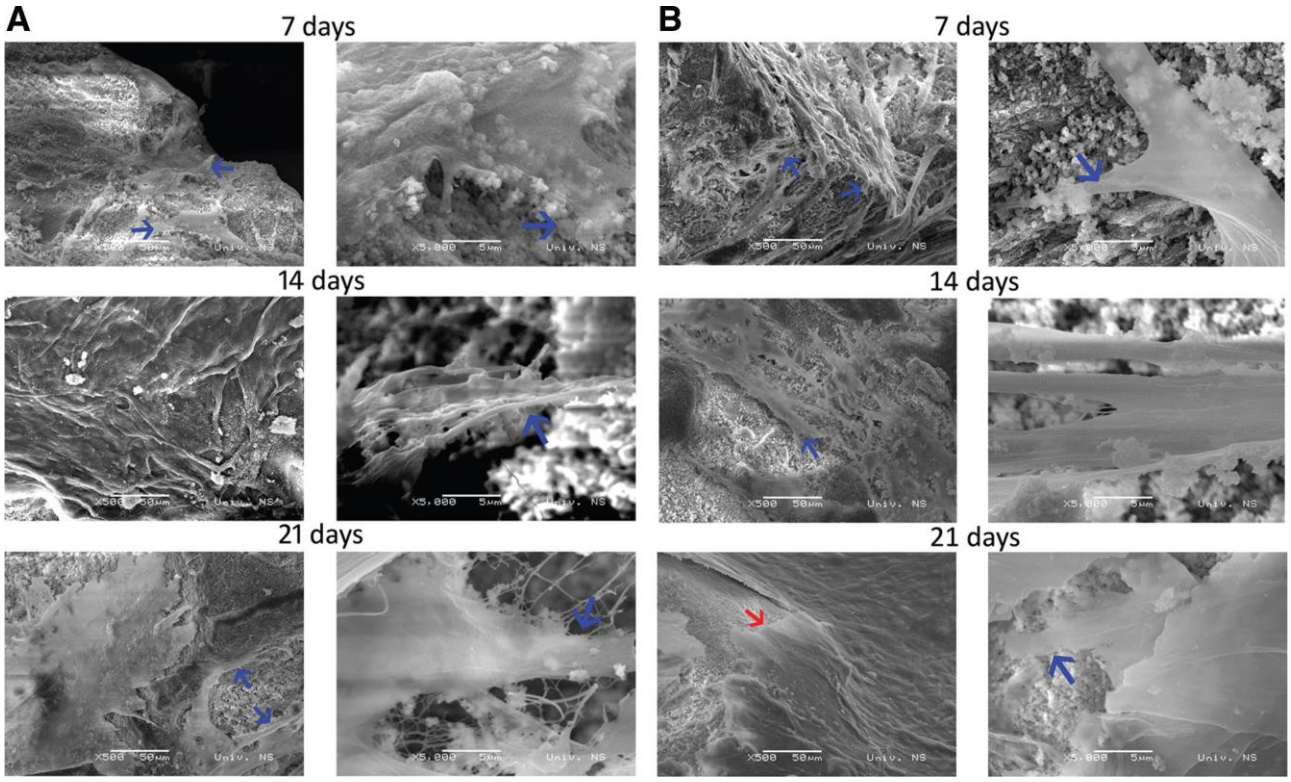

Figure 20: Scanning electron micro-photographs of osteoblasts seeded on the construct's surface, cultivated in two different media. A: Scanning electron micro-photographs of the osteoblasts cultivated in growth medium and seeded on the construct's surface for 7, 14 and 21 days. Blue arrows refer to the cells with morphological changes to stabilize the cell-material interface. B: Scanning electron microphotographs of the osteoblasts cultivated in osteogenic medium and seeded on the construct's surface for 7, 14 and 21 days. Blue arrows point to the cytoplasmic extensions that indicate cell adhesion. Note that after 21 days of seeding the lamellar structure of the osteoblasts was formed on the surface of the manufactured construct (red arrow).

4.6 Radiography of the implanted bone construct and micro-CT analysis of the explanted tissue

Figure 21 illustrates the progression of bone healing over time. Radiographic evaluation of the rabbit's ulna at 6 weeks post-implantation of the bone construct revealed extensive formation of calcified endosteal callus, visible as shadows at the fracture site and well-formed

deposits penetrating the bone. By 9 weeks post-implantation, clear indications of bone deposition were observed on both the proximal and distal parts of the ulna. The reconstructed bone 3D images, along with the adjacent remaining material particles, are depicted in Figure 22B and Figure 22F.

Figure 21: Representative radiographic images of rabbit ulna defects reconstructed using the engineered 3D construct at 3-, 6-, and 9-weeks post-surgery. Three weeks after the surgery, the fracture lines were clearly visible, while the construct remained in place without any dislocation. At six weeks post-surgery, the fracture lines were barely discernible and exhibited continuous illumination. The construct's shadow exhibited calcium deposits, a granular structure, and direct contact with the surrounding bone. No signs of fragment dislocation were observed. After nine weeks, the fracture lines became indistinct due to mineral deposition and the formation of new bone tissue, which penetrated the construct sharply from both the distal and proximal sides. The construct's shadow appeared smaller compared with the earlier radiographic phase and was partially replaced by newly formed bone. The spongiosa on the ulna exhibited consolidation at the site of discontinuity, accompanied by a thickening of the cortical bone. Mineralization of the spongiosa was also present in the mid-diaphysis of the radius.

Cross-sectional micro-CT images of the original bone and newly formed bone are presented in Figures 22A and 22C, respectively. Statistical analyses demonstrated a significant difference between the original and newly formed bone in terms of total porosity and open porosity parameters ($p<0.05$). However, no significant differences were observed for closed porosity, average pore size and average cortical thickness between the old and new bone areas ($p>0.05$) (Figure 22D). The pores were categorized into three groups: 0–50 µm, 50–210 µm, and 210–470 µm. The highest percentage of pores was in the 50–210 µm range, in both the new bone group (47±15%) and the old bone group (47±12%). There was no significant difference between the new and old bones for any of the pore size categories tested ($p>0.05$) (Figure 22E).

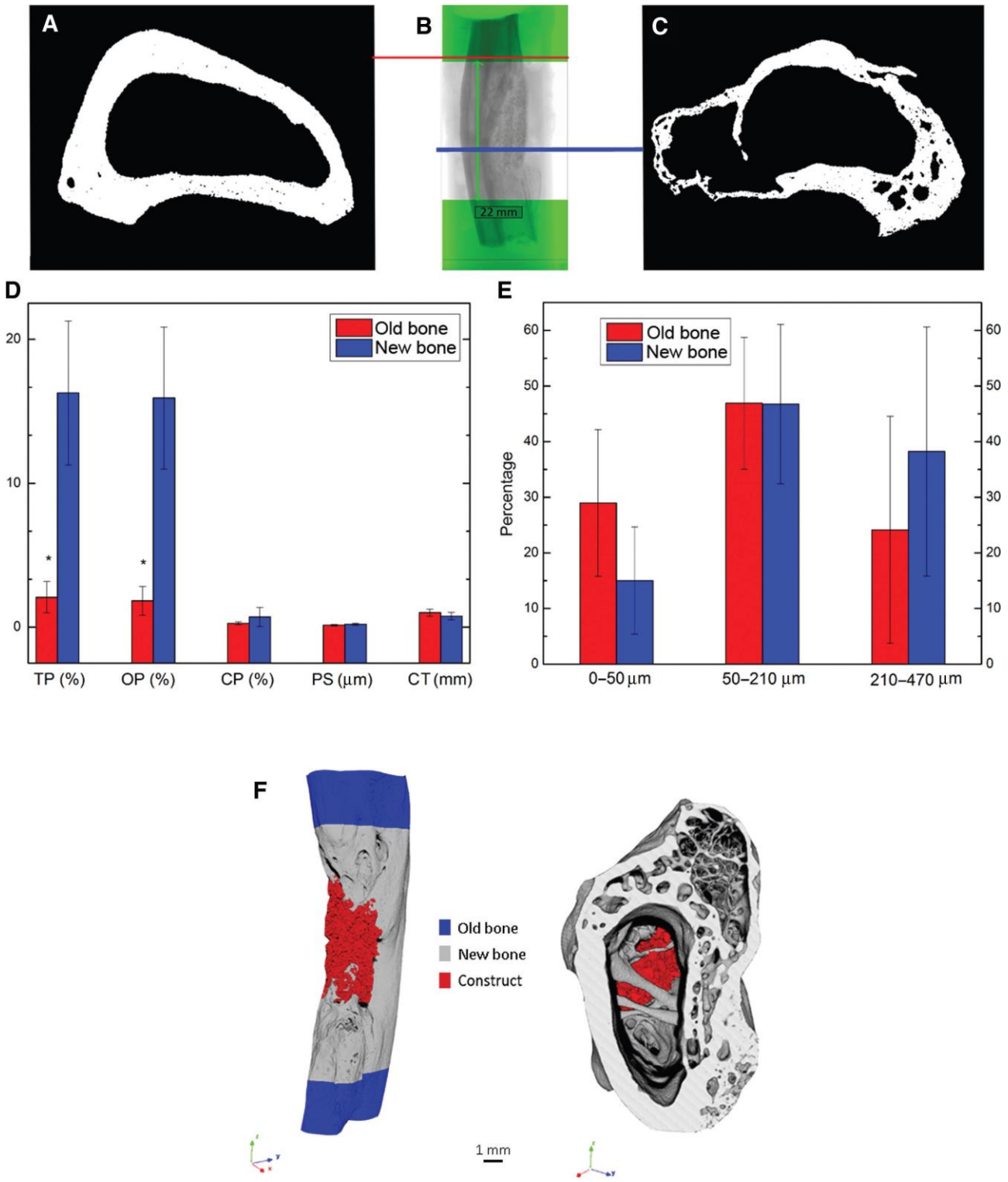

Figure 22: A and C: The assessment of orthotopic bone formation. Micro-CT cross-sections of the old bone (A) and new bone (C) were captured at 12 weeks post-surgery. B: The segmental bone defect measured 22 mm in size. D: Quantitative histograms illustrate the formation of new bone at 12 weeks, depicting TP (total porosity), OP (open porosity), CP (closed porosity), PS (pore size), and CT (cortical thickness). E: The distribution of pore sizes in new and old bones is displayed. Statistical significance between the new and old bones is indicated by asterisks ($p < 0.05$). F: In areas where the new bone formed, it established complete integration with the old bone, benefitting from increased nutrient supply and the presence of bone cells. However, in the central region, remnants of the non-resorbed bone substitute can be observed. Notably, formation of trabeculae is evident within the bone structure.

4.7 Histological and histomorphometric analysis

The histological analysis of the explanted bone revealed satisfactory healing of the bone defect without complications such as necrosis, infection or bleeding. After 12 weeks of healing, the defect was filled with newly formed bone (NFB) and remaining scaffold particles. The NFB tissue exhibited close contact with the old bone, with a discreet demarcation line between them. In this region, as well as in the area of the NFB, small isolated scaffold particles were observed, surrounded by bone tissue without CNT interposed.

The histological analysis demonstrated that a small amount of NFB was mineralized, while the majority of it was non-mineralized, indicating active osteogenesis. Furthermore, a significant portion of the NFB exhibited signs of lamellar organization, with vital osteocytes concentrically positioned around Haversian channels. Woven non-mature bone was also present, indicating active remodeling of the bone tissue. The NFB primarily displayed a trabecular architecture with newly formed bone marrow among the trabeculae. Additionally, hyaline cartilage was identified, indicating the presence of ossification (Figures 23 and 24).

The results of histomorphometric analysis did not show significant differences between the central and peripheral parts of the defect, either for NFB (35±11% vs. 51±11%, respectively) or for the mineralized surface area - MSA (35±11% vs. 49±11%, respectively) ($p>0.05$). No connective tissue or construct particles were observed in the peripheral part of the defect. On the other hand, 6±5% of connective tissue and 17±17% of construct particles were found in the central part of the defect.

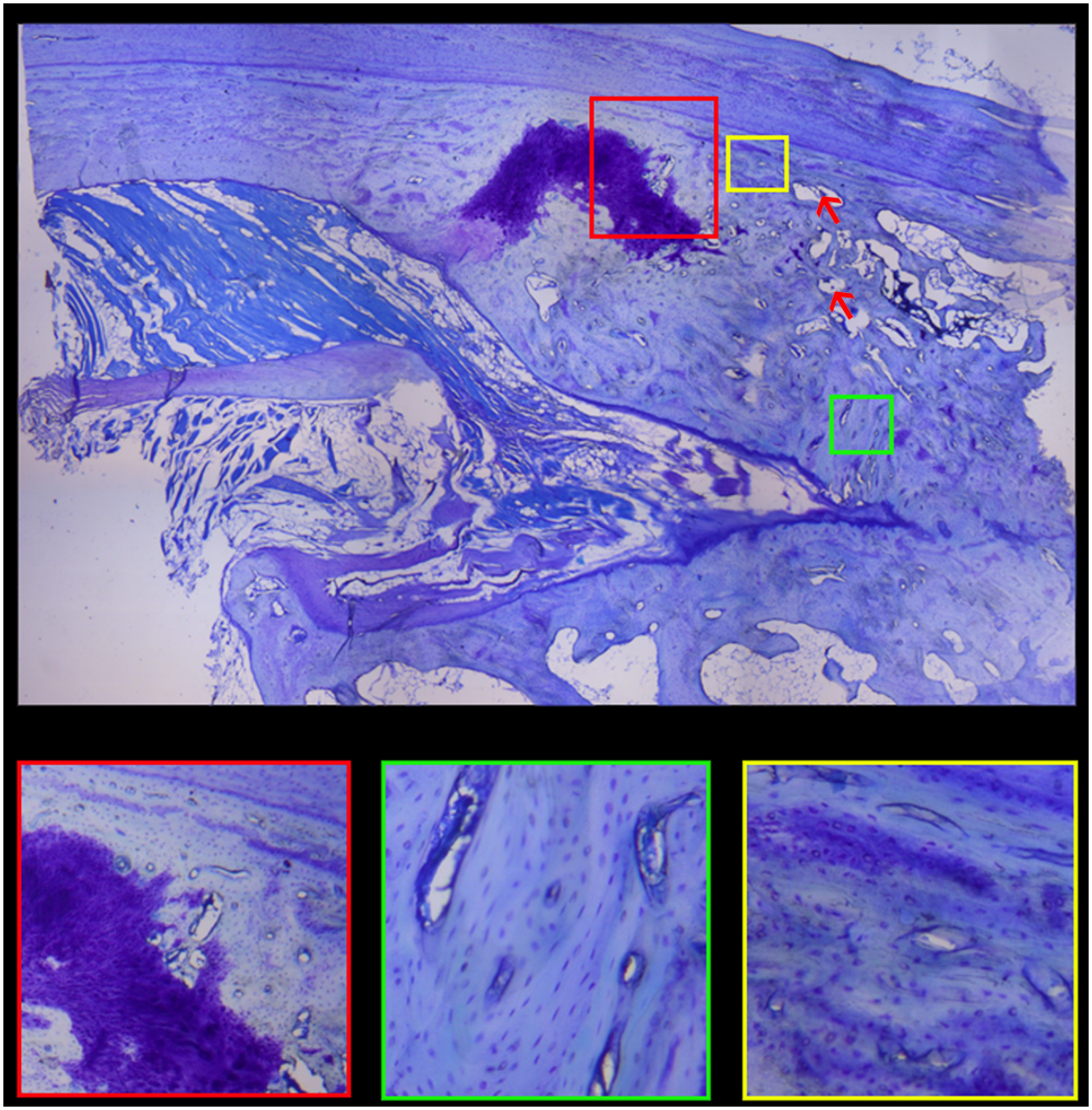

Figure 23: Toluidine blue staining of the harvested bone. Upper panel: A merged image of the defect, which is nearly completely filled with newly generated bone tissue. A distinct boundary line is observed, representing the separation between mature and immature new bone. Numerous graft particles are present (indicated by red arrows), surrounded by bone tissue, with no presence of soft tissue (10x magnification). Red square: Hyaline cartilage is prominent, suggesting the presence of ossification. Green square: Isolated material particles that are surrounded by newly formed bone tissue, predominantly exhibiting a lamellar structure (100x magnification). Yellow square: The morphological characteristics of numerous viable nuclei within osteocyte lacunae indicate bone repair. The construct particles are fully embedded in the newly formed bone, demonstrating the excellent osteoconductive properties of the material (100x magnification).

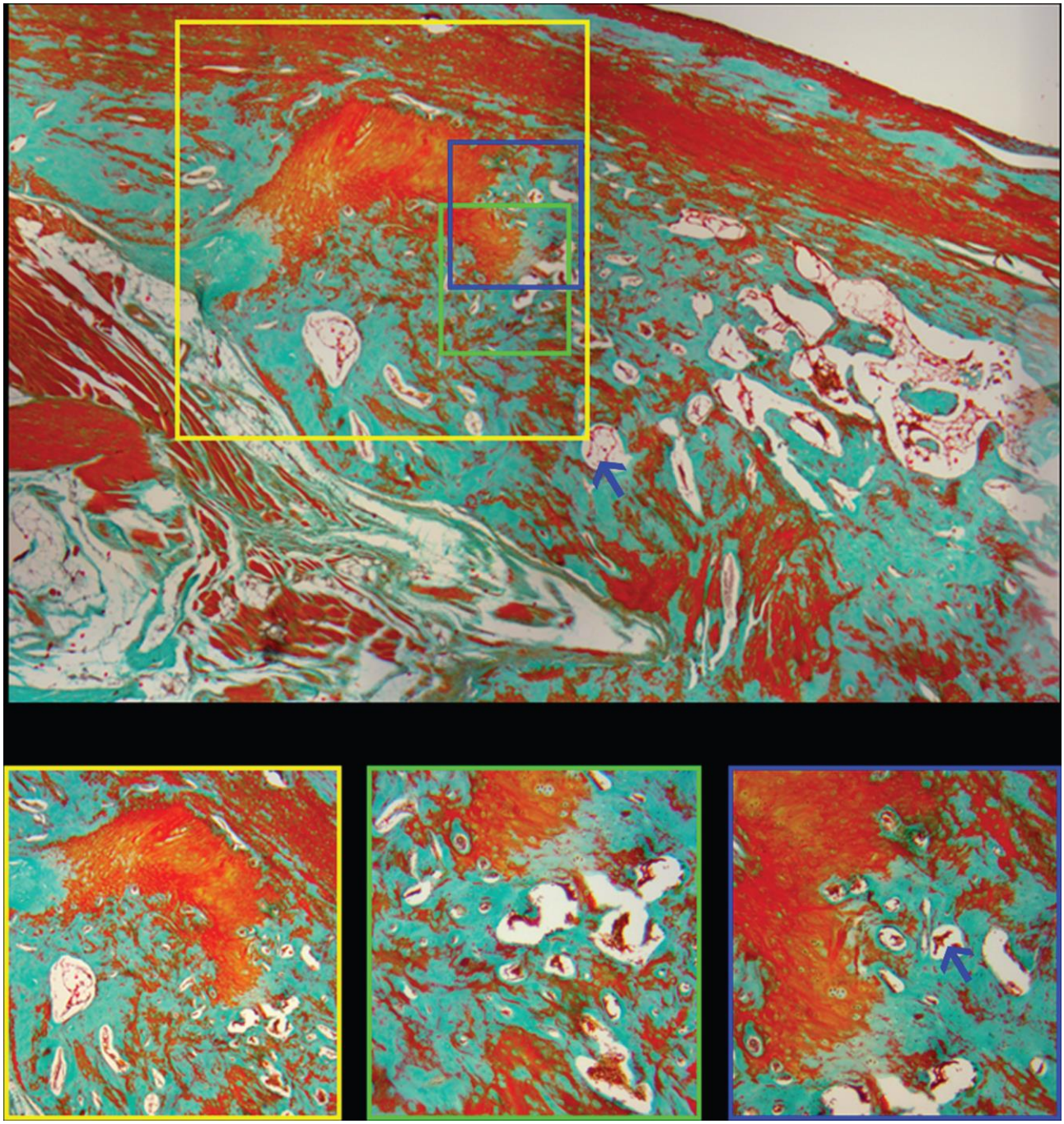

Figure 24: Goldner trichrome staining of the harvested bone. Upper panel: Stitched image. Green color indicates the mineralized bone, while red color indicates the non-mineralized tissue. Yellow square: Wide area of hyaline cartilage and predominately the presence of non-mineralized new bone tissue indicating active osteogenesis (40×). Green square: Ossification is observed. NFB is mainly not mature and non-mineralized (100×). Blue square: The construct particles (blue arrows) are predominantly embedded within the newly formed bone tissue without interposing the fibrous tissue between the construct and new bone (100×).

4.8 Immunostaining analysis

The quantities of bone tissue exhibiting positive staining for BMP2 were greater in comparison to the bone tissue displaying positive staining for OCN and OPN. Many cells with intense BMP2 staining were observed in the area of the construct, as well as in the adjacent sections of rabbit ulna (Figures 25 and 26). Only a small number of cells positive for OCN and OPN were identified, both within the construct region and in the surrounding bone tissue of the rabbit.

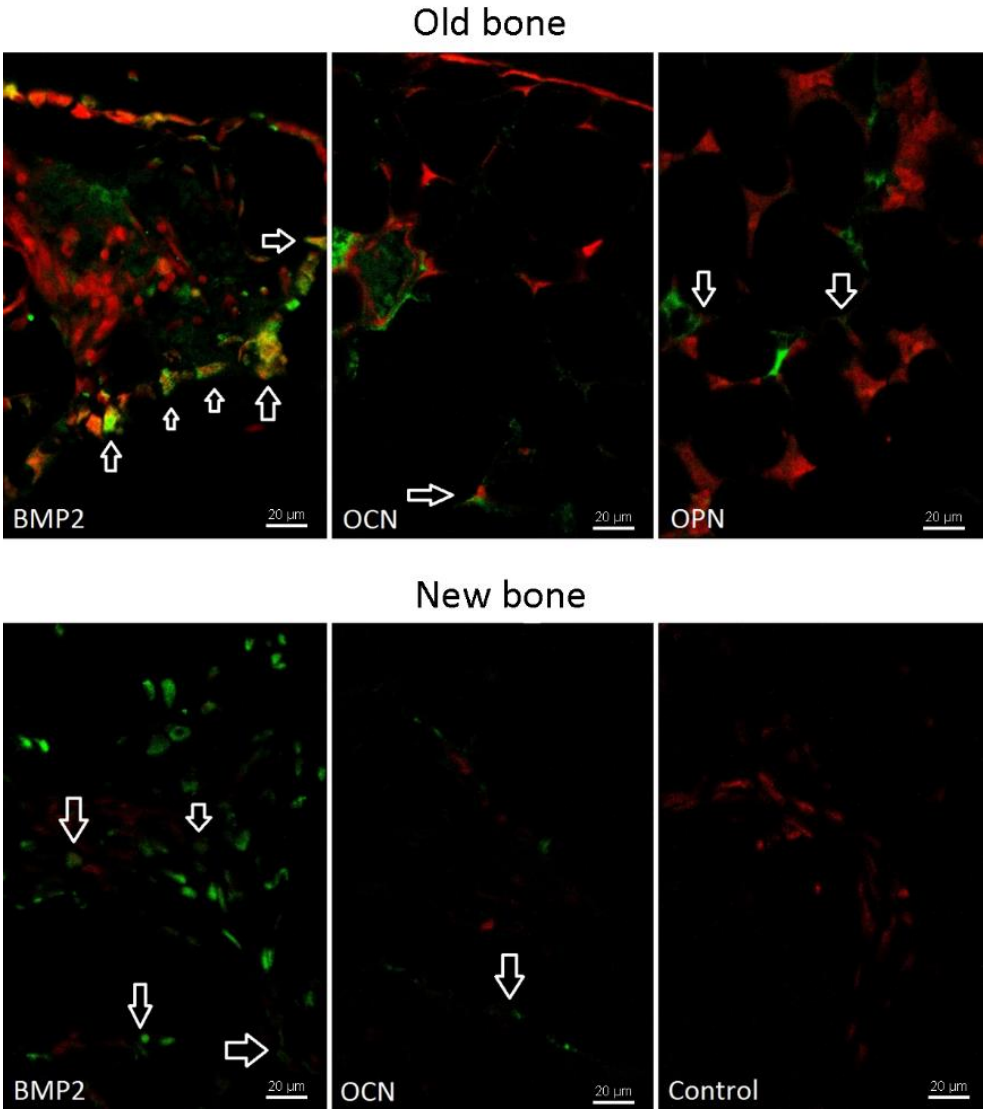

Figure 25: Confocal microscopy of bone remodeling indicators in different regions of the reconstructed bone. Immunofluorescence staining of anti-bone morphogenetic protein 2 (BMP2), anti-osteocalcin (OCN) and anti-osteopontin (OPN). Expression of BMP2 molecule, OCN molecule and OPN molecule in old bone and newly formed bone (white arrows) and the control staining for secondary antibody.

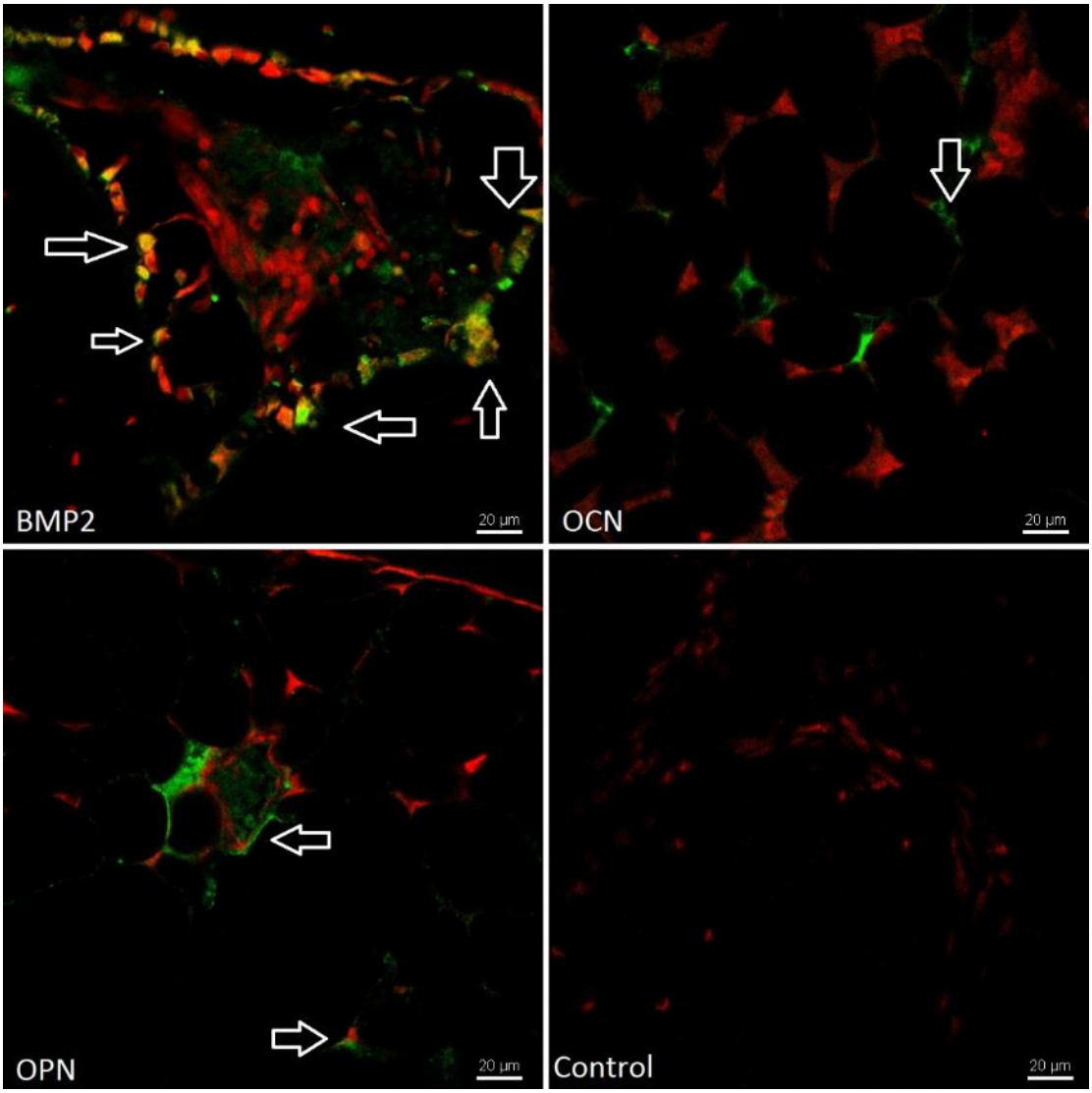

Figure 26: Immunofluorescence staining of anti-BMP2, anti-OCN and anti-OPN antibodies in the rabbit bone near the construct, and the expression of BMP2, OCN and OPN molecule (white arrows) and the control staining for secondary antibody.

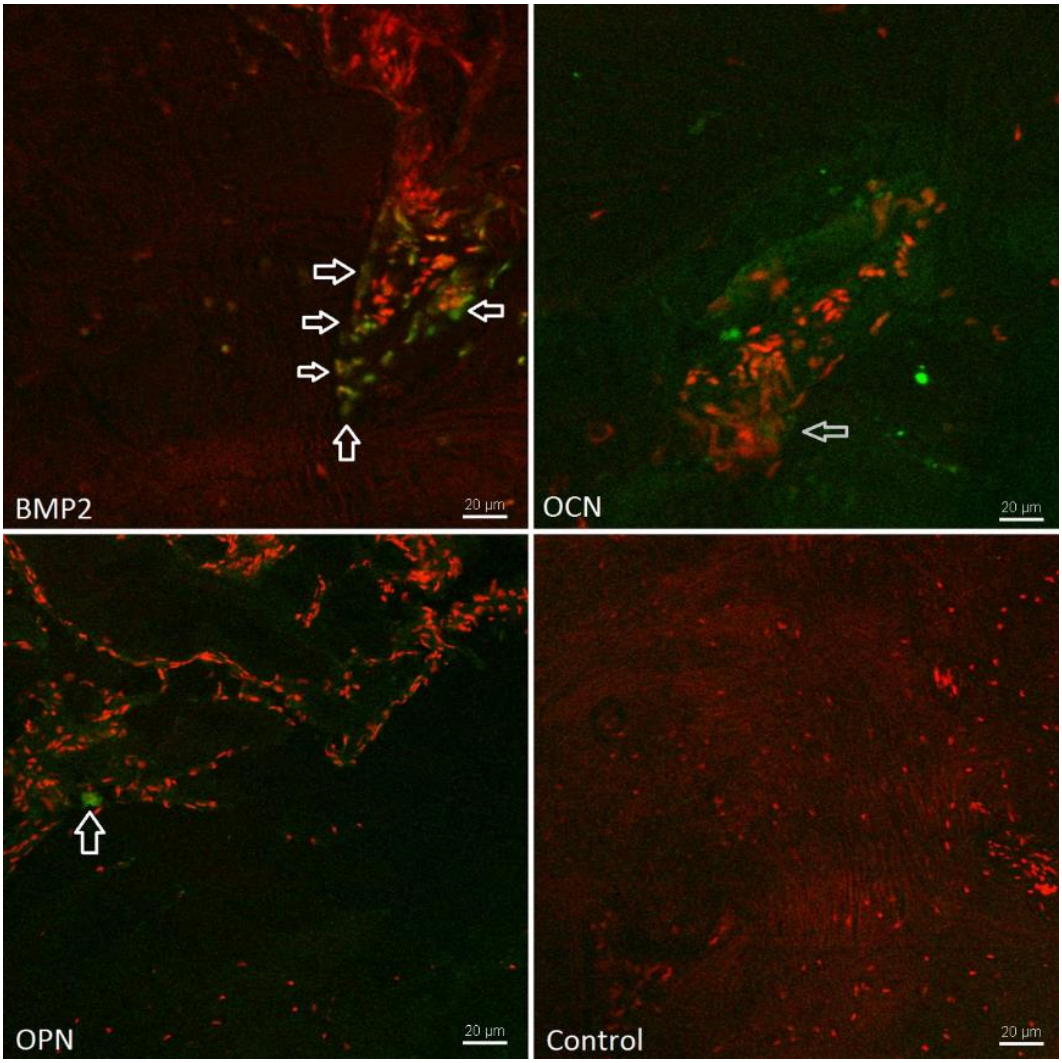

Figure 27: Immunofluorescence staining of anti-BMP2, anti-OCN and anti-OPN antibodies in the construct's region. Expression of BMP2, OCN and OPN molecule (white arrows) and the control staining for secondary antibody.

4.9 Evaluation of clinical implementation of virtual surgical planning, medical models and surgical guides

1. Surgery time or surgery duration: Average duration of 7 surgeries done with the help of virtual planning and 3D printing was 10.7 ± 1.1 hours, while that of five surgeries in the control group was 12.1± 2.8 hours. The difference between the experimental and the control group was 1.4 hours (t-test, p=0.131).
2. Average time of hospitalization was 8.57±1.62 days ([min-max]: 6-11) for the experimental group and 17.6 ±15.47 days([min-max]:8-45) for the control group. Mann–Whitney U test showed significant difference between the groups (p=0.0165).
3. Surgical complications were registered in only one case in the control group. Complications consisted of inadequate placement and orientation of the transplant, which later resulted in significant resorption of the transplant.
4. Final functional and esthetic result: Comparing the control and the experimental groups by t-test, we found that the mean percentage of autograft out of volume (planned position) was significantly better in the experimental group (21.586±9.448) than in the control group (59.64±19.81, p=0.001). The mean lateral displacement of the autograft was 3.351±0.797mm and 14.18 ± 8.333mm in the experimental and the control group, respectively (p=0.006). The mean AP displacement of the autograft was 5.643±2.31mm and 17.24±10.458mm in the experimental and the control group, respectively (p=0.031).
5. Patient satisfaction was most commonly reported as 5 ([min-max]: 4-5, median value:5) out of 5.00, in the experimental, while in the control groups it was frequently reported as 3 ([min-max]:3-5, median value:3), respectively. There was a significant difference between the groups (Mann–Whitney test, p=0.017).

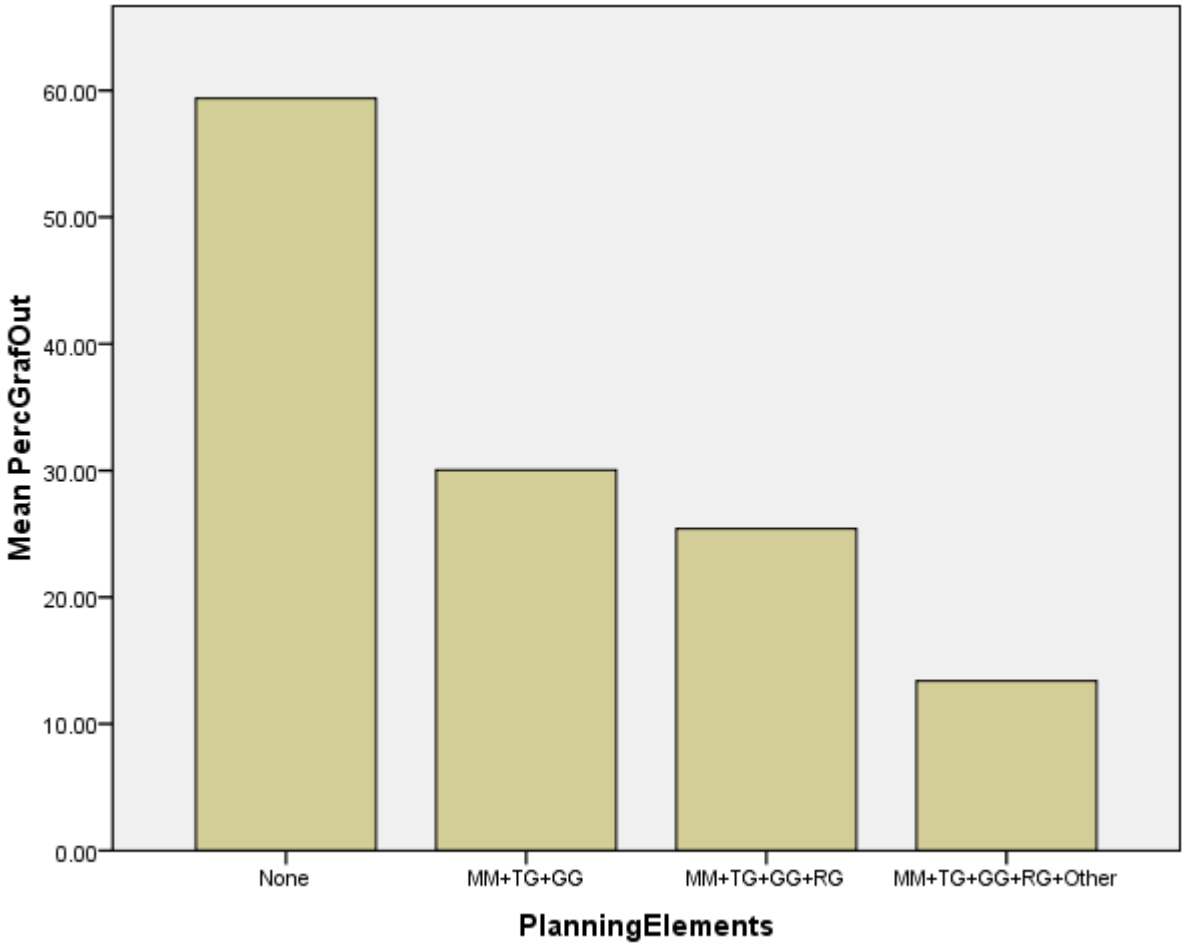

Figure 28: Graphical representation of relation of number of objects and techniques used during planned surgery (horizontal axis) to the percentage of bone graft placed postoperatively out of the volume of preoperative mandible margins. *None* column represents surgeries done conventionally. *MM+TG+GG* column represents surgeries done with help of MM, TG (transplant guide, the surgical guide for donor region resection) and GG (graft guide, the surgical guide for shaping of auto-transplantation graft). *MM+TG+GG+RG* column represents surgeries done with the use of MM, TG, GG and RG (resection guide, the surgical guide for resection of the mandible). *MM+TG+GG+RG+Other* column represents surgeries done with all the previous elements combined with resection MM (that is used to check the shape and fitting of the auto-transplantation graft) and fixators of the mandible after resection, that secure the spatial relation between resected mandible ends.

5. Discussion

In the first part of our study, we investigated some fundamental dilemmas in the field of medical 3D printing, that is, what technology and which scanning protocol should be chosen when trying to translate the virtual anatomical model into a 3D-printed model that accurately mimics the shape of the scanned anatomical structure (Micic et al. 2023). The obtained results are of paramount importance given that there are not enough data in the literature regarding the most suitable technology/protocol for producing high-accuracy 3D medical models. This is especially challenging considering the necessity of MSCT or combined CBCT and MSCT use for SG and MM in autograft mandibular reconstruction (Serrano et al. 2019). This is the very first study where detailed analysis of several radiological approaches was tested in the human mandible and, therefore, it is expected that the results may be highly usable in oral and maxillofacial surgical reconstructive procedures.

We found that application of different radiological protocols resulted in various metrical discrepancies between 3D-printed models and the mandible. We checked every step of the procedure as potential error source. We assessed the difference of linear measures that arose from DICOM to 3D model transformation and/or 3D model to 3D-printed MM procedure to test the used 3D printing methodology, and the difference was not significant. In the next step, significant variability of the linear measures, confirmed by one-sample t-test ($p<0.05$, Table 4), revealed that the radiological protocols were the source of discrepancies.

One-sample t-test of the differences in the set of linear measures of the mandible to every radiological protocol–based MM linear measures (Table 4) did not show statistically significant deviation from 0, but differences generated by some protocols were at the brink of significance, as follows: InnerEarUHR0.6 U30u: p=0.080, Dental 2.0 H30s: p=0.063: Dental 0.75 H60s: p=0.110, Dental 0.75 H30s: p=0.104. It should also be taken into account that, considering the precision required by the specific nature of MM and bone SG use, the statistical significance threshold in future research may be less than 5%, because millimeter-scale deviations produce miss-fitting between the bone and SG. Namely, our detailed analysis of *MM – Mandible* data revealed the differences over 2 mm related to Dental 2.0 H30s, Dental 0.75 H30s and InnerEarUHR 0.6U30u radiological protocols, and differences over 1 mm resulting from Dental 2.0 H60s, Dental 0.75 H60s and InnerEarUHR 0.6U90u protocols (Table 4). In our study, the protocols that were related to the differences below 1 mm were high- and standard-resolution CBCT protocols (Table 4). On the same subject, Amin and Saleh managed to compare direct physical measures with the volume reconstructions of CBCT and MSCT scans; they found no significant and clinically relevant differences, reporting submillimeter errors (Amin and Saleh 2015). However, it is possible that the result of <1 mm error is related to the design of Amin and Saleh`s study, where out of 26 measurements in total, 24 were under 33 mm and majority were under 20 mm. Taking into account the ARE values of the measurements of the study of Amin and Saleh, it is obvious that the measurements over 100 mm would give >1 mm or even >2 mm errors. Similar to our research, Whyms and coworkers attempted to determine MSCT parameters acceptable for quantitative 3D modeling for pre- and post-surgical planning as well as to increase accuracy of both prosthetic material construction and treatment change recognition (Whyms at al. 2013). Although these authors did not discuss surgical planning in detail, their study did give many guidelines for future research, some of which we have applied. In the study of Whyms and associates, ARE values were in acceptable range for all measurements, except for volumetric measurements on MSCT slice thickness of 2.5 mm. Linear measurements illustrated in the same study revealed discrepancies well over 2 mm on some of the measurements (Whyms at al. 2013). Hence, while the ARE values in the

cited scientific papers are considered acceptable and in the range of 5% statistical significance, it is obvious that fitting misalignments of few millimeters of SG and reconstruction grafts for bone tissue would lead to serious issues or failure of the whole surgical outcome. Similar to implant surgery guides and prosthetics in dentistry, bone surgery guides and grafts require reliable accuracy. The acceptable range of accuracy should be a matter of future detailed research for each particular skeletal site.

When analyzing each linear measure individually, our data revealed that BW showed the most significant discrepancy between the MSCT/CBCT scans and the mandible (Table 4), and between the 3D-printed MM and the mandible (Table 4), considering that it was underestimated in all 16 cases. This result is not expected because this measure is not the longest linear measure (RPCL and LPCL are longer), so the error may arise either from thermal deformation of plastics during 3D printing or from potential volume reconstruction software error (Mitsouras et al. 2015, Scarfe and Allan 2008). Moreover, it would be expected that anisotropic voxels should produce errors in the measures aligned with Z axis or oblique measures (Scarfe and Allan 2008), which was not the case. High porosity and rounded shape of the condyle region could be the main reasons for the considerable BW underestimation by radiological scanning, which should be the matter of future research.

We gave special attention to the smallest measures, such as SW and SH, and noticed that SD of these measures presented a considerable percentage of the whole measure. As described in the results, SW's (smallest measure) SD was more significant than the average SD of all measures combined. We decided to divide all measures average value with the SD to numerically express the reliability of the measurements, scoring them from the lowest (least reliable) to the highest (most reliable). The lowest number, belonging to the SH—the second shortest measure—can be explained by specific anatomical site: the pointy alveolar ridge between the central lower incisor teeth may not be displayed and measured correctly on lower-resolution scans. The attempt to improve small measures reading with magnification, by repeating the SW measuring process with 15x magnification, reduced the Y-axis's 3D axis correction percentage value by half (Table 6) in all cases except CBCT0.25.

Another frequently mentioned potential source of inaccuracy is voxel anisotropy. According to Dalrymple and associates, narrow collimation mode should produce isotropic voxels, while wide collimation mode should produce anisotropic voxels (Dalrymple et al. 2007). However, the cited study did not provide further acquisition data; therefore, we selected only the clinically relevant scan protocols that achieve only anisotropic MSCT voxels. It is important to outline that in routine clinical work the voxel size is not calculated and the radiologist chooses protocols based on the literature and previous experience. In contrast, the widely used CBCT is well known for creating isotropic data (Scarfe and Fartman 2008). Thus, we strived to examine the advantages or disadvantages of standard- and high-resolution CBCT/MSCT scanning images by comparing them mutually and to MM based on these scans. Our 3D axis correction strategy was partially successful in volume measure correction for anisotropic and unsuccessful for isotropic radiological protocols (Table 7).

We noted the most significant inaccuracy in 3D linear measurements performed on the CBCT and MSCT volume reconstructions. Similarly, Periago et al. reported differences of 2–3 millimeters between cone-beam 3D reconstruction measurements and actual measurements (Periago et al. 2008). This has been a topic among radiologists for a long time, and it is noted that the measuring is more precise if performed on 2D slices, or simultaneously on both 2D slices and volume reconstruction, than on the reconstructed 3D models alone (Fernandes et al. 2015, Aksoy et al. 2016). It is widely accepted that user-defined rendering parameters as well as locating different landmarks on shiny and shaded surfaces in 3D space introduce majority

of inaccuracies (Periago et al. 2008; Waltrick et al. 2013; Baumgaertel et al 2009). Therefore, if used solely, the volume rendering is considered an interactive, highly subjective process that can finally alter results. However, 3D-rendered objects represent a useful tool for qualitative assessment (Fernandes et al. 2015; Periago et al. 2008).

From the results of our research, the most proper radiological protocols for MM 3D printing were high- and standard-resolution CBCT, with Dental 2.0 H60s MSCT protocol performing almost the same as standard-resolution CBCT (*Sum of difference* column of Table 5). These results are mostly in line with the previous findings of Vani and Prasad (Vani and Prasad 2017). Their work found no significant difference between linear measures taken on dry mandible and CBCT scan, suggesting its suitability for MM fabrication. However, this issue demanded further clarification due to the fact that all of the linear measures taken in the study of Vani and Prasad were oriented only vertically (aligned with the Z axis of Cartesian coordinate system). In addition, the longest set of measures taken had to be excluded from the analysis due to insufficient agreement of the repeated measures.

Besides these issues, there is a need for defining the MSCT protocol that is the most suitable for mandibular reconstruction MM and SG fabrication. The protocol officially recommended by Siemens for jaw analyses on SOMATOM Sensation 16 - Dental 0.75 H60s produced less accurate MM than did the wide-collimation mode of the same protocol—Dental 2.0 H60s. As for the protocol InnerEarUHR 0.6 U90u, even though it ranked the third by preciseness in the *Measurement rank* column, it fell to the fifth position in the *Sum of difference score* column and has shown to be even less accurate than the previous two protocols (Table 5). Lastly, the reconstructions in kernel (H30s and H30u) and window (Base orbith) properties for soft tissues have shown to reduce the accuracy of every protocol, most notably of Dental 2.0, which dropped from the third to the eight position (Table 5).

Comparing our results with other studies, we found that the majority of linear measures on DICOM data in other studies were underestimated, or shorter than those on the scanned object, while a very small number of linear measures were overestimated (Vani and Prasad 2017; Periago et al. 2008). However, no studies have discussed the possibility of grouping overestimation of linear measurements according to MSCT or CBCT plains intersection or according to Cartesian axis of the 3D model derived from DICOM data (Serrano et al. 2019; Mitsouras et al. 2015). That is why we were intrigued by our results related to the SW measure. It was overestimated in all of the cases, as shown in the *CT, CBCT 2D – Mandible* column and the *MM – Mandible* column of Table 4. For other four measures combined, in both columns, there were only six overestimates (9.375%) out of 64 measures. Waltrick et al. found that measures on CBCT (0.2, 0.3 and 0.4 voxel sizes) underestimated real mandibular measures in 60.2% of cases, with all errors under 1 mm (Waltrick et al. 2013). The reported errors are in line with the findings from our research, but the total percentage of underestimated measures on both DICOM and MM measurements in our research was 72.5%. However, the choice of measures used in the work of Waltrick and associates was such that all of them presented the combination of two or even all three of the 3D virtual model axes that could be derived from DICOM files, so the errors could not be related to any particular axis. Baumgaertel et al. found that CBCT measures were constantly underestimated. They offered two explanations: software-related (measures are taken from center to center of the voxel depicting an object, instead of from border to border of an object), and segmentation-related (threshold value of the segmentation determines if "hybrid voxels" on the border of hard and soft tissue would make the object larger or smaller) (Baumgaertel et al 2009). These two theories can explain underestimation of CBCT measurements in comparison to physical measures, but they cannot clearly explain a 100% overestimation of the SW measure. A potential explanation would be

that the circular path of CBCT and MSCT radiation source around the specific V shape of the mandible creates an increased attenuation effect on the region of mandibular symphysis, which leads to increased gray value in “hybrid voxels” on the air/cortical bone border.

Practical consideration of overestimation and underestimation of the linear and volumetric measures on a DICOM volume is directly connected to bone MM and SG. In order to fabricate usable bone SG, one should use a 3D model or MM slightly bigger than the actual bone. This is because most measures we took on radiological images of the mandible were smaller than that on the original bone. In addition, there is a need to make SG just that much larger on the contact surface to the bone to ensure the proper fitting on the target bone. That is why we added the standard deviation of the MM linear measures to the difference of linear measurements of MM and mandible to maximize the 3D axis correction value.

The results of the present study have clearly shown that the most accurate MM of the mandible are achievable with CBCT0.25 and CBCT0.35, closely followed by Dental 2.0 H60s MDCT protocol. It should be kept in mind that the radiation dose should also be taken into account when planning the therapy. Ali et al. found that average effective radiation dose for human mandible CBCT was 0.25 mSv for Scanora 3D and 0.33 mSv for 3D Acutomo 80 device, while MSCT effective radiation dose of the same region was 0.474 mSv for the Somatom Sensation 16® and even higher for the other MSCT scanners tested (Ali et al. 2015, Loubele et al. 2009). These results suggest that Dental 2.0 H60s MDCT protocol has advantage over CBCT protocols. We also correlated the overestimation and underestimation of the linear measures on DICOM volume reconstruction with planes and axis of the reconstructed volume. Based on these results, we recommended 3D axis correction or scaling of the 3D model resulting from DICOM volume reconstruction. Such correction guidelines can be recommended with high reliability during the specific patient-tailored reconstructive procedures of the mandible in oral and maxillofacial surgery. More studies with greater sample size are needed to generalize the observed results to other fields of medicine, archeology, and forensic science.

In the next phase of the research, we focused on guided surgery and artificial graft overcritical defect bone reconstruction on an animal model. After determining optimal protocols for MM and SG fabrication, we engineered 3D-printed bone construct mimicking the bone tissue architectural pattern, onto which bone cells can attach, proliferate, migrate and produce new bone. The important role of surgical planning and 3D printing was to precisely plan the resection of the rabbit’s ulna after CBCT scanning was done, to design and 3D-print the porosity and pore connectivity of the construct and to design and 3D-print the reconstruction graft with the attachments that would ensure the primary stability (Micic et al. 2020). The last was achieved by designing the attachments on the construct’s ends, which were in the contact with the resected bone ends by grasping both bone ends with cylindrical structures of biodegradable PLA, while leaning on the inner surface of the resected bone with porous net-like PLA membrane and nHAP.

From an architectural perspective, the 3D construct exhibited the necessary porosity (>50% total porosity and >100 μm average pore size) to meet the structural requirements for successful regeneration processes. This allowed for effective ion exchange and homeostasis (Cao et al., 2015; Fernandez-Yague et al., 2015; Komlev et al., 2015). In terms of chemical properties, a bone replacement material should be hydrophilic and possess favorable wettability when in contact with human blood in order to achieve good osteointegration (Wen et al., 2017). Our engineered construct demonstrated super-hydrophilicity, achieving complete wetting in just 0.234 seconds.

The surface area of newly formed bone is known to reflect active osteogenesis and bone remodeling. Additionally, the presence of inflammatory cells is a critical parameter for assessing the biocompatibility of the bone substitute (Zhang B. et al., 2017). All the evidence obtained in this study indicates the biocompatibility of the construct and successful bone regeneration. Histological analysis revealed active ossification in the regeneration process. After 12 weeks of healing, mature mineralized lamellar bone with Haversian osteons and blood vessels, as well as a mature bone marrow, were observed, indicating substantial regeneration of the bone defect. These findings align with the results published by Tang et al. (2016), who achieved almost complete bone regeneration using a promising new material, trimodal macro/micro/nano mesoporous bioactive glass, enhanced with the growth factor rhBMP-2. The presence of numerous strongly stained BMP2-positive cells in the regions of new bone matrix is consistent with their role in recruiting host cells during bone healing, as these factors are associated with chemotaxis induction (Dang et al., 2017). Moreover, BMP-like factors in the bloodstream have been shown to adsorb onto hydroxyapatite surfaces and promote osteoblast adhesion. Therefore, it can be inferred that the 3D-printed bone replacement provides an osteoinductive and osteoconductive microenvironment that activates trophic signals, recruiting proteins and growth factors to the site of the defect. OCN, a late-stage marker expressed during the maturation of osteoblasts, is highly specific to osteoblast mineralization (Dang et al., 2017). The higher expression of BMP2 compared with OCN is likely due to the sacrifice of the animals after only 12 weeks, which is an insufficient period for the completion of the bone mineralization process.

Generally, the following four surface properties of biomaterials regulate bone formation: chemical composition, surface energy, nano- and microtopography and surface roughness (Hutchens et al. 2016; Sohn and Oh 2019). Desirable osteointegration of the engineered construct is presumably due to its super-hydrophilicity in combination with the presence of nanostructure patterns favorable for superior adhesion of cells. We succeeded to fabricate the bone construct with satisfactory surface properties and microarchitecture (open porosity of 64% and pore connectivity of 34.8 pores per mm^3) that allowed vascularization, cells migration and proliferation, not only on the construct's surface, but also within its internal compartments. Due to the optimal degradation speed, new bone formation and construct's degradation seem synchronized, which further provided bone osteoinductive capacity.

Numerous research groups have devoted efforts to the reconstruction of large-scale bone defects (Oryan et al., 2016; Yang et al., 2014; Fassbender et al., 2014; Xu et al., 2012). Compared with under-critical size bone defects, the challenges in bone reconstruction for larger defects arise from the difficulty of achieving optimal vascularization in the central part of the defect. This complexity is attributed to the nature of bone healing and long time required (approximately 6 months to regenerate), which means that bio-degradability of the replacement material should be balanced and located predominantly on the interface between old bone and bone scaffold (Zhang B. et al., 2017).

Significant progress has been made in the field through the utilization of novel approaches. These include concepts such as seeding stem cells on the bone construct prior to implantation, employing prefabricated constructs containing new donor bone in bioreactors, and incorporating growth factors into the cell culture medium (Zhang H. et al., 2017; Temple et al., 2014). These advancements have been particularly effective when the bone integrity is preserved, with the defect surrounded by old bone on at least three sides. The findings presented in this study align with other investigations where cylindrical bone voids in rat tibia (Nezhurina et al., 2018), rabbit calvaria (Jokanovic et al., 2017) or sheep femoral bone (Hettwer et al., 2019) were reconstructed. Thang and colleagues (2016) successfully reconstructed a 16-mm

marginally resected radius in rabbits using mesoporous bioactive glass with enhanced compressive strength. Notably, the bone construct alone resulted in 10% new bone formation, while the addition of BMP2 increased new bone formation to 40%. Additionally, similar to Zhang B. et al. (2017) and Zhang P. et al. (2009), our study took a step further by reconstructing a long bone defect with interrupted bone integrity (full diameter of the ulna was removed).

There are two key distinctions between our study and these novel investigations. Firstly, the our study focused on reconstructing the ulna instead of the radius, which is a significant advancement considering the estimated mechanical load shared by the ulna during ulna–radius compressive strain (Lu et al., 2012). Secondly, by engineering a bone substitute with desirable osteoinductive properties, our approach has the potential to address a critical requirement mentioned in the aforementioned papers, but without the use of stem cells and growth factors. It is important to interpret the present results while considering a notable limitation regarding the number of experimental animals involved. Future studies are planned to confirm these promising preliminary results using a larger number of animals and in larger animal models.

Next issue is related to reconstruction of over-critical size bone defects. Despite the introduction of numerous formulations for bone replacement in the past decade, none of the solutions meet a crucial requirement for healing centimeter-sized bone defects: providing sufficient mechanical support and serving as "interactive" biomaterial capable of coordinating material resorption and new bone formation (Yang C. et al., 2018; Sohn and Oh, 2019). Consequently, achieving bone repair within the central part of the construct is challenging, resulting in fibrous tissue filling the defect and thus jeopardizing vascularization. In our research, we successfully addressed some critical material and biochemical issues, leading to the reconstruction of 1/4 of the rabbit's ulna. In our study this was accomplished by employing two innovative solutions.

Namely, the construct was 3D-printed using a novel nHAP-based material that differs from current formulations in the following crucial aspect: the material's solubility matches that of natural bone, allowing for the ideal time frame for bone apposition and material degradation without the formation of fibrous tissue at the interface. Additionally, in the central part of the construct where new bone naturally forms during the final stages of the regenerative process, the construct exhibited a slightly lamellar structure. Our findings confirmed the absence of any harmful effects of the 3D-printed construct on stem cells from the apical papilla (SCAP) in direct contact. Furthermore, leachable products from the construct significantly stimulated cell migration.

The primary aim of this part of the study was to assess the potential of the construct to induce osteogenesis *in vitro*, both alone and in the presence of osteogenic induction medium. SCAP cultured in induction and growth medium served as a control group. A study by Miles et al. (Miles et al., 2019) investigated the osteoinduction of microcapsules containing HAP microgranules on mesenchymal stem cells (MSCs) in both growth and osteogenic medium. Microcapsules with HAP stimulated MSC mineralization in osteogenic medium from the first week, but significant mineralization did not occur when only growth medium was added to the culture. In contrast, SCAP within the construct were able to produce mineralized extracellular matrix (ECM) regardless of the medium used. The construct's properties guided cells towards osteogenic differentiation, as evidenced by alkaline phosphatase production at day 7, mineralized deposits after 3 weeks of culture, and qualitative SEM images at day 7, 14, and 21 in both media. The most significant finding was the absence of differences in mineralization deposits between control cells cultivated in osteogenic medium and cells in the construct cultivated in plain growth medium (at week 3 of culture). Furthermore, the addition of osteogenic medium further amplified the construct's osteogenic properties.

As previously described, the scaffold's structure primarily determines the extent of cell migration and differentiation, bone ingrowth, vascularization, and mass transfer between cells and the environment (Bueno and Glowacki, 2009). The present findings are likely the result of modifications in the construct's surface nano-topography, increasing the concentration of atoms and crystal grains and the surface area-to-volume ratio. These modifications improve cell adhesion, bone ingrowth, osteointegration, and mechanical properties (Webster et al., 1999). Careful histological analysis confirmed that osteoblasts were able to infiltrate such a material structure and await the proximity of blood vessels and newly deposited bone.

The next innovation in our study was the successful printing of the nHAP-based construct with both desirable mechanical support and high porosity, enabling the required osteoconductivity of the material. The combination of the construct's composition (with magnesium and phosphorus additions), mechanics, and specific 3D architecture appeared to provide multiple mechanochemical stimuli that contribute to better temporal control of the healing process and cell modulation.

The demonstrated concept suggests that large-size bone defects can be reconstructed by personalized approach, using customized bone construct fabricated by 3D printing, out of osteinductive biomaterial, without use of growth factors and stem cells. This is a promising step toward clinical implementation, but using novel biomaterials in research involving humans is a demanding and long-lasting process that cannot be achieved in the span of this particular research.

In the final part of our research, we focused on the clinical implementation of guided surgery with “in house” 3D printing. Indeed, from the practical point of view, clinical implementation of the techniques determined in the previous steps of the research was the most important phase. In this phase, we summed up the experience from the previous two research steps usable in clinical practice.

Although the total time of surgery was not significantly shorter in the experimental than in the control group ($p=0.131$), on average 84 minutes less per operation is a considerable saving in the time and cost of the procedure. Tarsitano et al. found that the total operation room (OR) time decreased by 115.5 minutes (statistically significant) in the group of patients operated with the use of computer-aided design and manufacturing (3D printing) compared with the control group (Tarsitano et al, 2016). Gil and associates reported the average decrease of OR time of 64 min (no significance), while Serrano and associates found the OR time reduction to be the most frequent clinical end point to be reported (in five out of 14 studies analyzed) with the average time reduction of 21.2% ($p<0.001$) (Gil et al. 2015, Serrano et al. 2019). A shortcoming of our study is failure to register the OR reconstruction and resection time separately, as part of the total OR time. That way, it would be clear from what specific part of operation procedure is time reduction originating, and most probably the statistical significance would be reached by analyzing the time difference between the experimental and the control group.

Large difference in average hospitalization after surgery between the experimental and the control group is partially because of the one case of post-surgery complications found in the control group. Excluding the case with complications would reduce the average hospital stay for the control group to 10.75 days, but there would still be more than two-day difference to the experimental group, and the hypothesis that the use of virtual planning, SG and MM would reduce hospital stay for this type of surgery was confirmed by t-test ($p=0.031$). However, since the complication occurred due to inadequate placement and orientation of the transplant, the occurrence that we aim to eliminate by virtual surgery planning, SG and MM

implementation, we consider that the results are representative even when including the case with the mentioned complications. Although not most important, the total cost of the procedure and occupation of the hospital capacity have high priority for the public health, especially in the time of potential pandemic, when resources become very limited. By saving 84 minutes in the OR and 9.2 days of the hospital stay on average, our study demonstrated that implementing the proposed procedures is a high priority for our health system.

Tarsitano et al. have found that the total time saving in the OR (determined as a cost of operation per one minute, multiplicated by minutes saved) is equal to or greater than the SG and MM production cost (Tarsitano et al. 2016 jul). We cannot be precise about the cost of the procedure, since every mandibular reconstruction had different levels of complexity and different size; yet, with consideration of the significant reduction in post-surgery hospitalization in the experimental group, we can certainly say that these savings are greater than the expenses of virtual planning, SG and MM production.

An important variable used in our study that could not be compared with other scientific papers was the time prior to surgery, or time spent on virtual planning and fabrication of all elements needed for the guided surgery. It could not be compared because of the fact that this variable was usually overlooked or at least it was not described properly in the scientific papers dealing with this subject. In one case of mandibular reconstruction via fibular flap, where semiautomatic fibular resection guide was made in commercial software, the time of modeling procedure was stated to be only around 3 hours (Yuan 2016). It should be noted that this particular case was indeed exceptional because of the size and shape of the tumor that only allowed for two separate markers to be used as the mandibular resection guide, which made the modeling procedure shorter and simpler. The majority of scientific reports are specific about the time needed to complete the whole procedure from radiological scanning to actual planned surgery, but those provide specific information report up to 2 weeks needed (Martelli et al. 2016). As mentioned in the introduction, such a long-time span can lead to inadequate healing. The fact that pre-surgery time or time-to-surgery cannot be compared with other scientific papers where the same type of surgery planning was used leaves us with the assumption that the already significant difference in hospitalization time is in reality even greater, because of the production time difference between remote and in house production of SG and MM.

The most important result of our study, and in the same time the most important advocate for implementation of the methods we used, is the final functional and esthetic result and patient satisfaction with the procedure. Having a need to compare a variety of cases that demanded different type of mandibular resection, we had to choose a methodological approach that was robust enough to function in all cases and at the same time sensitive enough. Considering the usual methods, used by Tarsitano et al., where the authors measured the deviation of the postoperative mandible from the mandibular midline and compared bi-gonial diameter and mandibular angle, we found several shortcomings (Tarsitano et al. 2016). It is not unusual to register certain amount of asymmetry in the patient's anatomy even preoperatively, so the strategy of mandibular midline would not be the best solution for such patients. Bi-gonial diameter and mandibular angle measurements may be less effective measures in types of defect where the mandibular ramus and mandibular angle are not affected. Instead, we decided to use the preoperative 3D model of the mandible (as used in the leading 3D planning step) as an ideal and desired shape and size of neomandible, and the postoperative 3D model of the reconstructed mandible as a final result of the whole procedure. Regardless of the technique, autograft from each donor site cannot precisely match the shape and size of the mandible, and every donor site has some shortcomings. For example, a drawback of the fibula flap is the

relative lack of height, scapular flap has a relative lack of thickness, and so on. Thus, we came to the conclusion that measuring linear deviation from an ideal position or from the line of symmetry is a less objective criterion, knowing in advance that we cannot precisely mimic the preoperative mandible shape and size with the autograft, but we can measure what part of neomandible has volumetric misalignment that protrudes out of the preoperative or ideal mandible volume. This way, by measuring only the volumetric difference out of the volume of the preoperative mandible, we were able to quantify the result of operation more objectively. Apart from the volumetric discrepancy, we measured a maximal linear deviation from the ideal mandible shape and size both laterally and in antero-posterior direction. All three of these parameters showed significant difference in favor of the experimental group. Due to limitations of our study, our method for comparing the final functional and esthetic result was dealing only with the mandibular bone, and did not take into account soft tissue profile or eventual dental restorations. Nevertheless, the facts that all three spatial parameters of function and symmetry were better in the experimental group and that the patient satisfaction was significantly increased in the experimental group support the necessity of implementation of our methods. Furthermore, we noticed positive correlation between the number of planning elements involved in surgery and the final functional and esthetic result (Figure 28). Hence, the more planning elements are used, the better result we can expect.

With our work, we advocate for the implementation of virtual planning, SG and MM in clinical practice (Micic&Djuric 2023). We have shown clear benefits from a range of methods, majority of which are expected to become a standard in clinical practice in a span of a few future years, and neglecting these facts could leave domestic medicine behind in the field of mandibular reconstruction. We have also shown the efficiency of the new combined resection and reconstruction guide for mandibular reconstruction as well as the concept of “in house 3D printing”.

6. Conclusion

This research pioneered the implementation of 3D printing in fields of surgical reconstruction of large skeletal defects and bone tissue engineering in Serbia. In the process, we managed to find optimal radiological protocols for fabrication of medical models and surgical guides used in large mandibular defect reconstruction. We also gave recommendation for correction of 3D models derived from commonly used radiological protocols of scanned anatomical regions of interest so they may be presented more accurately.

In Center of Bone Biology, we engineered customized 3D printer for bone replacement scaffold fabrication, and produced, characterized and implemented a scaffold made of novel (nHAP/PLGA) bone replacement material for reconstruction of overcritical size bone defect of rabbit`s ulna. This was the first successful reconstruction of large defects on load bearing long bones, without using external fixation, bone morphogenic proteins, growth factors and stem cells.

As a final phase of our research, we successfully implemented methods previously tested in laboratory and animal experiments in clinical environment. We successfully applied virtual surgery planning with medical models and surgical guides fabrication in seven surgical treatments of large mandibular defects, significantly improving surgical outcome.

In summary, we advocate for more close and clinically oriented multidisciplinary cooperation in implementing new and innovative technology of 3D printing in medicine and especially in bone defect reconstruction. We demonstrated favorable effects of successful bone tissue engineering and virtual surgery planning compared to a conventional surgical approach. After successful testing in clinical context, we are advocating for implementation of “in house” 3D printing and virtual planning of bone reconstruction surgical procedures. We hope that this research will be the starting point for future research and development, as well as for broader clinical implementation.

7. References

Aksoy S, Kelahmet U, Hincal E, Oz U, Orhan K. (2016). Comparison of linear and angular measurements in CBCT scans using 2D and 3D rendering software. Biotechnology and Biotechnological Equipment, 30(4), 777–784. doi: 10.1080/13102818.2016.1174077

Ali AS, Fteita D, Kulmala J. (2015). Comparison of physical quality assurance between Scanora 3D and 3D Accuitomo 80 dental CT scanners, Libyan Journal of Medicine, 10:1. doi: 10.3402/ljm.v10.28038

Amin W, Saleh MW. (2015). Accuracy of a customized volumetric rendering program in linear measurement of cone beam and multi-slice computed tomography derived three-dimensional images. Journal of Oral and Maxillofacial Radiology, 3(2), 33. doi: 10.4103/2321-3841.157515

Auriemma E, Voorhout G, Barthez PY. (2007). Determination of optimal window width and level for measurement of the canine pituitary gland height on computed tomographic images using a phantom. Veterinary Radiology and Ultrasound, 48(2), 113–117. doi: 10.1111/j.1740-8261.2007.00214.x

Ballard DH, Trace AP, Ali S, Hodgdon T, Zygmont ME, DeBenedectis CM, Smith SE, Richardson ML, Patel MJ, Decker SJ, Lenchik L. (2018). Clinical Applications of 3D Printing: Primer for Radiologists. Academic Radiology, 25(1), 52–65. doi: 10.1016/j.acra.2017.08.004

Baumgaertel S, Palomo JM, Palomo L, Hans MG. (2009). Reliability and accuracy of cone-beam computed tomography dental measurements. American Journal of Orthodontics and Dentofacial Orthopedics, 136(1), 19–25. doi: 10.1016/j.ajodo.2007.09.016

Berman B. (2012). 3-D printing: The new industrial revolution. Business Horizons, 55(2), 155–162. doi: 10.1016/j.bushor.2011.11.003

Bharatha A, Hirose M, Hata N, Warfield SK, Ferrant M, Zou KH, Suarez-Santana E, Ruiz-Alzola J, D'Amico A, Cormack RA, Kikinis R, Jolesz FA, Tempany CMC. (2001). Evaluation of three-dimensional finite element-based deformable registration of pre- and intraoperative prostate imaging. Medical Physics, 28(12), 2551–2560. doi: 10.1118/1.1414009

Bücking TM, Hill ER, Robertson JL, Maneas E, Plumb AA, Nikitichev DI. (2017). From medical imaging data to 3D printed anatomical models. PLoS ONE. 12(5), 1–10. doi: 10.1371/journal.pone.0178540

Bueno EM, Glowacki J. (2009). Cell-free and cell-based approaches for bone regeneration. In Nature Reviews Rheumatology. 5, (12), 685–697. doi: 10.1038/nrrheum.2009.228

Cao X, Wang J, Liu M, Chen Y, Cao Y, Yu X. (2015). Chitosan-collagen/organomontmorillonite scaffold for bone tissue engineering. Frontiers of Materials Science. 9(4), 405–412. doi: 10.1007/s11706-015-0317-5

Dang PN, Herberg S, Varghai D, Riazi H, Varghai D, McMillan A, Awadallah A, Phillips LM, Jeon O, Nguyen MK, Dwivedi N, Yu X, Murphy WL, Alsberg E. (2017). Endochondral Ossification in Critical-Sized Bone Defects via Readily Implantable Scaffold-Free Stem Cell Constructs. Stem Cells Transl Med. 6(7):1644-1659. doi: 10.1002/sctm.16-0222.

Dalrymple NC, Prasad SR, El-Merhi FM, Chintapalli KN. (2007). Price of isotropy in multidetector CT. Radiographics. 27(1), 49–62. doi: 10.1148/rg.271065037

Della Bona, A., Cantelli, V., Britto, V. T., Collares, K. F., & Stansbury, J. W. (2021). 3D printing restorative materials using a stereolithographic technique: a systematic review. In Dental Materials. (Vol. 37, Issue 2, pp. 336–350). Elsevier Inc. doi: 10.1016/j.dental.2020.11.030

Elsawy, MA, Kim KH, Park JW, Deep A. (2017). Hydrolytic degradation of polylactic acid (PLA) and its composites. Renewable and Sustainable Energy Reviews. 79, 1346–1352. doi: 10.1016/j.rser.2017.05.143

Eltes PE, Kiss L, Bartos M, Gyorgy ZM, Csakany T, Bereczki F, Lesko V, Puhl M, Varga PP, Lazary A. (2020). Geometrical accuracy evaluation of an affordable 3D printing technology for spine physical models. J Clin Neurosci. 72:438-446. doi: 10.1016/j.jocn.2019.12.027.

Fassbender M, Minkwitz S, Thiele M, Wildemann B. (2014). Efficacy of two different demineralised bone matrix grafts to promote bone healing in a critical-size-defect: a radiological, histological and histomorphometric study in rat femurs. Int Orthop. 38;(9):1963-9. doi: 10.1007/s00264-014-2321-2

Fernandes TM, Adamczyk J, Poleti ML, Henriques JF, Friedland B, Garib DG. (2015). Comparison between 3D volumetric rendering and multiplanar slices on the reliability of

linear measurements on CBCT images: an in vitro study. J Appl Oral Sci. Jan-Feb;23(1):56-63. doi: 10.1590/1678-775720130445.

Fernandez-Yague MA, Abbah SA, McNamara L, Zeugolis DI, Pandit A, Biggs MJ. (2015). Biomimetic approaches in bone tissue engineering: Integrating biological and physicomechanical strategies. Adv Drug Deliv Rev. Apr;84:1-29. doi: 10.1016/j.addr.2014.09.005.

Gandolfi MG, Zamparini F, Degli Esposti M, Chiellini F, Aparicio C, Fava F, Fabbri P, Taddei P, Prati C. (2018). Polylactic acid-based porous scaffolds doped with calcium silicate and dicalcium phosphate dihydrate designed for biomedical application. Mater Sci Eng C Mater Biol Appl. 1;82:163-181. doi: 10.1016/j.msec.2017.08.040.

Ganry L, Hersant B, Bosc R, Leyder P, Quilichini J, Meningaud JP. (2018). Study of medical education in 3D surgical modeling by surgeons with free open-source software: Example of mandibular reconstruction with fibula free flap and creation of its surgical guides. J Stomatol Oral Maxillofac Surg. 119(4):262-267. doi: 10.1016/j.jormas.2018.02.012.

Hettwer W, Horstmann PF, Bischoff S, Güllmar D, Reichenbach JR, Poh PSP, van Griensven M, Gras F, Diefenbeck M. (2019). Establishment and effects of allograft and synthetic bone graft substitute treatment of a critical size metaphyseal bone defect model in the sheep femur. APMIS. 127(2):53-63. doi: 10.1111/apm.12918.

Hong Q, Lin L, Li Q, Jiang Z, Fang J, Wang B, Liu K, Wu Q, Huang C. (2021). A direct slicing technique for the 3D printing of implicitly represented medical models. Comput Biol Med. 135:104534. doi: 10.1016/j.compbiomed.2021.104534.

Hou X, Yang DD, Li D, Zeng L, Li C. (2020). 3D Slicer and Sina appilication for surgical planning of giant invasive spinal schwannoma with scoliosis: A case report and literature review. Neurochirurgie. 66(5):396-399. doi: 10.1016/j.neuchi.2020.06.131.

Hutchens SA, Campion C, Assad M, Chagnon M, Hing KA. (2016). Efficacy of silicate-substituted calcium phosphate with enhanced strut porosity as a standalone bone graft substitute and autograft extender in an ovine distal femoral critical defect model. J Mater Sci Mater Med. 27(1):20. doi: 10.1007/s10856-015-5559-3.

Jewer DD, Boyd JB, Manktelow RT, Zuker RM, Rosen IB, Gullane PJ, Rotstein LE, (1989) Freeman JE. Orofacial and mandibular reconstruction with the iliac crest free flap: a review of 60 cases and a new method of classification. Plast Reconstr Surg. 84(3):391-403; discussion 404-5.

Jokanovic, V., Čolović, B., Marković, D., Petrović, M., Jokanović, M., Milosavljević, P., & Sopta, J. (2016). In Vivo Investigation of ALBO-OS Scaffold Based on Hydroxyapatite and PLGA. Journal of Nanomaterials. vol. 2016, Article ID 3948768, 10 pages doi: 10.1155/2016/3948768

Jokanović V, Čolović B, Marković D, Petrović M, Soldatović I, Antonijević D, Milosavljević P, Sjerobabin N, Sopta J. (2017). Extraordinary biological properties of a new calcium hydroxyapatite/poly(lactide-co-glycolide)-based scaffold confirmed by in vivo investigation. Biomed Tech (Berl). 62(3):295-306. doi: 10.1515/bmt-2015-0164.

Karadzic I, Vucic V, Jokanovic V, Debeljak-Martacic J, Markovic D, Petrovic S, Glibetic M. (2015). Effects of novel hydroxyapatite-based 3D biomaterials on proliferation and osteoblastic differentiation of mesenchymal stem cells. J Biomed Mater Res A. 103(1):350-7. doi: 10.1002/jbm.a.35180.

Keating SC, Thomas AA, Flecknell PA, Leach MC. (2012). Evaluation of EMLA cream for preventing pain during tattooing of rabbits: changes in physiological, behavioural and facial expression responses. PLoS One. 7(9):e44437. doi: 10.1371/journal.pone.0044437.

Komlev VS, Popov VK, Mironov AV, Fedotov AY, Teterina AY, Smirnov IV, Bozo IY, Rybko VA, Deev RV. (2015). 3D Printing of Octacalcium Phosphate Bone Substitutes. Front Bioeng Biotechnol. 8;3:81. doi: 10.3389/fbioe.2015.00081.

Lee KG, Lee KS, Kang YJ, Hwang JH, Lee SH, Park SH, Park Y, Cho YS, Lee BK. (2018). Rabbit Calvarial Defect Model for Customized 3D-Printed Bone Grafts. Tissue Eng Part C Methods. 24(5):255-262. doi: 10.1089/ten.TEC.2017.0474.

Liu YF, Xu LW, Zhu HY, Liu SS. (2014). Technical procedures for template-guided surgery for mandibular reconstruction based on digital design and manufacturing. Biomed Eng Online. 23;13:63. doi: 10.1186/1475-925X-13-63.

Liu L, Shi G, Cui Y, Li H, Li Z, Zeng Q, Guo Y. (2017). Individual construction of freeform-fabricated polycaprolactone scaffolds for osteogenesis. Biomed Tech (Berl). 62(5):467-479. doi: 10.1515/bmt-2016-0005.

Loubele M, Bogaerts R, Van Dijck E, Pauwels R, Vanheusden S, Suetens P, Marchal G, Sanderink G, Jacobs R. (2009). Comparison between effective radiation dose of CBCT and MSCT scanners for dentomaxillofacial applications. Eur J Radiol. 71(3):461-8. doi: 10.1016/j.ejrad.2008.06.002.

Lu Y, Thiagarajan G, Nicolella DP, Johnson ML. (2012). Load/strain distribution between ulna and radius in the mouse forearm compression loading model. Med Eng Phys. 34(3):350-6. doi: 10.1016/j.medengphy.2011.07.022.

Mah P, Reeves TE, McDavid WD. (2010). Deriving Hounsfield units using grey levels in cone beam computed tomography. Dentomaxillofac Radiol. 39(6):323-35. doi: 10.1259/dmfr/19603304.

Micic M, Antonijevic D, Milutinovic-Smiljanic S, Trisic D, Colovic B, Kosanovic D, Prokic B, Vasic J, Zivkovic S, Milasin J, Danilovic V, Djuric M, Jokanovic V. (2020) Developing a novel resorptive hydroxyapatite-based bone substitute for over-critical size defect reconstruction: physicochemical and biological characterization and proof of concept in segmental rabbit's ulna reconstruction. Biomed Tech (Berl). 65(4):491-505. doi: 10.1515/bmt-2019-0218.

Micic M, Jadzic J, Milenkovic P, Antic S, Antonijevic D, Djuric M. (2023) Testing of Different Scanning Protocols Used for Precise 3D-printing of Mandibular Models. J Craniofac Surg. Published ahead of print on May 25 2023. doi: 10.1097/SCS.0000000000009421.

Micic M, Djuric M. (2023) Acelularna 3d štampa u hirurškoj rekonstrukciji koštanih defekata. Medicinski Podmladak. Vol. 74 Br.3. doi: 10.5937/mp74-43883

Miles KB, Maerz T, Matthew HWT. (2019). Scalable MSC-derived bone tissue modules: In vitro assessment of differentiation, matrix deposition, and compressive load bearing. Acta Biomater. 1;95:395-407. doi: 10.1016/j.actbio.2019.01.014.

Mitsouras D, Liacouras P, Imanzadeh A, Giannopoulos AA, Cai T, Kumamaru KK, George E, Wake N, Caterson EJ, Pomahac B, Ho VB, Grant GT, Rybicki FJ. (2015). Medical 3D Printing for the Radiologist. Radiographics. 35(7):1965-88. doi: 10.1148/rg.2015140320.

Numajiri T, Tsujiko S, Morita D, Nakamura H, Kodama T, Sowa Y. (2017). A fixation guide for the accurate insertion of fibular segments in mandibular reconstruction. International Journal of Oral and Maxillofacial Surgery. 46, 338. doi:10.1016/j.ijom.2017.02.1140

Nezhurina EK, Karalkin PA, Komlev VS, Sviridova IK, Kirsanova VA, Akhmedova SA, Shanskiy YaD, Fedotov AYu, Barinov SM, Sergeeva NS. (2018). Physicochemical and osteoplastic characteristics of 3D printed bone grafts based on synthetic calcium phosphates and natural polymers. IOP Conf. Series: Mater Sci Eng. 347:012047. doi: 10.1088/1757-899X/347/1/012047

Oryan A, Alidadi S, Bigham-Sadegh A, Moshiri A. (2016). Comparative study on the role of gelatin, chitosan and their combination as tissue engineered scaffolds on healing and regeneration of critical sized bone defects: an in vivo study. J Mater Sci Mater Med. 27(10):155. doi: 10.1007/s10856-016-5766-6.

Periago DR, Scarfe WC, Moshiri M, Scheetz JP, Silveira AM, Farman AG. (2008). Linear accuracy and reliability of cone beam CT derived 3-dimensional images constructed using an orthodontic volumetric rendering program. Angle Orthod. 78(3):387-95. doi: 10.2319/122106-52.1.

Pierchala MK, Makaremi M, Tan HL, Pushpamalar J, Muniyandy S, Solouk A, Lee SM, Pasbakhsh P. (2017). Nanotubes in nanofibers: Antibacterial multilayered polylactic acid/halloysite/gentamicin membranes for bone regeneration application. Applied Clay Science. 0–1. doi: 10.1016/j.clay.2017.12.016.

Ragbir M, Brown JS, Mehanna H. (2016). Reconstructive considerations in head and neck surgical oncology: United Kingdom National Multidisciplinary Guidelines. J Laryngol Otol. 130(S2):S191-S197. doi: 10.1017/S0022215116000621.

Robert P, Mauduit J, Frank RM, Vert M. (1993). Biocompatibility and resorbability of a polylactic acid membrane for periodontal guided tissue regeneration. Biomaterials. 14(5):353-8. doi: 10.1016/0142-9612(93)90054-6.

Sander IM, McGoldrick MT, Helms MN, Betts A, van Avermaete A, Owers E, Doney E, Liepert T, Niebur G, Liepert D, Leevy WM. (2017). Three-dimensional printing of X-ray computed tomography datasets with multiple materials using open-source data processing. Anat Sci Educ. 10(4):383-391. doi: 10.1002/ase.1682.

Scarfe WC, Farman AG. (2008). What is cone-beam CT and how does it work? Dent Clin North Am. 52(4):707-30, v. doi: 10.1016/j.cden.2008.05.005.

Schliephake H, Weich HA, Dullin C, Gruber R, Frahse S. (2008). Mandibular bone repair by implantation of rhBMP-2 in a slow release carrier of polylactic acid--an experimental study in rats. Biomaterials. 29(1):103-10. doi: 10.1016/j.biomaterials.2007.09.019.

Serrano C, van den Brink H, Pineau J, Prognon P, Martelli N. (2019). Benefits of 3D printing applications in jaw reconstruction: A systematic review and meta-analysis. J Craniomaxillofac Surg. 47(9):1387-1397. doi: 10.1016/j.jcms.2019.06.008.

Seruya M, Fisher M, Rodriguez ED. (2013). Computer-assisted versus conventional free fibula flap technique for craniofacial reconstruction: an outcomes comparison. Plast Reconstr Surg. 132(5):1219-1228. doi: 10.1097/PRS.0b013e3182a3c0b1.

Sohn HS, Oh JK. (2019). Review of bone graft and bone substitutes with an emphasis on fracture surgeries. Biomater Res. 14;23:9. doi: 10.1186/s40824-019-0157-y.

Sieira Gil R, Roig AM, Obispo CA, Morla A, Pagès CM, Perez JL. (2015). Surgical planning and microvascular reconstruction of the mandible with a fibular flap using computer-aided design, rapid prototype modelling, and precontoured titanium reconstruction plates: a prospective study. Br J Oral Maxillofac Surg. 53(1):49-53. doi: 10.1016/j.bjoms.2014.09.015.

Temple JP, Yeager K, Bhumiratana S, Vunjak-Novakovic G, Grayson WL. (2014). Bioreactor cultivation of anatomically shaped human bone grafts. Methods Mol Biol. 1202:57-78. doi: 10.1007/7651_2013_33.

Tack P, Victor J, Gemmel P, Annemans L. (2016). 3D-printing techniques in a medical setting: a systematic literature review. Biomed Eng Online. 21;15(1):115. doi: 10.1186/s12938-016-0236-4.

Tang W, Lin D, Yu Y, Niu H, Guo H, Yuan Y, Liu C. (2016). Bioinspired trimodal macro/micro/nano-porous scaffolds loading rhBMP-2 for complete regeneration of critical size bone defect. Acta Biomater. 1;32:309-323. doi: 10.1016/j.actbio.2015.12.006.

Tarsitano A, Battaglia S, Crimi S, Ciocca L, Scotti R, Marchetti C. (2016). Is a computer-assisted design and computer-assisted manufacturing method for mandibular reconstruction economically viable? J Craniomaxillofac Surg. Jul;44(7):795-9. doi: 10.1016/j.jcms.2016.04.003.

Tarsitano A, Ciocca L, Scotti R, Marchetti C. (2016). Morphological results of customized microvascular mandibular reconstruction: A comparative study. J Craniomaxillofac Surg. Jun;44(6):697-702. doi: 10.1016/j.jcms.2016.03.007.

Tel A, Costa F, Sembronio S, Lazzarotto A, Robiony M. (2018). All-in-one surgical guide: A new method for cranial vault resection and reconstruction. J Craniomaxillofac Surg. 46(6):967-973. doi: 10.1016/j.jcms.2018.03.020.

Troy KL, Edwards WB. (2018). Practical considerations for obtaining high quality quantitative computed tomography data of the skeletal system. Bone. 110:58-65. doi: 10.1016/j.bone.2018.01.013.

Vani C, Prasad GR. (2017). Evaluation of validity of cone beam CT (CBCT) measurements compared to direct method on human dry mandibles. IAIM. 4(10): 59-66. ISSN: 2394-0034 (O)

Waltrick KB, Nunes de Abreu Junior MJ, Corrêa M, Zastrow MD, Dutra VD. (2013). Accuracy of linear measurements and visibility of the mandibular canal of cone-beam computed tomography images with different voxel sizes: an in vitro study. J Periodontol. 84(1):68-77. doi: 10.1902/jop.2012.110524.

Webster TJ, Siegel RW, Bizios R. (1999). Osteoblast adhesion on nanophase ceramics. Biomaterials. 20(13):1221-7. doi: 10.1016/s0142-9612(99)00020-4.

Wen G, Guo Z, Liu W. (2017). Biomimetic polymeric superhydrophobic surfaces and nanostructures: from fabrication to applications. Nanoscale. 9;9(10):3338-3366. doi: 10.1039/c7nr00096k.

Whyms BJ, Vorperian HK, Gentry LR, Schimek EM, Bersu ET, Chung MK. (2013). The effect of computed tomographic scanner parameters and 3-dimensional volume rendering techniques on the accuracy of linear, angular, and volumetric measurements of the mandible. Oral Surg Oral Med Oral Pathol Oral Radiol. 115(5):682-91. doi: 10.1016/j.oooo.2013.02.008.

Xu L, Lv K, Zhang W, Zhang X, Jiang X, Zhang F. (2012). The healing of critical-size calvarial bone defects in rat with rhPDGF-BB, BMSCs, and β-TCP scaffolds. J Mater Sci Mater Med. 23(4):1073-84. doi: 10.1007/s10856-012-4558-x.

Yang Y, Chu L, Yang S, Zhang H, Qin L, Guillaume O, Eglin D, Richards RG, Tang T. (2018). Dual-functional 3D-printed composite scaffold for inhibiting bacterial infection and promoting bone regeneration in infected bone defect models. Acta Biomater. 1;79:265-275. doi: 10.1016/j.actbio.2018.08.015.

Yang J, Chen HJ, Zhu XD, Vaidya S, Xiang Z, Fan YJ, Zhang XD. (2014). Enhanced repair of a critical-sized segmental bone defect in rabbit femur by surface microstructured porous titanium. J Mater Sci Mater Med. 25(7):1747-56. doi: 10.1007/s10856-014-5202-8.

Some of the results of this thesis were published in previous publications:

Micic M, Antonijevic D, Milutinovic-Smiljanic S, Trisic D, Colovic B, Kosanovic D, Prokic B, Vasic J, Zivkovic S, Milasin J, Danilovic V, Djuric M, Jokanovic V. (2020) Developing a novel resorptive hydroxyapatite-based bone substitute for over-critical size defect reconstruction: physicochemical and biological characterization and proof of concept in segmental rabbit's ulna reconstruction. Biomed Tech (Berl). 27;65(4):491-505. doi: 10.1515/bmt-2019-0218. IF=1.411, M23

Micic M, Jadzic J, Milenkovic P, Antic S, Antonijevic D, Djuric M. (2023) Testing of Different Scanning Protocols Used for Precise 3D-printing of Mandibular Models. J Craniofac Surg. Published ahead of print on May 25 2023. doi: 10.1097/SCS.0000000000009421. IF=1.172, M23

Micic M, Djuric M. (2023) Acelularna 3d štampa u hirurškoj rekonstrukciji koštanih defekata. Medicinski Podmladak. Vol. 74 Br.3. doi: 10.5937/mp74-43883, M54

Biography of the candidate

Milutin Mićić was born in Valjevo, Serbia, 20th November 1981. He finished high school in his home town and enrolled at the Faculty of Philosophy and High Medical School of Professional Studies, University of Belgrade in 2005. In 2011, he graduated on the bachelor academic studies of Ethnology and Anthropology, with an average grade 8.26 and on the proffesional bechelor studies of Medical Radiology, with an everage grade of 7.29. In 2014, he graduated on the master academic studies of Ethnology and Anthropology, with an average grade of 9.57, and on proffesional master studies of Medical Radiology, with an everage grade of 9.00. Same year he enrolled the PhD studies in Skeletal Biology at the Faculty of Medicine, University of Belgrade.

He participated in international project Bioarcheology of Ancient Europe: humans, animals and plants in prehistory of Serbia, Ministry of Science and Education, scientific cycle 2011. – 2015. And BEAN - Bridging the Europian and Anatolian Neolithic demography, migration and lifestyle at the advent of civilisation, Commision of the European Communities – RTD, Bruxelles.

He dedicated his professional work to use of radiological scanning for virtual planning and 3D printing in medicine, with the focus on bone surgery, as well as virtual reconstruction of human remains from archeological sites. He published following scientific papers as the first author:

Micic M, Antonijevic D, Milutinovic-Smiljanic S, Trisic D, Colovic B, Kosanovic D, Prokic B, Vasic J, Zivkovic S, Milasin J, Danilovic V, Djuric M, Jokanovic V. (2020) Developing a novel resorptive hydroxyapatite-based bone substitute for over-critical size defect reconstruction: physicochemical and biological characterization and proof of concept in segmental rabbit's ulna reconstruction. Biomed Tech (Berl). 27;65(4):491-505. doi: 10.1515/bmt-2019-0218. IF=1.411, M23

Micic M, Jadzic J, Milenkovic P, Antic S, Antonijevic D, Djuric M. (2023) Testing of Different Scanning Protocols Used for Precise 3D-printing of Mandibular Models. J Craniofac Surg. Published ahead of print on May 25 2023. doi: 10.1097/SCS.0000000000009421. IF=1.172, M23

Micic M, Djuric M. (2023) Acelularna 3d štampa u hirurškoj rekonstrukciji koštanih defekata, Medicinski Podmladak M54

Mićić Milutin, Exploring possibilities of 3D imaging software use in estimating cortical bone and dental roots thickness, Ninth International Conference on the Mesolithic in Europe, MESO 2015, http://media.wix.com/ugd/f9ff73_3a6e5174fffc4327bbb9e7e241618d6f.pdf , http://media.wix.com/ugd/f9ff73_760b68f0cc214ff8adf7e6e4a36369b3.pdf , Begrade,14.-18. September 2015.

ИЗЈАВА О АУТОРСТВУ

Име и презиме аутора: Милутин Мићић

Број индекса: BS-03/14

ИЗЈАВЉУЈЕМ

да је докторска дисертација под насловом

УТИЦАЈ ИЗБОРА РАДИОЛОШКИХ ПРОТОКОЛА НА ТАЧНОСТ ТРОДИМЕНЗИОНАЛНИХ МЕДИЦИНСКИХ МОДЕЛА, ХИРУРШКИХ ВОДИЧА И КОШТАНИХ ЗАМЕНИКА

- резултат сопственог истраживачког рада
- да дисертација у целини ни у деловима није била предложена за стицање друге дипломе према студијским програмима других високошколских установа;
- да су резултати коректно наведени и
- да нисам кршио ауторска права и користио интелектуалну својину других лица

У Београду, _____ 2023. године Потпис аутора

_____

ИЗЈАВА О ИСТОВЕТНОСТИ ШТАМПАНЕ И ЕЛЕКТРОНСКЕ ВЕРЗИЈЕ ДОКТОРСКОГ РАДА

Име и презиме аутора: Милутин Мићић

Број индекса: BS-03/14

Студијски програм: Биологија скелета

Наслов рада: Утицај избора радиолошких протокола на тачност тродимензионалних медицинских модела, хируршких водича и коштаних заменика

Ментори:

- професор Марија Ђурић, Институт за анатомију, Медицински факулет, Универзитет у Београду
- др Ђорђе Антонијевић, Стоматолошки факултет, Универзитет у Београду

Изјављујем да је штампана верзија мог докторског рада истоветна електронској верзији коју сам предао ради похрањивања у Дигиталном репозиторијуму Универзитета у Београду. Дозвољавам да се објаве моји лични подаци везани за добијање академског назива доктора наука, као што су име и презиме, година и место рођења и датум одбране рада. Ови лични подаци могу се објавити на мрежним страницама дигиталне библиотеке, у електронском каталогу и у публикацијама Универзитета у Београду.

У Београду, _____ 2023. године Потпис аутора

_____

ИЗЈАВА О КОРИШЋЕЊУ

Овлашћујем Универзитетску библиотеку „Светозар Марковић“ да у Дигитални репозиторијум Универзитета у Београду унесе моју докторску дисертацију под насловом:

УТИЦАЈ ИЗБОРА РАДИОЛОШКИХ ПРОТОКОЛА НА ТАЧНОСТ ТРОДИМЕНЗИОНАЛНИХ МЕДИЦИНСКИХ МОДЕЛА, ХИРУРШКИХ ВОДИЧА И КОШТАНИХ ЗАМЕНИКА

која је моје ауторско дело.

Дисертацију са свим прилозима предао сам у електронском формату погодном за трајно архивирање.

Моју докторску дисертацију похрањену у Дигиталном репозиторијуму Универзитета у Београду и доступну у отвореном приступу могу да користе сви који поштују одредбе садржане у одабраном типу лиценце Креативне заједнице (Creative Commons) за коју сам се одлучио.

1. Ауторство (CC BY)

2. Ауторство – некомерцијално (CC BY-NC)

3. Ауторство – некомерцијално – без прерада (CC BY-NC-ND)

4. Ауторство – некомерцијално – делити под истим условима (CC BY-NC-SA)

5. Ауторство – без прерада (CC BY-ND)

6. Ауторство – делити под истим условима (CC BY-SA) (Молимо да заокружите само једну од шест понуђених лиценци. Кратак опис лиценци је саставни део ове изјаве).

У Београду, _____ 2023. године Потпис аутора

_____

1. Ауторство. Дозвољавате умножавање, дистрибуцију и јавно саопштавање дела, и прераде, ако се наведе име аутора на начин одређен од стране аутора или даваоца лиценце, чак и у комерцијалне сврхе. Ово је најслободнија од свих лиценци.

2. Ауторство – некомерцијално. Дозвољавате умножавање, дистрибуцију и јавно саопштавање дела, и прераде, ако се наведе име аутора на начин одређен од стране аутора или даваоца лиценце. Ова лиценца не дозвољава комерцијалну употребу дела.

3. Ауторство – некомерцијално – без прерада. Дозвољавате умножавање, дистрибуцију и јавно саопштавање дела, без промена, преобликовања или употребе дела у свом делу, ако се наведе име аутора на начин одређен од стране аутора или даваоца лиценце. Ова лиценца не дозвољава комерцијалну употребу дела. У односу на све остале лиценце, овом лиценцом се ограничава највећи обим права коришћења дела.

4. Ауторство – некомерцијално – делити под истим условима. Дозвољавате умножавање, дистрибуцију и јавно саопштавање дела, и прераде, ако се наведе име аутора на начин одређен од стране аутора или даваоца лиценце и ако се прерада дистрибуира под истом или сличном лиценцом. Ова лиценца не дозвољава комерцијалну употребу дела и прерада.

5. Ауторство – без прерада. Дозвољавате умножавање, дистрибуцију и јавно саопштавање дела, без промена, преобликовања или употребе дела у свом делу, ако се наведе име аутора на начин одређен од стране аутора или даваоца лиценце. Ова лиценца дозвољава комерцијалну употребу дела.

6. Ауторство – делити под истим условима. Дозвољавате умножавање, дистрибуцију и јавно саопштавање дела, и прераде, ако се наведе име аутора на начин одређен од стране аутора или даваоца лиценце и ако се прерада дистрибуира под истом или сличном лиценцом. Ова лиценца дозвољава комерцијалну употребу дела и прерада. Слична је софтверским лиценцама, односно лиценцама отвореног кода.